The Study of MnO_x Catalysts for Water Oxidation by Soft X-Ray Spectroscopy

im Fachbereich Physik
der Freien Universität Berlin

eingereichte Dissertation zur Erlangung des akademischen Grades
der Doktorin der Naturwissenschaften (Dr. rer. nat.)

vorgelegt von

Munirah Atique Khan

Berlin

Juni 2015

HZB Helmholtz Zentrum Berlin

Freie Universität Berlin

1. Gutachter: Prof. Dr. Emad Flear Aziz
2. Gutachter: Prof. Dr. Ludger Wöste

Disputation am…… 30. 07. 2015

Die selbständige und eigenhändige Anfertigung versichere ich an Eides statt.

Berlin, den

03-08-2015

Munirah Atique Khan

Table of Contents

Abstract

The efficient conversion of solar energy to chemical energy in a clean and sustainable way for storage is one of the greatest challenges for the scientific community. This energy conversion is performed in nature through photosynthesis, featuring a series of redox reactions, a key to which is the splitting of water. Water oxidation is a mechanistically complex redox reaction, catalyzed in all photosynthetic organisms within the oxygen evolution center (OEC) of photosystem II (PS II), which contains a $CaMn_4O_5$ cluster. In this regard manganese oxides (MnO_x) are effective water oxidation catalysts providing structural and mechanistic clues about the nature of the reactions occurring inside OEC. This study has established soft X-ray spectroscopy explicitly at manganese L-edge and oxygen K-edge as a tool for gaining electronic structural insights into water oxidation catalysis. Changes in the local electronic structure of three series of MnO_x derived from different manganese complexes are investigated *ex situ* by X-ray absorption spectroscopy (XAS) and resonant inelastic X-ray scattering (RIXS).

In the first part of the study, narrowing of the local gap between highest occupied molecular orbital (HOMO) and lowest unoccupied molecular orbital (LUMO) is observed when electrical voltage and visible light illumination were applied simultaneously to the Mn catalytic system doped in nafion. The MnO_x catalyst with the smallest local HOMO-LUMO gap, strongest charge transfer and higher concentration of Mn^{3+} over $Mn^{2+/4+}$ produced itinerant electrons that contributed to the enhancement in catalytic activity (water oxidation). Theoretical calculations demonstrated that the gap between the ground and first excited valence states for Mn^{3+} was notably lower than for $Mn^{2+/4+}$ oxidation states, which was reflected in the unique features of inelastic scattering spectra.

In the second part of the thesis, the electronic structures of two series of MnO_x films electrodeposited from ionic liquids as a function of heat treament and electrolyte pH were investigated. In the first section, the effect of heat treatment on electronic structures of MnO_x films was studied. The manganese L-edge absorption and emission spectra measured at various stages of the heat treatments identified two major manganese oxide species, Mn_3O_4 and birnessite, that constitute 97% of the MnO_x at all heating stages. The ratio of birnessite vs. Mn_3O_4 remained almost constant at all temperatures, except for the transformation of a small amount (8%) of birnessite into Mn_3O_4 when the MnO_x films are heated ≥90 °C. For the best catalyst (heat treated at 90 °C) this conversion was accompanied by loss of water molecules and hydroxyl species that were accommodated within the transformed birnessite layered structure before the phase transformation. Further dehydration at higher temperature (120 °C) that removed more structural water did not lead to further phase transformation but to poorer catalytic performance, indicating the importance of maintaining a certain amount of the structural water molecules embedded within the layered birnessite phase.

In the second section, MnO_x films prepared from ionic liquids with different pH values (acidic, basic and neutral) were probed with X-ray absorption spectroscopy (XAS) at manganese L-edge and oxygen K-edge. It was shown that varying the pH values of electrolyte can remarkably change the electronic structure of catalysts. All the catalysts were found to be mixtures of Mn_2O_3, Mn_3O_4, MnO_2 and birnessite in different proportions. Linear fitting of experimental spectra was performed to estimate the amount of each oxide phase present in catalysts. The best catalyst (prepared from neutral precursor) implied the importance of Mn_2O_3, Mn_3O_4, MnO_2 and birnessite in MnO_x in right proportion.

In conclusion, the three series of Mn catalysts investigated in this study showed notably different patterns of spectroscopic features providing insight into Mn 3d orbitals, local HOMO-LUMO gap at Mn sites and various MnO_x species of the active catalyst. New experiments are underway using techniques like infrared spectroscopy, pump-probe experiments and photoemission spectroscopy to reveal further information about their electronic and molecular structure. Such detailed information can open the possibility of optimizing catalysts of water splitting.

Abstrakt

Die effiziente Umwandlung von Solarenergie in chemische Energie in einer sauberen und nachhaltigen Weise ist eine der größten Herausforderungen für die Wissenschaft. In der Natur erfolgt die Umwandlung durch Photosynthese, die eine Reihe von Redoxreaktionen umfasst. Sie ist der Schlüsselprozess zur Wasseraufspaltung. Die Wasseroxidation ist eine mechanistisch komplexe Reaktion, die in allen photosynthetisch aktiven Organismen innerhalb des wasserspaltenden Komplex OEC (oxygen evolution center) des Photosystems II (PS II) stattfindet.

In dieser Arbeit wurde Spektroskopie mit weicher Röntgenstrahlung direkt an der Mangan L-Kante und der Sauerstoff K-Kante von Manganoxiden angewendet, um Informationen über elektronische und strukturelle Prozesse bei der Katalyse der Wasseroxidation zu erlangen. Es wurden Änderungen in der lokalen elektronischen Struktur zweier mit unterschiedlichen Mn-Komplexen hergestellter Serien von MnOx mittels Röntgenabsorptionsspektroskopie (XAS) und resonanter inelastischer Röntgenstreuung (RIXS) ex situ untersucht.

Im ersten Teil dieser Arbeit konnte beobachtet werden, wie die lokale HOMO-LUMO-Lücke des Mn-Katalyse-Systems (dotiert in Nafion) bei Anlegen einer Spannung und gleichzeitiger Bestrahlung mit sichtbarem Licht abnimmt. Der Mn-Katalysator mit der kleinsten lokalen HOMO-LUMO-Lücke und dem stärksten Ladungstransfer sowie hoher Konzentration an den Oxidationszuständen Mn^{3+} und $Mn^{2+/4+}$ erzeugt Leitungselektronen, die dazu beitragen, dass die katalytische Aktivität (Wasseroxidation) verstärkt wird. Theoretische Rechnungen zeigen, dass die energetische Lücke zwischen dem Grundzustand und dem ersten angeregten Valenzzustand für Mn^{3+} merklich kleiner ist als für den $Mn^{2+/4+}$ Oxidationszustand, was sich in den eindeutig unterscheidbaren spektralen Strukturen der RIXS Spektren wiederspiegelt.

Im zweiten Teil dieser Arbeit werden die Ergebnisse zur elektronischen Strukturuntersuchung von MnOx-Filmen vorgestellt. Hierzu wurden die aus einer ionischen Flüssigkeit elektrolytisch abgeschiedenen Filme in Abhängigkeit des pH-Wertes und des Wärmeeintrags untersucht. Die für verschiedene Stadien des Wärmezufuhrprozesses an der Mn L-Kante gemessenen Spektren lassen zwei Arten von Manganoxid erkennen, Mn_3O_4 und Birnessit, die 97% des MnO_x in allen Stadien des Wärmezufuhrprozesses ausmachen. Das Verhältnis von Birnessit zu Mn_3O_4 bleibt für alle Temperaturen nahezu konstant, die Ausnahme bildet die Umwandlung eines kleinen Anteils (8%) des Birnessit zu Mn_3O_4 bei Erhitzung der MnO_x Schicht auf über 90°C.

Für den besten Katalysator (bei einer Temperatur von 90° C) wurde die Umwandlung begleitet von einem Verlust von Wassermolekülen und Hydroxyl-Gruppen, die vor dem Phasenübergang innerhalb der umgewandelten Birnessit-geschichteten Struktur lokalisiert waren. Eine weitere Erhöhung der Temperatur auf 120°C führt zu einer weiteren Reduzierung des eingebetteten Wassers, es führt aber nicht zu einem vermehrten Phasenübergang. Stattdessen nimmt die katalytische Performance ab. Dies deutet darauf hin, dass für die Aufrechterhaltung der guten Katalyseeigenschaften eine gewisse Menge an eingelagertem Wasser in der Birnessit-geschichteten Phase notwendig ist.

Weiterhin wurden Manganoxidfilme aus ionischen Flüssigkeiten mit unterschiedlichen pH-Werten (sauer, basisch und neutral) hergestellt und mit Röntgenabsorptionsspektroskopie (XAS) an der Mangan L-Kante und an der Sauerstoff K-Kante untersucht. Dabei zeigte sich, dass die pH-Werte des Elektrolyten einen großen Einfluss auf die elektronische Struktur des Katalysators haben. Sämtliche untersuchten Katalysatoren waren Gemische aus Mn_2O_3, Mn_3O_4 und MnO_2 sowie Birnessit zu unterschiedlichen Anteilen. Mit Hilfe der linearen Regression wurde aus den experimentell gewonnenen Spektren der Anteil jeder Manganoxidspezies am jeweilig untersuchten Katalysator bestimmt. Es zeigte sich, um die besten Katalyseeigenschaften zu erhalten (die bei einem Katalysator auftraten, der aus einem Precursor bei neutralem pH-Wert hergestellt wurde), müssen die verschiedenen Manganoxideanteile und Birnessit in einem bestimmten Verhältnis zueinander stehen.

Zusammenfassend lässt sich sagen, dass die drei in dieser Arbeit untersuchten Mangan-Katalysator-Serien ausgeprägte spektroskopische Unterschiede aufzeigen, die Rückschlüsse auf die elektronische Struktur und auf die lokalen energetischen HOMO-LUMO Lücken dieser aktiven Mn-Katalysatoren geben. Neuere Experimente, die sowohl Infrarotspektroskopie, zeitaufgelöste Pump-Probe-Verfahren und Photoemissionspektroskopie umfassen, sind auf dem Weg. Dadurch lässt sich insbesondere die elektronische Struktur umfassend bestimmen. Hieraus lassen sich dann weitere Informationen für die Optimierung von Katalysatoren für die Wasserspaltung ableiten.

List of Publications

Parts of this thesis have been published or submitted as the following articles:

1. **Electronic Structural Insights into Efficient MnO_x Catalysts.**
   Munirah Khan, Edlira Suljoti, Archana Singh, Shannon A. Bonke, Tim Brandenburg, Kaan Atak, Ronny Golnak, Leone Spiccia and Emad F. Aziz .
   Journal of Material Chemistry A.
   2 (2014) 18199–18203.
   http://dx.doi.org/10.1039/C4TA04185B

2. **On the Origin of the Improvement of Electrodeposited MnO_x Films in Water Oxidation Catalysis Induced by Heat Treatment.**
   Munirah Khan, Jie Xiao, Fengling Zhou, Mikhail Yablonskikh, Douglas R. MacFarlane, Leone Spiccia, and Emad F. Aziz.
   ChemSusChem.
   8 (2015) 1980–1985.
   http://dx.doi.org/10.1002/cssc.201500330

3. **Electronic Structures Variations in Water Splitting MnO_x Films Deposited from Ionic Liquids as a Function of pH.**
   Munirah Khan, Jie Xiao, Fengling Zhou, Douglas R. MacFarlane, Leone Spiccia, and Emad F. Aziz.
   In preparation.

4. **Enhancing the Catalytic Activity by Narrowing the Local Energy Gaps – XAS and RIXS Studies of a Manganese Water Oxidation Catalyst.**
   Jie Xiao, **Munirah Khan**, Archana Singh, Edlira Suljoti, Leone Spiccia, and Emad F. Aziz.
   ChemSusChem.
   8 (2015) 872–877.
   http://dx.doi.org/10.1002/cssc.201403219

5. **Unraveling Electronic Structure of Photocatalytic Manganese Complexes via Theoretical Multi-Reference X-Ray Spectroscopy**
   Sergey I. Bokarev, **Munirah Khan**, Mahmoud Abdel-Latif, Jie Xiao, Leone Spiccia, Rifaat Hilale, Saadullah G. Azize, Emad F. Aziz, and Oliver Kühn.
   The Journal of Physical Chemistry C
   Publication Date (Web): July 21, 2015.
   http://dx.doi.org/10.1021/acs.jpcc.5b05169

Apart from this thesis, I have contributed for the following articles during my PhD:

1. **Local Energy Gap Opening Induced by Hemin Dimerization in Aqueous Solution**.
   Ronny Golnak, Jie Xiao, Kaan Atak, **Munirah Khan**, Edlira Suljoti and Emad F. Aziz.
   Journal of Physical Chemistry B.
   119 (2015) (7) 3058–3062.
   http://dx.doi.org/10.1021/jp509966q

2. **Probing Orbital Symmetry in Solution: Polarization-Dependent Resonant Inelastic Soft X-Ray Scattering on Liquid Micro-Jet.**
   Brian Dierker, Edlira Suljoti, Kaan Atak, Kathrin Maria Lange, Nicholas Engel, Ronny Golnak, Marcus Dantz, Kai Hodeck, **Munirah Khan**, Nobu Kosugi and Emad Flear Aziz.
   New Journal of Physics.
   15 (2013) 093025-093034.
   http://dx.doi.org/10.1088/1367-2630/15/9/093025

Outline of Thesis

This dissertation is written with following outline: Chapter 1 provides basic information on water splitting catalysts with a comprehensive literature. Chapter 2 covers the theoretical aspects of all the experimental techniques employed, mainly X-ray absorption and resonant inelastic X-ray scattering along with data acquisition techniques and handling procedures. The original work is presented in Chapter 3 and in Chapter 4, where each chapter consists of different sections taken from articles either published or in preparation. Chapter 3 provides detailed information about the Mn 3d configuration revealed by X-ray absorption spectroscopy (XAS) and resonant inelastic X-ray scattering (RIXS) measurements on Mn $L_{2,3}$-edge. Standard procedures to prepare the MnO_x catalysts primarily doped into nafion are explained. The electronic structures of catalysts are derived from the measured spectra and their possible effect on the water oxidation mechanism is explained. Theoretical simulations with multi-reference approach to X-ray spectra are applied utilizing the restricted active space self-consistent field (RASSCF) technique together with the state interaction method (RASSI) for spin-orbit coupling. Chapter 4 is about manganese $L_{2,3}$-edge and oxygen K-edge XAS of MnO_x catalysts that were deposited from ionic liquids at different pH values or were heat treated. With the help of linear fitting, experimental spectra are explained to resolve the change of structural moieties. Chapter 5 finally concludes the outcome of this dissertation with a future perspective.

Chapter 1

Water Splitting: A Fuel for the Future

1.1 Introduction

The energy production through non-renewable sources is coupled with the emission of green house gases and can not fulfill the future needs. Scientists have directed their attention towards the development of alternative renewable energy supplies that are free of carbon emissions. The requirement to generate renewable fuel on terawatt scale is the biggest challenge of this century. To produce energy on such a mass scale, water is the cheapest and the most abundant feedstock, which can be converted into hydrogen fuel through water splitting [1-2]. This Chapter introduces some basic principles of water oxidation and a comprehensive literature survey of water splitting systems and their mechanism. Water is the richest source of hydrogen on earth among all available resources, however delivering the necessary energy input to break the strong O-H bonds of water ((enthalpy ΔH°) 494 kJ/mol) while overcoming the mechanistic complexity is the "Holy Grail" of chemistry [3]. To produce economically viable and environmentally friendly hydrogen using water is only possible through utilization of abundant solar energy falling on the earth to drive water splitting directly or indirectly. Solar energy can supply energy cost of water splitting, a well-known electrochemical process occurring in series of chemical reactions. During water splitting, water oxidizes into four-electrons to produce dioxygen and protons, which are then reduced to yield molecular hydrogen summarized by following equations:

$$2H_2O + O_2 \rightarrow 4H^+ + 4e^- + 2O_2$$

$$2H^+ + 2e^- \rightarrow H_2$$

$$2H_2O + O_2 \rightarrow 2H_2 + 2O_2$$

The water oxidation reaction is a thermodynamically and kinetically demanding process. According to Nernst equation, a minimum theoretical energy input of 1.23 V (vs. NHE) at pH 0 is needed to complete the process [3]. This energy is consumed in the water oxidation half reaction which is energetically uphill. Removing four electrons and four protons from two water molecules leads to the formation of an O-O bond. In practice, the water oxidation is multi-step reaction involving various high-energy intermediates [3]. The complexity of this multi-step reaction, which even further enhances energy demands, makes it difficult to achieve without the application of overpotential. This energy barrier can be significantly lowered with a catalyst that couples the dissociation steps to the energy-releasing step of O-O bond formation without releasing reactive intermediates. Many catalysts based on rare earth complexes and transition metal complexes are used as anodes of an electrochemical cell [4]. Schematic presentation of one of these electrochemical cells is shown in Figure 1.1.

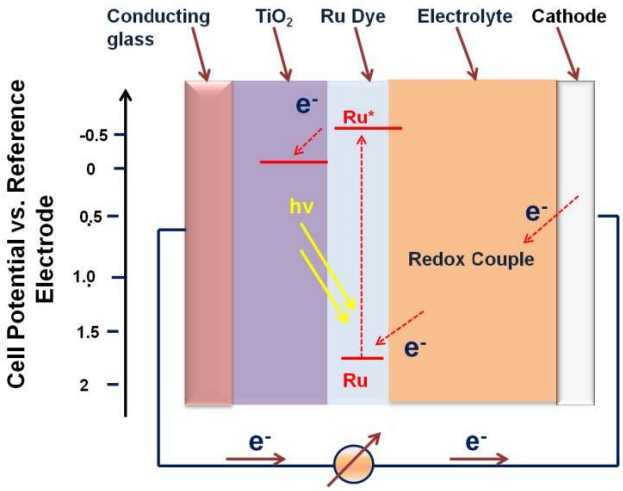

Figure 1.1. Schematic representation of an electrochemical cell using Ru catalyst as an anode. In the photocurrent generation process, the photons are absorbed by Ruthenium-dye molecules followed by a fast ejection of electrons from the dye to the conduction band of TiO_2. Subsequently, the dye is regenerated through an electron transfer from a redox couple in the liquid electrolyte.

1.2 Photosystem II

Solar to chemical energy conversion is observed in nature through all photosynthetic organisms such as cyno bacteria and green plants through photo system II which is responsible for water splitting by releasing the molecular oxygen into atmosphere [4-6]. Inside photosystem II (PS II) there is a ubiquitous natural catalytic center that efficiently oxidizes water using manganese, a cheap and abundant element, and sunlight as the energy input as shown in Figure 1.2 [6-10].

Cyanobacteria, algae and plants which are photosynthetic in nature are proposed to originate from water-oxidizing bacteria millions of years ago which could catalyze the oxidation of soluble Mn^{2+} to insoluble manganese oxides of the general formula MnO_x [11]. Further evolution of these MnO_x into compounds efficient in water oxidation could have been originated by bacteria which were able to oxidize water. This evolution seems logical as the amount of water on the Earth was huge and water-oxidizing bacteria could thus reproduce and survive more than other bacteria.

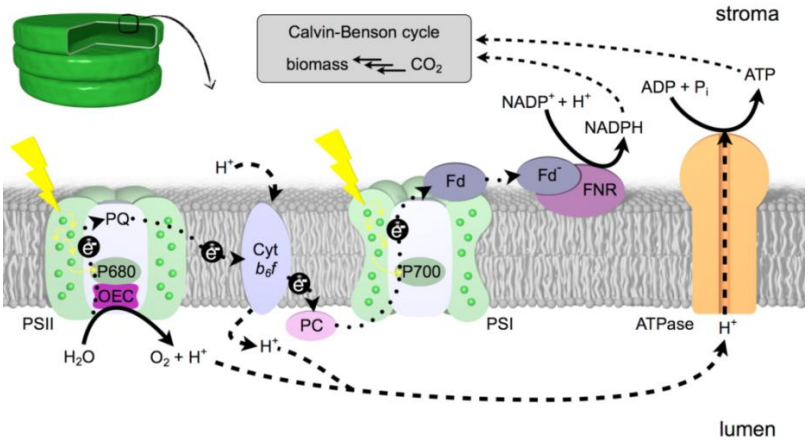

Figure 1.2. Schematic presentation of photosynthesis taken from reference [12]. The Figure shows oxygen evolving complex (OEC) inside photosystem II as water splitting center.

1.2.1 Water Oxidation Center (WOC)

Water oxidation center (WOC) in photosystem II is composed of a Mn_4CaO_5 cluster which efficiently catalyses water with a turnover number (TON) of 180,000 molecules of O_2 per site and turnover frequencies (TOF) of 100-400s^{-1} [13-14]. The whole structure of Mn_4CaO_5 cluster plays a role in water oxidation catalysis and is closely scrutinized to provide mechanistic insights into the operation of this extremely complicated photosynthetic machinery [15]. The active site responsible for water oxidation during photosynthesis identified as a $CaMn_4O_5.(H_2O)_4$ cluster embedded in the thylakoid membrane is most widely studied catalyst comprising a cubane-like $CaMn_3O_x$ cluster and a dangling Mn center [16]. In the latest high-resolution structure with 1.9 Å, Umena *et al* has proved asymmetric Mn_3Ca cubane with a dangling Mn center held together by five oxo-bridges and amino acids from the protein backbone. The structure resembles a distorted chair, with the asymmetric cubane serving as the seat base and the isolated manganese and oxygen atoms serving as the back of the chair. The presence of four water molecules (two on the calcium center and two on the dangling Mn center) is established and it is reported that two of these water molecules serve as the substrate for water oxidation [17].

An intense investigation on this amazing natural system has leaded the path to artificial photosynthesis. Synthetic photoelectrocatalytic molecular catalysts have been developed with the intention of achieving an efficient water oxidation. Nocera *et al* has reported an artificial leaf that splits water at room temperature using cobalt based catalyst [2]. Dau *et al* successfully manufactured active catalysts mimicking the PS II from cheap transition metals like manganese, cobalt and nickel and investigated their water splitting mechanism using K-edge X-ray absorption spectroscopy [18]. Spiccia *et al* has reported water splitting catalysts using different preparation techniques like screen printing, doping and electrodeposition and has characterized their structure with SEM, TEM, XRD and EDX [19]. Yachandra *et al* has employed XANES, K_β XES and EXAFS along with electron paramagnetic resonance spectroscopy to explain the structure of catalysts that are mimick of PS II [20]. Inspite of all the advances, water oxidation by the WOC is still not entirely understood and several models for the mechanism of oxygen evolution in PS II have been proposed to account for the detailed oxygen evolution by PS II. Out of these many proposed mechanisms "Kok cycle" is widely accepted to explain the basic principles for the function of the WOC [21-22]. According to the well-known Kok scheme the WOC can exist in 5 states: S_0 to S_4. The subscript 0-4 represents the number of oxidizing equivalents (oxidation state) abstracted from the WOC by light at each step. Singlet excitation up to 1.8 eV produces a fast electron transfer in chlorophyll P_{680} which is the light sensitizing antenna of photosystem II. An intermediate electron acceptor pheophytin produces an ion radical pair [P_{680}^{+} $Pheo^{-1}$] followed by a fast electron transfer from $Pheo^{-\cdot}$ to an acceptor Q which is the iron complex with plastoquinone. At this stage P_{680}^{+} is reduced from WOC via a redox active center called tyrosin. The last state S_4 is unstable and is independent of light where oxidized water center reacts with an attached substrate of water to produce free oxygen. Currently, the functional mechanism of whole cycle from the state S_0 to S_4 is not completely understood.

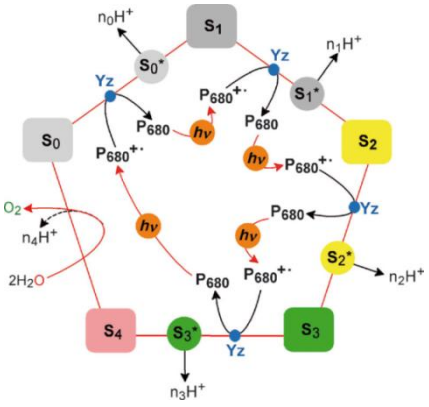

Figure 1.3. The Kok cycle explains the water oxidation mechanism in photosystem II taken from reference [22].

1.3 Water Oxidation Catalysts

Metal oxides have been known to catalyze water oxidation in a heterogeneous solution, driven by sacrificial oxidants in either electrochemical (potential driven) or photo-electrochemical cells (light driven plus potential). The most efficient and widely employed materials are active oxides of rare and precious metals such as Pt, RuO and IrO_2 [23-28]. Due to limited availability and high cost of these precious metals, their large scale application is limited as water splitting catalysts. Extensive literature is available on recent developments of metal oxides of the first series of transition metals used as photo electrochemical water splitting catalysts. The ultimate goal is to design new oxygen evolving catalysts using inexpensive and abundant materials such as transition metals like manganese (Mn), cobalt (Co) and Iron (Fe) [29-32].

For the reason that manganese is both inexpensive and environmentally friendly, many efforts have been made to prepare Mn complexes for important applications such as electrochemical capacitors, lithium and other batteries, electro catalysis for the Oxygen Reduction Reaction (ORR), the catalytic oxidation of organic dyes and MnO_2 based gas sensors [33-36]. Manganese oxides have also been studied as an anode catalyst that mimics the structure of the WOC in PS II and/or catalyze water oxidation. A large number of Mn complexes have been tested for their ability to catalyze water oxidation, although none of the reported complexes are accurate structural mimic of the WOC. Manganese oxides are prepared using various techniques such as precipitation, electrodeposition, hydrothermal methods and sol-gel processes [37-40].

1.4 Important Factors for Water Oxidation Catalysis

The water splitting catalyst in nature provides a model for designing an efficient, robust and sustainable artificial water splitting system. Being complex in nature the water splitting process is dependent on many factors for its efficiency. Very useful insights have emerged from manganese oxide clusters (MnO_x) as artificial water oxidation catalysts to understand the important factors and their pertinent roles. It has already been shown that operating and deposition conditions (precursor complex, pH, temperature, etc.) can affect the cluster size, composition, stability and structural moieties of MnO_x catalysts. These factors are being discussed as follows.

1.4.1 Morphology and Cluster Size of Catalyst

It is well known that nanostructured materials have high surface areas and can provide a large area of interface between the catalyst and the electrolyte, which would effectively promote the catalytic performance.

Thus, nanostructured MnO_x is a promising material for developing highly robust, efficient water oxidation catalysts. Recently various manganese molecular compounds have been prepared and used as oxygen evolving catalysts. The catalysts exhibited high turnover frequencies for catalytic water oxidation when embedded into a Nafion membrane. In these studies, a series of managanese complexes were doped by ion exchange into a thin Nafion layer that had been deposited on conductive electrodes [41]. An important feature of Nafion films is that hydrophilic channels are formed that are lined by sulfonate head groups whose charges are balanced by counter ions such as H^+ and Na^+. Such a property has been exploited in fuel cells where Nafion films are used as proton conducting membranes. The permeability of these channels to cations (but not anions) means that the mobile cations (H^+ or Na^+) can be exchanged by, for example, cationic manganese clusters. Catalysis by the Mn-exchanged Nafion films was achieved by polarizing the modified electrode at 1.0 V (vs Ag/AgCl) under illumination with visible light under near-neutral pH conditions (pH ~ 6). To investigate the mechanism of water oxidation by $[Mn4O_4L_6]^+$ in Nafion, X-ray absorption spectroscopy (XAS) was used to probe the fate of the cluster embedded in a Nafion film [42-43]. These studies established that the cluster dissociates upon introduction into Nafion, giving a reduced Mn^{2+} state which re-oxidizes to form a fragmented MnO_x birnessite phase similar to bacteriogenic birnessite, a MnO_x phase which is stable under acidic operating conditions. Cycling between a reduced Mn^{2+} state and MnO_x was shown to be responsible for the sustained water oxidation catalysis instead of the initially doped cluster. In addition, it was found that by using different manganese precursor complexes, the size and catalytic activity of the MnO_x nanoparticles were altered.

1.4.2 Potential and pH of Electrolyte

Many manganese oxides (MnO_x) have been explored as active water oxidation catalysts. They often suffer from poor catalytic activity or instability problems under neutral conditions. A Pourbaix diagram can indicate the stability of various Mn oxide species under a large range of pH as shown in Figure 1.4 [44]. Ohsaka and co-workers studied the pH dependence of electrochemically deposited nanorods of MnO_x in a γ-MnOOH phase for water oxidation reaction. The nanorods showed the maximum activity in the basic medium and the activity dropped sharply in acidic and neutral medium [45]. Morita and Tamura have reported a mixture of Mn_2O_3 and β-MnO_2 deposited by the thermal decomposition of the manganese nitrate. This mixture was able to perform water oxidation activity in acidic as well as in basic medium. However, in basic electrolytes (1M KOH), the MnO_x electrode was shown to efficiently oxidize water for a prolonged period of time (20 hrs) without any further increase in the overpotential. A significant increase in the overpotential (by 150 mV) was shown over the same period of time in acidic medium.

The low activity in acidic medium was attributed to an increase in the oxygen content in the film [46]. Until recently, no comprehensive explanation had been provided for the higher catalytic activity of MnO_x in basic medium. It would be advantageous if highly active MnO_x water oxidation catalysts could be developed which operate under neutral chemical environments to minimize loss/degradation processes.

1.4.3 Electronic and Structural Moieties

A connection between manganese oxides and the OEC is already established in section 1.2 suggesting that all of the mechanisms proposed for the origin of PS II deal with the bio-mineralization of Mn into Manganese oxides. Manganese oxides are discussed as inorganic models for the OEC where Mn centres are μ-oxo bridged nano-scaled sections of a manganese oxide structure embedded in the amino acid environment of PS II [44, 47- 48]. Birnessite-like synthetic MnO_x prepared from various methods have been identified as promising water oxidation catalysts revealing their structural features related to the OEC of PS II [49-53]. Birnessites are abundant on Earth and have a number of properties that are closely related to the OEC. In birnessite distorted amorphous layers formed by edge sharing MnO_6 octahedra have many defects. The oxidation state of birnessite averages between 3.5-3.8 as shown by the Pourbaix diagram in Figure 1.4. As compared to highly ordered materials which do not possess structural flexibility, defected layer structure of birnesssite can act as coordination sites for water to attach different Mn active centers. In the defected layers of birnessite many cations like Sr^{+2}, Mg^{2+}, Ca^{2+} can be incorporated [54]. $CaMnO_x$ showed the highest catalytic activity, followed by $SrMnO_x$ and $MgMnO_x$ with the lowest activity. As Ca^{2+} is essential for the activity of PS II, such impurities in birnessite structure can further enhance its activity although their precise role in the catalytic cycle is currently unknown.

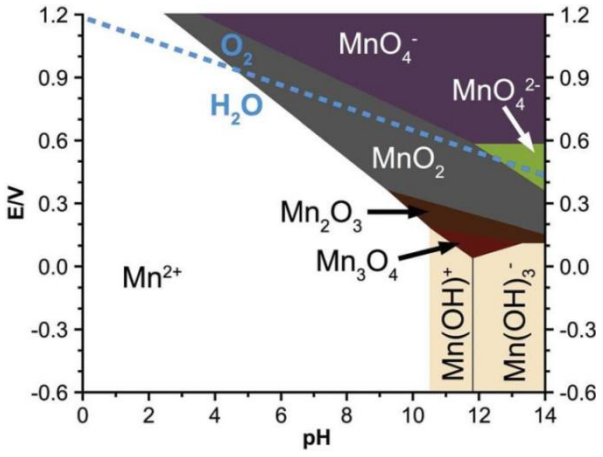

Figure 1.4. Pourbaix diagram showing the stability of manganese species as a fuction of pH, taken from reference [49].

The Mn layer vacancies of birnessite have been reported to elongate Mn–O bonds as observed for Jahn-Teller distorted MnO_6 octahedra present in the oxide structures [50, 53, 55-58]. The increased number of elongated and weaker Mn–O bonds contributes to an increased structural flexibility that has already been correlated to a higher activity in water oxidation catalysis [44, 50, 53, 59]. In another study, birnessite-like manganese oxides (MnO_x) showing a high activity in water oxidation catalysis are prepared through partial oxidation of the outer shell of the MnO precursor particles with Ce^{4+} as oxidant. An amorphous birnessite-like phase composed of edge-sharing MnO_6 octahedra with a large number of layer defects was shown. Ca^{2+} or $Mn^{2+/3+}$ ions, was placed in the interlayer space defects to balance the negative charges on the so formed layers. A comparison of the resulting structure of the MnO_x layers to that of layered $CaMnO_x$ described above shows that these materials are closely related [50, 53, 60].

Other than oxidative conditions needed to convert MnO into MnO_X, it was shown that Mn_3O_4, α-Mn_2O_3, β-MnO_2, $Ca_2Mn_3O_8$ and $CaMn_4O_8$ can also be transformed into catalytically active, layered MnO_x structures by either using Ce^{4+} as an oxidant or applying an electrochemical potential in the presence of $LiClO_4$ [61-64]. It has been reported that manganese oxide particles can also be doped in silica to produce efficient catalyst of water splitting. X-ray absorption spectroscopy has revealed the catalysts are composed of an intermediate $Mn^{3+/4+}$ oxidation states and could thus very likely be birnessite-like oxides [65].

Other than birnessite many other phases of Mn oxides are also reported as active catalysts for water oxidation. Screen-printed films of an amorphous nanostructured pyrolusite (β-MnO_2) phase, prepared from a comproportionation reaction of Mn^{2+} and MnO_4^- under acidic conditions, exhibited a much higher water oxidation activity than highly crystalline commercial samples [66]. In pyrolusite, edge-sharing MnO_6 octahedra are assembled into chains, with the width of a single octahedron, which share corners with neighbouring octahedra to form a tunneled but saturated octahedron structure [67]. In another study, MnO_x supported on glassy carbon electrodes were heat treated to improve the water oxidation activity. Electrochemical characterization showed that nanoparticles of MnO prepared at glassy carbon electrode at room temperature were inactive for water splitting. A subsequent heat treatment of 500 °C had converted these inactive MnO nanoparticles into Mn_3O_4 which were found to be efficient in water oxidation [68].

It is important to note that all the proposed mechanisms above for water-oxidation catalysis by the OEC and amorphous manganese oxides do not explain the role of the local electronic structure at Mn catalytic sites. Further experimental and theoratical investigations of the electronic structure of MnO_x catalysts are needed to better elucidate the mechanisms leading to high activity of Mn based water splitting catalysts.

Chapter 2

Experimental Techniques and Instruments

2.1 Introduction

X-ray spectroscopy is an experimental technique probing local electronic structure by resonantly exciting the characteristic core levels of elements. An X-ray photon can excite an electron from an occupied state into an unoccupied state leaving a core-hole which will decay either by emission of a photon or an electron through Auger process. It provides an element specific probe due to its atom selectivity and is highly sensitive to chemical bonds and the local environment. X-ray absorption spectroscopy (XAS) and resonant inelastic X-ray scattering (RIXS) are the ideal and, possibly, the only currently available techniques that can directly measure the unoccupied states and valence electron excitations, respectively, near the Fermi level of the element of interest (catalytic sites) in bulk. XAS probes the intermediate state, while the final state is investigated by RIXS. The details are shown in Figure 2.1. The two dipole allowed transitions (initial to intermediate followed by intermediate to final) makes the dipole forbidden direct d-d transitions (initial to final) accessible by RIXS. The energy difference of the incident X-ray (shown in blue) and the emitted X-ray (shown in red) gives rise to the energy of d-d transition, i.e. loss features often observed in typical RIXS spectra. In this chapter an overview of the soft X-ray absorption and emission spectroscopies and the experimental aspects of these techniques will be presented.

In nature, transition metals are part of many biological and chemical processes such as water oxidizing center of photo system II and hemoglobin of blood. It is therefore of paramount interest to understand valence electronic structure of transition metals which is the key to their chemical function. In transition metal complexes valence levels are delocalized in contrast to core-electrons which are localized on a single atom. Through the advances in high power X-ray sources, high resolution X-ray spectrometers and the development of new synchrotron radiation facilities, X-ray spectroscopy has become a widely used tool to investigate such processes.

2.2 Soft X-Ray Spectroscopy

In the soft X-ray regime, due to high transition probability dipole-allowed transitions dominate the absorption spectrum. Higher order processes, such as electronic quadrupole or magnetic dipole transitions are significantly weaker than dipole allowed transitions. The main spectroscopic measurement used in this thesis is dipole-allowed oxygen K-edge and manganese L_2 and L_3-edge transitions to the unoccupied valance orbitals (2p for oxygen and 3d and 4s for the manganese) [69]. Hence those edges allow a strong X-ray probe of the valance electronic structure. The absorption edge is defined by the energetic position of a specific shell (K, L, M…) of an element making X-ray spectroscopy an element specific probe to the electronic structure. In K-edge spectroscopy a single electron is excited from the 1s state into the empty 2p level: hence the absorption cross-section represents the density of the empty states. However in L-edge spectroscopy many factors such as strong interaction of the 2p hole with the 3d electrons, the electron-electron correlation, spin-orbit coupling, affect the final spectrum [70-73].

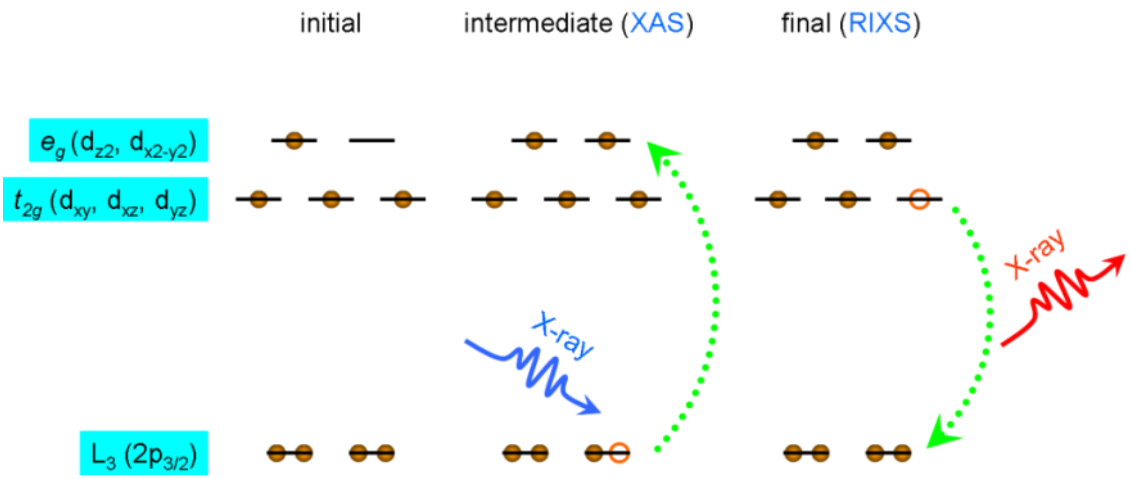

Figure 2.1. Illustration of the electronic transitions of XAS and RIXS processes at the L_3-edge of a typical d^4 transition metal ion (such as Mn^{3+}) in octahedral symmetry.

The final core-hole states have a finite lifetime which adds some energy uncertainty to the spectral features, due to Heisenberg's uncertainty principle. Such lifetime width has typically an average of a few femtoseconds [74-75]. This relaxation happens via two channels, non-radiative and radiative decays namely fluorescence yield and Auger electron yield. In the Auger process, filling the core-hole with a valence electron is followed by emission of an Auger electron. In the fluorescence process a valence electron fills the core-hole followed by spontaneous emission of a photon.

The probability of these processes depends on the element and the transition considered. Figure 2.2 shows the fluorescence and Auger probabilities for the K, and L_3 shells as a function of the atomic number of elements. The Auger process dominates for the light elements at the K and L_3 core levels. Fluorescence yield is the dominant decay mechanism only for heavy elements at K-edge, and also at the L-edge. It reflects that fluorescence yield is about 1% at K-edge of light elements such as oxygen. In this study, three types of X-ray spectroscopy is used, X-ray absorption spectroscopy (XAS), X-ray emission spectroscopy (XES) spectroscopy and resonant inelastic X-ray scattering (RIXS) spectroscopy to study the electronic properties of water splitting catalysts. The details of these methods are discussed as follows.

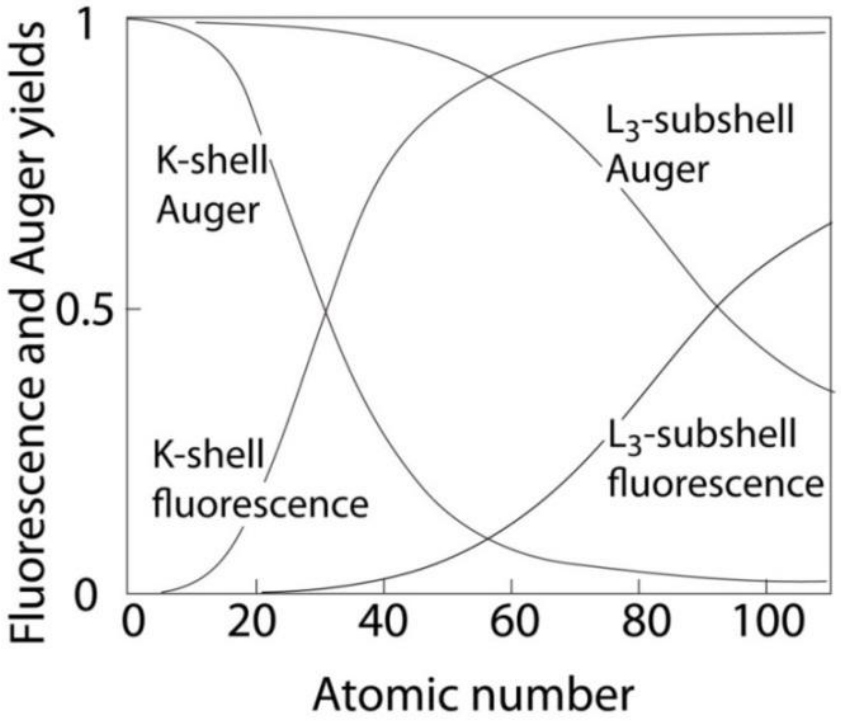

Figure 2.2. Fluorescence and Auger probabilities for the K, and L_3 shells depending on the atomic number. Adapted from reference [76].

2.2.1 X-Ray Absorption Spectroscopy (XAS)

X-ray absorption spectroscopy is a very powerful method to study the electronic properties of the materials. This method includes information about the dipole-allowed transitions between the core-levels states and unoccupied low-lying valence levels as it measures the absorption cross section as a function of incident photon energy. Fermi's Golden Rule can well describe the cross–section of electronic transitions between two states. In this model electrons are treated quantum mechanically and the light is modeled classically as a periodically varying perturbation with wave vector k, frequency ω and polarization to the atomic Hamiltonian. Absorption cross-section is expected to be linearly proportional to the transition probability from an initial state to a final state. Using the absorption cross section, a transition probability between a ground state energy E_g and a final state of energy E_f can be calculated shown in following equation 2.1 [77]. Here, Ω denote incoming photon energy, g and f refer to the initial ground and core excited final states, E_g is ground state energy, E_f is final state energy, $\vec{d}$ is the dipole moment, Γ is the life time broadening of final states,T is temperature, and $L(E_g+E_i-\Omega,\Gamma)$ represents the Lorentzian line shape function.

$$XAS(\Omega) = \sum_g f(E_g, T) \sum_f \left|\vec{d}_{fg}\right|^2 L(E_g+E_f-\Omega,\Gamma)$$

In soft X-ray regime, dipole allowed transitions are significantly higher in strength than other electronic transition (quadrupole or magnetic dipole transitions). Therefore, electronic dipole-allowed transitions dominate the absorption spectrum. An electric dipole transition will only take place if the dipole operator for corresponding transition is non-zero. If the cross-section for electric dipole transition operator is zero, the transition is dipole forbidden. This condition implies some selection rules for any XAS transition to take place [78]. These selection rules can be derived with regards to the conservation of orbital angular momentum quantum number (L), z-component of angular momentum quantum number (M) and spin quantum number (s). Considering the odd parity of dipole operator, a dipole transition must involve a change in orbital angular momentum of an electron but it does not affect the spin of an electron if the spin-orbit coupling is weak.

$$L = \pm 1$$
$$M = 0, \pm 1$$
$$S = 0$$

It is obvious from these rules that soft X-ray can be employed either as K-edge or L-edge spectroscopy. In K-edge spectroscopy only diploe-allowed transition from 1s to 2p levels are probed whereas in L-edge spectroscopy electronic transitions from 2p to 3d energy states are dominant.

For measuring absorption spectra, the incoming light is scanned through the binding energy of a core shell. The abrupt increase around a specific energy gives rise to an absorption edge. The resulting spectra can be subdivided into different branches namely NEXAFS and EXAFS. Extended X-ray absorption fine structure (EXAFS) is obtained by excitations from a core level to the continuum states far from the threshold, starting from 50 eV up to 1000 eV above the absorption edge [78-80]. The ionized electron is scattered by its neighbors probing the local geometrical structure. The energetic region up to 50 eV above the edge is of interest for studies on the unoccupied valence states and is known as near edge X-ray absorption fine structure (NEXAFS). XAS spectra can be measured by different techniques as transmission mode, total flourescence yield, total electron yield, and partial flourescence yield.

Transmission method is a direct measure for quantification of absorption cross-section where one would ideally measure initial photon intensity (I_0) and transmitted intensity (I) accurately. X-rays are strongly attenuated within a few micrometers of matter, thus the remaining intensity detected is very weak.

Total fluorescence yield is another method implemented in experiments to measure the XAS spectra. TFY is determined by summation over all possible transitions where the number of photons contributes to the spectrum. In this process photons are measured from all the possibly active radiative channels to get information for XAS. After the creation of a core-hole state by the absorption of an X-ray photon, the electron decays to fill the hole followed by fluorescence photon, which are not discriminated based on their wavelength. TFY measurements suffer distortions due to self-absorption and saturation effects [80-81].

In the total electron yield (TEY) method the number of electrons ejected from a sample are measured as a function of excitation energy. The quantity of ejected electron is proportional to the number of photons absorbed by the sample at a given energy. The removal of an electron from the sample causes electrons from the ground holder to flow into the sample resulting in current [82].

In partial fluorescence yield (PFY) method photons are discriminated based on their wavelenghts. The emitted photon is selected with a high energy precision, avoiding the contributions from the other undesired electronic transitions [83].

2.2.2 X-Ray Emission Spectroscopy (XES)

XES is a photon in/photon-out spectroscopy and is very useful giving element-specific information. It provides a complementary picture to the XAS revealing the nature of the occupied states. Like the XAS process, the XES is governed by dipole selection rules, and sensitive to the various final state symmetries in the valence region. XES can be described by a two-step model in which absorption and emission are considered as two decoupled processes.

Excitation of a core electron happens in first step (the absorption process) and second decoupled step explains the probability for the relaxation to the final state (the emission process). In non-resonant X-ray emission spectroscopy, the absorption of a photon above the ionization potential leads to the core ionization of the molecule, resulting in fluorescence, after electron from the occupied states relaxes into the core hole. Emitted photons can reveal valuable information about the electronic structure of the occupied orbitals of an atom or molecule. For resonant excitations known as RIXS, the two step model fails to explain spectra. As the intermediate states have a sufficient lifetime, two-step model is time independent and cannot provide information about the dynamics of a system.

2.2.3 Resonant Inelastic X-Ray Spectroscopy (RIXS)

In resonant inelastic X-ray scattering (RIXS) electron is excited not above the ionization threshold, but resonantly into an unoccupied bound state. In such a case several intermediate states are accessible making the actual intermediate state complicated. The intermediate core excited state, can decay to different final states, while the decaying channels interfere with each other. Therefore the resonant excitations are explained as an inelastic scattering process and the system itself in terms of a ground-state, final state and intermediate state is more accurately described within the framework of scattering theory. Resonant Inelastic X-ray Scattering (RIXS) is described by the Kramers-Heisenberg equation considering the summation upon all possible intermediate and final states, which is the main peculiarity of RIXS process making it one-step model [84].

$$\mathrm{RIXS}_{\Omega_0}(\omega)\sum_{g} f(E_g,T)=\sum_{f}\left|\sum_{i}\sqrt{\frac{\Gamma_i}{\pi}}\frac{(\vec{e}_1\vec{d}_{fi})(\vec{d}_{ig}\vec{e}_2)}{\omega+E_f-E_i-i\Gamma_i}\right|^2 G(\omega+E_f-E_g-\Omega_0,\gamma)$$

Here, Ω and ω denote the incoming and emitted photon energies; g, i, and f refer to the initial, core-excited intermediate, and valence-excited final states ($g \in \{f\}$), $\vec{e}_1$ and $\vec{e}_2$ are polarization vectors of emitted and absorbed photon, T is the temperature, E_g is initial state energy, E_i is intermediate core state energy, E_f final state energy, Γ is the element-specific lifetime broadening of the intermediate state, $G(\Omega_0,\gamma)$ is the Gussian profile and $\vec{d}$ is the dipole moment. Some of the unique features of RIXS are evident directly from the above equation. Compared to UV-Vis or infrared light spectroscopy, RIXS is a much superior technique. The selection rules in RIXS are different from UV-Vis. As the electric dipole operator acts twice because of two photon process, transitions with zero change in orbital angular momentum like dipole forbidden d-d transition are accessible as shown in Figure 2.3. RIXS is also element-selective and orbital specific technique providing higher energy resolution than UV-Vis. Therefore the information obtained from RIXS is complementary to the information from UV-Vis spectroscopy.

RIXS can also differentiate between the inequivalent chemical bondings sites, different valencies or inequivalent crystallographic positions of same element if the absorption edges in these cases are distinguishable. In addition, by tuning to electronic excitations at different X-ray edges of the same chemical element (Kβ emission and L-edge) a variety of information is collected. In comparison to XES, RIXS offers muh higher spectral resolution. The reason of sharper spectral peak width in contrast to XES is that the intermediate state no longer limits the spectral resolution but rather the final state lifetime. Final state does not contain a core hole, which results in a comparatively longer lifetime and therefore narrower peak width of the final state. Schematics of RIXS are shown in left panel of Figure 2.3 where the RIXS process can be divided into two sub-classes: resonant elastic X-ray scattering (REXS) and resonant inelastic X-ray scattering (RIXS). In inelastic scattering the excited electron will be left behind as a spectator (will not participate in emission itself), leaving the system in an excited state. The inelastic transitions are further categorized as d-d transition and charge transfer transition. Transitions in the range of 0-5 eV are termed as d-d transitions while charge transfer transitions often occur in the range of 4-15 eV. In charge transfer transitions, a neighboring electron from ligands participate in the decay channel by emitting a photon with less energy as shown in the right panel of Figure 2.3. The limitation of RIXS lies in its complex instrumentation. It requires an intense incident photon beam to collect a reasonable amount of scattered photons. This requirement for high photon flux can only be fulfilled at a synchrotron source.

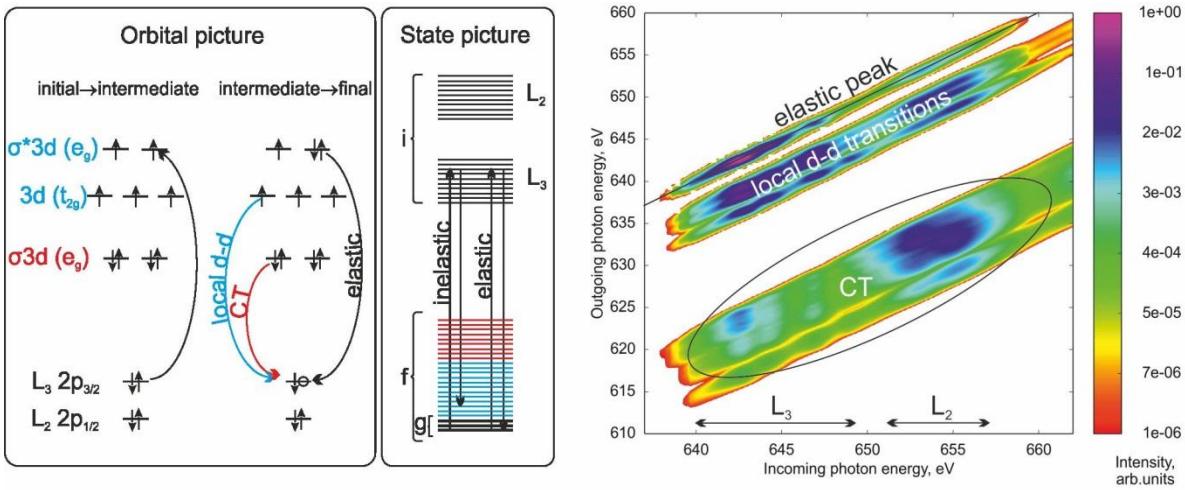

Figure 2.3. Left panel: The sketch of processes relevant to optical X-ray spectroscopy in the orbital and many-electron state representations. Different types of RIXS transitions are shown, i.e. elastic, local d-d reorganization, and charge-transfer (CT) together with the corresponding MOs. Right panel: General view of the 2D RIXS spectrum as calculated for $[Mn\ (II)(H_2O)_6]^{2+}$ showing different features. The details for the experimental results are discussed in Chapter 3.

2.3 Instrumentation for X-Ray Spectroscopy

The realization of X-ray absorption and resonant inelastic spectroscopy depends highly on the quality and sophistication of the setup used for experiments. Thus, the focus here is to explain the general experimental aspects and instrumentation requirements. An intense X-ray photon flux concentrated in a small spot size of a few micrometers is the main requirement of RIXS experiments as the fluorescence yield of shallow core holes is very low, and the emitted photons are detected in a small solid angle. Thus, the synchrotron radiation facilities producing soft X-rays in high brilliance are needed. The specific experimental setup and sample geometry is also a requirement in connection to complex RIXS experiments. Synchrotron radiation from the U41-PGM beamline at BESSY II of the Helmholtz-Zentrum Berlin in combination with an X-ray emission spectrometer is used for all the experiments discussed in this thesis. Details of all the instrumentation used in this work for performing XAS and RIXS experiments are presented herein.

2.3.1 Synchrotron Radiation: U41-PGM

Synchrotron radiation (electro-magnetic radiation) occurs, when charged particles (electron) moving nearly at the speed of light are radially accelerated by a magnetic field [85]. In synchrotron facilities like BESSY II initially a hot thermionic cathode emits electrons that constitute a beam of free electrons. The electrons are then inserted into the microtron which further accelerates the electrons within 50 ms with a repetition rate of 10 Hz with successive injection of electrons to 50 MeV, at which point they are injected into the booster synchrotron. In the booster synchrotron, electrons are accelerated on a circular path using a suitable RF field which synchronizes it carefully with electron motion.

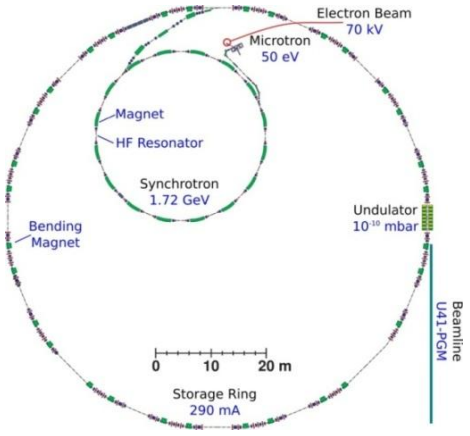

Figure. 2.4. A schematic presentation of synchrotron facility taken from reference [86]. An accelerator injects the electrons into a booster ring where they are accelerated before being injected in to storage ring. The storage ring has a number of straight sections connected through bending magnets.

High frequency resonators (HF resonators) with a suitable temporal coupling with the magnets, further accelerate the electrons to threshold energy of 1.72 GeV to obtain relativistic electrons with a velocity up to 0.99c before injected into storage ring. The major part of BESSY II is the storage ring with a circumference of 240 meters field. Being a third generation light source BESSY II has high brilliance as its main advantages. In storage ring, a high electron flux with high temporal stability is created by bending magnets and undulators. Maintaining the trajectory, electrons inside storage ring are collected as packets, so-called bunches. Successive injection of electrons into storage ring can make maximum current stabilized at 300 mA. After the initial stage of injection, the current decays at a slow decay rate of several hours, and this mode of operation is termed as 'decay mode'. Recently a new 'top up' mode is adopted at BESSY II, where the electrons are injected every minute into the storage ring. This thesis contains some experiments performed in decay mode while others in top up mode (details are given in Chapter 3 and 4).

It is known that moving electrons produce Bremsstrahlung radiation when decelerated. The electrons passing through an insertion device loses energy in the form of Bremsstrahlung radiation which is collected by a beamline. A beamline is always tangential to storage ring and comprises of an insertion device (ID) and a monochromator and focusing optics. The wigglers and undulators act as insertion devices of the storage ring and can be considered as the actual radiation sources. An undulator comprises of an alternating arrangement of the bending magnets. The alternating magnetic field of each undulator changes the electron's trajectories causing them to oscillate, which in turn produce many cones of light tangential to the storage ring. These radiations overlap coherently because the accurate phase superposition of their radiation lobes give sharp maxima that are the undulator harmonics. Energy loss of electrons due to this Bremsstrahlung process in the storage ring is compensated by high frequency resonators situated on a short linear section.

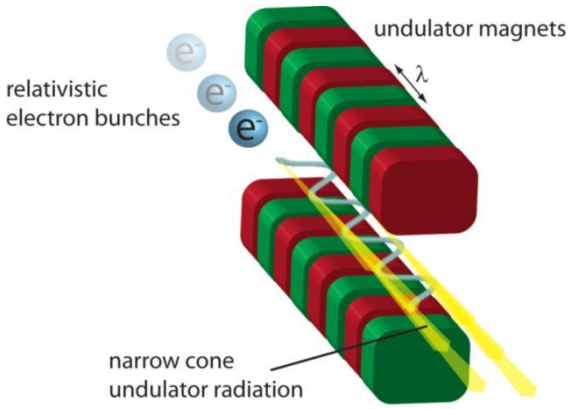

Figure 2.5. Periodic arrangement of magnets of an undulator in order to produce synchrotron radiations. Adapted from [87].

Undulators provide several excellent properties such as high brilliance and polarized light. In order to achieve the high brilliance of soft X-rays, a high vacuum of 10^{-10} mbar is maintained. However the light coming out of an undulator needs further monochromatization and optics to get a focused beam before being used in experiments. A schematics showing principle optical elements of the U41-PGM beamline at BESSY II is drawn in Figure 2.6. It consists of gold coated optical devices in grazing incidence to obtain a collimated beam. It is operated by the Helmholtz-Zentrum Berlin and was used for all the experiments in this study. The U41 undulator consists of 81 magnets with a period of 41.2 mm. It is located in the low beta section of storage ring where electrons have a small transverse extension. The combination of location and high number of magnets of the undulator provide U41 one of the highest brilliance available at BESSY. A pressure of 10^{-10} mbar is maintained at the undulator section. Radiation from the undulator beam coming from an entrance slit (not shown in the Figure) is focused by a toroidal mirror (M1) horizontally and collimates the radiation vertically. After mirror M1 collimated light is dispersed through a monochromator consisting of a plane grating (G) known as a Peterson plane grating monochromator (G), which creates a moderate energy resolution of the photon beam and high photon fluxes. The groove density of monochromator is about 600 mm^{-1}. After the grating, the beam is deflected by a plane mirror (M2).

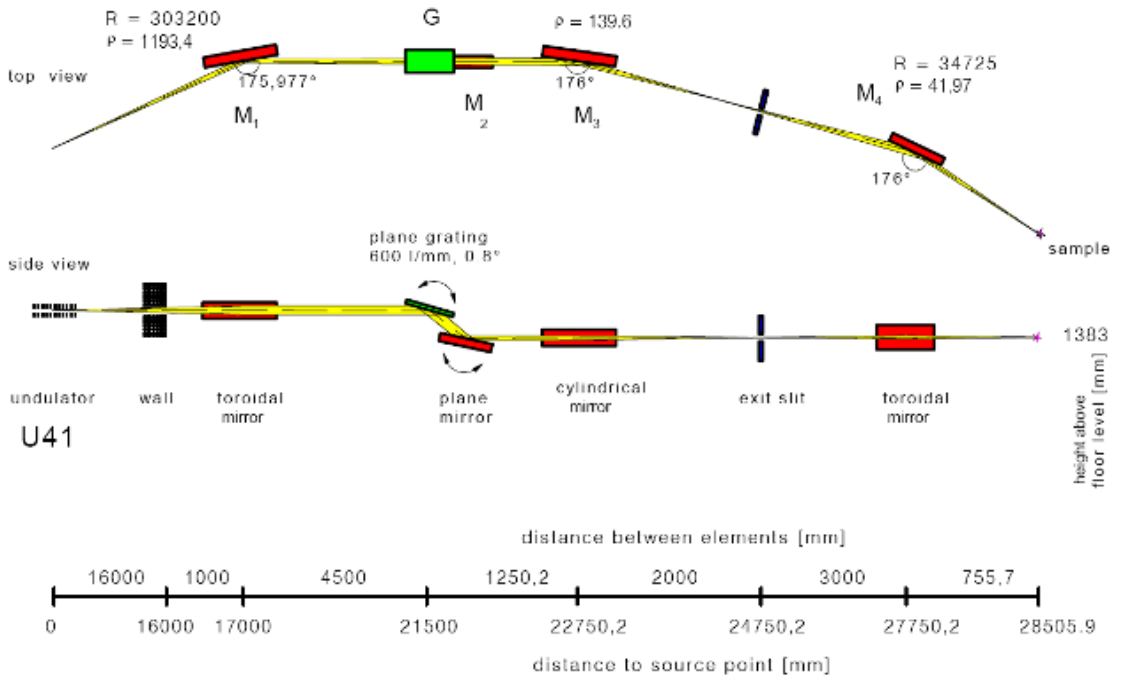

Figure 2.6. Schematic representation of U41-PGM beam line optics at BESSY II taken from reference [88]. The beam line elements consist of a collimating mirror (M1), monochromator (a combination of a grating and plane mirror (M2)), a cylindrical focusing mirror (M3), an exit-slit and a refocusing mirror (M4) to collimate the soft X-ray beam.

Both the grating and the plane mirror are movable and work in combination, allowing varying wavelength to pass the exit slit. Collimated beam from M2 passes through cylindrical mirror (M3) before the exit slit. The exit slit can be varied between different slit sizes of 20, 40, 100 200, 500, 2000 and 3000 µm to obtain a required focus size, flux and resolution. A compromise between a suitable photon flux and resolution has to be found. On the one hand, exit-slit's size must be taken into account, as a larger slit gives less spectral resolution but higher photon flux while on the other hand, a smaller slit gives a higher spectral resolution. Therefore, the exit-slit can be changed to adopt the experimental needs of a required resolution and a cross-section. After the exit slit the refocusing chamber is located where a torodial mirror (M4) refocuses the light towards the experimental chamber. The experimental chamber is connected at the end of the beamline with a base pressure of 10^{-7} mbar which is sufficient for the experiment. The pressure gap of 10^{-10}-10^{-7} between beamline and the experimental chamber is bridged by differential pumping from the beamline to the chamber. In general the beamline provides an energy range from 170 eV to 1800 eV. Overall the design of U41 PGM allows for a moderate energy resolution over a soft X-ray range.

2.3.2 Experimental Setup: X-Ray Spectrometer

All the XAS and RIXS measurements for this study are performed at the LiXEdrom spectrometer setup. This setup was initially designed to perform soft X-ray spectroscopy on liquid samples. However solid samples were also measured successfully with a little modification in sample holder. The setup consists of a main experimental chamber, a grating chamber and a detector. The sample holder can be moved in 3 dimensions to adjust the suitable sample position in front of detector. Main chamber maintains a pressure of 10^{-7}. The sample mounted on a copper holder is excited by X-rays entering in main chamber leaving the sample in an excited or an ionized state. X-ray absorption can be measured via the total fluorescence yield mechanism with an InGaAsP photodiode or in total electron yield mode by recording the drain current from sample. TFY as well as TEY currents are read out with a Keithley multimeter. After the X-ray beam hits the sample in the main chamber, the X-ray emission was measured using an X-ray spectrometer consisting of an energy dispersive grating and a spatially resolving detector. The setup has four different gratings going from 20 eV up to more than 1000 eV mounted on a revolver shaped grating holder that can rotate exposing one grating at a time. Depending upon the energy requirement of our experiment, a grating with a radius of 7.5 meters and a line density of 1200 mm^{-1} covering an energy range of 400-1000eV has been used to measure RIXS at the Mn L-edge. Diffraction lines originating from the source will focus on this circle of radius R, called the Rowland circle. Depending upon their wavelength, these lines will be dispersed on the Rowland circle producing an energy resolved spectrum as shown in Figure 2.7.

After dispersion from the grating emitted light reaches at the detector which is an assembly of a deflection plate, two dimensional multichannel plates (MCP) from VG Scienta, a phosphorous screen and a CCD camera (designed to move to access the different focus points on the Rowland circle). In order to achieve a Rowland circle geometry defined by R. H. A. Rowland in 1882, a spherical grating of radius 2R and the source has to be on a circle of radius R [89]. Diffraction lines originating from the source will focus on this circle of radius R, called the Rowland circle. The spherical grating serves for the diffraction and the focusing of light while minimizing the further needs of optical elements making it a widely used method even after 100 years of its discovery. The spatial resolution of the spectrometer is a function of the source size (entrance slit to the spectrometer), grating size, radius, groove density and the quality of the grating. High line density of grating provides a high resolution to spectra.

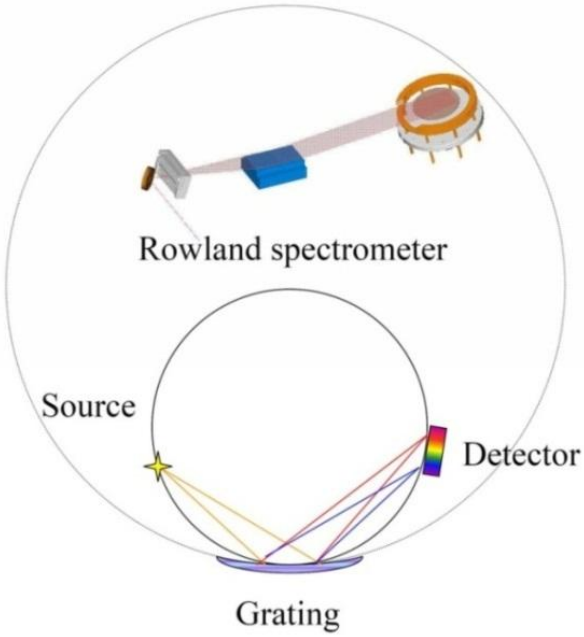

Figure 2.7. Illustration of the layout of the Rowland circle spectrometer reproduced from reference [90]. The radiation from a sample as point source is dispersed with a spherical grating at the Rowland circle.

The MCP consists of two multi-channel plates, first of which is coated with cesium iodide to increase the conversion efficiency and is connected to a high negative voltage of about -1.67 kV while the second plate is grounded. A negatively charged deflection plate serves to push the secondry electrons towards the first MCP plate. The plates are connected with highly resistive semiconductor material with small tubes (the micro-channels) passing through it. When a photon hits the wall of a channel, photoelectric effect ejects an electron, which then is accelerated towards the detector. Collision of electron with these micro channel walls produces secondary electrons. The MCP acts as a position resolving electron multiplier.

The secondary electrons are drifted to the bottom of the MCP due to potential difference between the two plates. The final electron shower is attracted to a positively charged fluorescence screen by being hit produces phosphorescence, which is captured by a CCD camera (charge-coupled device (Basler Scout 17FM), with 1392 x 1040 pixels resolution and maximum frame rate of 17 frames per second.

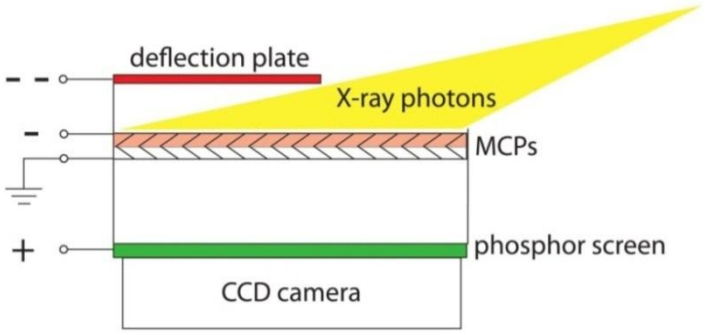

Figure 2.8. Detector assembly of the LiXEdrom [91].

2.4 XAS and RIXS Measurements

The parameters of the U41-PGM adopted for XAS and RIXS experiments are discussed briefly in this section. XAS and RIXS experiments were performed in the LiXEdrom experimental station at the U41-PGM beamline, at the BESSY II synchrotron facility. In all performed experiments, an exit-slit size of 20 microns was usually used, as this gives a high resolution and suffient intensity with a minimum possible exposure of the sample to X-ray. Third harmonic of the undulator is always used for the Mn L-edge. A compromise between energy resolution and incoming intensity is made by changing the *cff* value. Due to the specific characteristics of the U41-PGM beamline, the *cff* value is less than one. For these experiments, the value of *cff* was chosen between 0.35-0.65 depending on the sample measured. For heat treated catalysts discussed in Chapter 4, 4^{th} diffraction order was used to minimize the flux up to a minimum level as the samples were highly sensitive to radiation damage. However the nafion doped catalysts showed resistance to radiation damage and could be measured with 1^{st} order of diffraction of beam line. Beamline apertures were decreased to minimum possible values to further minimize the flux of incoming beam. Sample XA spectra were obtained by driving the monochromator throughout the energy region of interest and recording the electron current in the sample or fluorescence signal. The RIXS spectra were recorded in the XES spectrometer, monitoring the 1^{st} or 2^{nd} order emitted light. The voltages of the deflection plate, MCP and acquisition time for CCD camera were optimized depending on the sample emission.

2.5 RIXS Data Correction

Before analyzing and interpreting the experimentally obtained spectra, a treatment of the data, e.g., normalization or image correction is necessary. In the U41 PGM beamline it is possible to measure refocusing mirror current I_0. All the spectra measured were normalized to the mirror current (I_0) for compensating intensity variations. The normalization was achieved by dividing the sample current (I) to the mirror current (I_0) when the synchrotron radiation intensity was not uniform. Fluorescence photons from the grating slit hit the detector in various vertical dimensions due to the spherical shape of the grating. As a result of this the image produced on the outer edges of detector will be curved towards lower energies. The 2-dimensional picture in Figure 2.9a shows that each line belonging to a specific energy is curved. Since the channels of every vertical column in picture are summed up to obtain the spectrum, the curvature of the lines leads to a broadening of the peaks. Therefore a curve correction is applied. The position of the elastic peak was used for energy calibration.

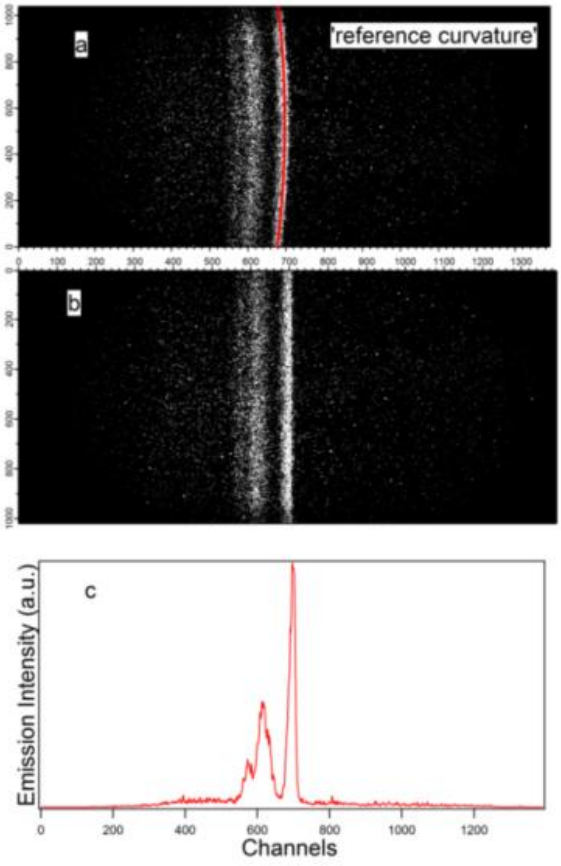

Figure 2.9. A picture recorded by the CCD camera is presented for a Mn catalyst. It can be read out as a matrix containing the entries of 1392 x 1040 channels in the upper panel. The spectrum, shown in lower panel b is obtained after applying the curve correction in the upper panel a. The panel c is the spectrum obtained after summing up intensities in panel b.

Chapter 3

Electronic Structural Insights into Manganese Water Oxidation Catalyst Doped in Nafion

3.1 Introduction

Because a manganese cluster is the only known system to catalyze water oxidation in nature, [43, 92] manganese catalysts have been attracting much attention [42, 43, 92-95]. This Chapter investigates Mn complexes doped into Nafion films deposited on conductive electrodes as water oxidation catalysts [42, 42, 55, 92, 93, 95]. L-edge XAS and RIXS experiments are performed *ex situ* at different stages of the catalyst generation and water oxidation cycle on the species namely: $[Mn(OH_2)_6]^{2+}$, the dinuclear complex $[Mn_2O(OAc)_2L_2]^{2+}$, and, $[MnL(OMe)_3]^{+}$ (where L= Me_3TACN/1,4,7-trimethyl-1,4,7-triazacyclononane in both cases). For clarity, these complexes will be referred to as Mn (II), Mn (III) and Mn (IV), respectively, as shown in Figure 3.1. The chapter is divided into three parts; first section provides insight into the local HOMO-LUMO gap of Mn (III) complex by XAS and RIXS spectroscopy. XAS spectra were measured through total flouresence yield. In the second section, a comparison of Mn (III) with a series of water splitting catalysts like Mn (II) and Mn (IV) is made again through XAS and RIXS techniques. The reason to choose Mn (IV) and Mn (II) is that former was reported as the second highest efficient catalyst and later as the least efficient catalysts of the series for water splitting in comparison to Mn (III) (reported as most efficient catalysts). Spectra were measured in total electron yield to get saturation free spectra in order to find out the specific oxidation states present in different stages of water oxidation cycle for each catalyst. Fitting of experimental XAS sepctra were performed through linear comnbination of reference oxides. In last section, theoretical calculations are presented to further reaveal the electronic structure of local Mn 3d for these catalysts.

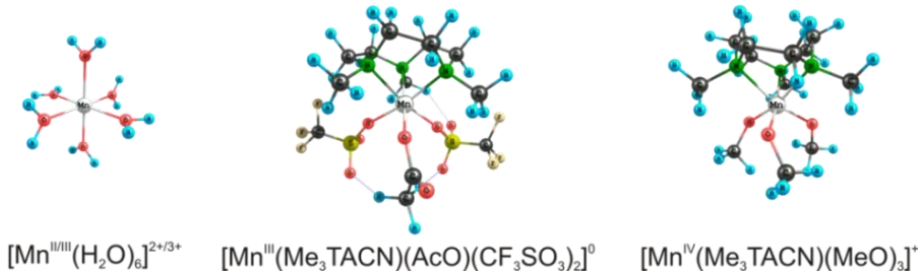

Figure 3.1. Structures of manganese complexes used as water oxidation complexes.

These are the reduced (II) and oxidized (III) forms of the manganese hexaaqua complex ($[MnII/III(H_2O)_6]^{2+/3+}$), $[MnIII(Me_3TACN)(AcO)(CF_3SO_3)_2]^0$, where two mono-coordinated $CF_3SO_3^-$ ions are modeling a Nafion environment, and finally the Mn (IV) compound $[MnIV(Me_3TACN)(OMe)_3]^+$.

3.2 Enhancing the Catalytic Activity by Narrowing Local Energy Gaps of Mn (III) Catalyst Doped into Nafion

This part of thesis is taken from following publication.

Enhancing the Catalytic Activity by Narrowing the Local Energy Gaps – XAS and RIXS Studies of a Manganese Water Oxidation Ctalyst.

Jie Xiao, **Munirah Khan**, Archana Singh, Edlira Suljoti, Leone Spiccia, and Emad F. Aziz.

ChemSusChem. 8 (2015) 872–877. DOI:10.1002/cssc.201403219

It is reported that a Mn dinuclear complex $[Mn_2O(OAc)_2L_2]^{2+}$ is decomposed into Mn^{2+} species upon doping into Nafion. A birnessite like manganese oxide is formed after the electro-oxidation of Mn^{2+} species. The anionic sulfonate groups of the Nafion matrix are important such that they allow ion exchange of cationic Mn species in the films, which are then converted into active catalysts [42, 43, 92, 93, 95]. Moreover, these films have proven to be an excellent medium for exploring the effect of morphology and surface area on catalytic activity [55, 95]. An intriguing feature of this catalyst was the enhancement in catalytic activity induced by visible light irradiation [81, 82, 84, 95, 96]. Light was proposed to promote oxygen release and to result in formation of Mn^{2+} species. Many techniques, including photoelectron spectroscopy (PES), UV/Vis spectroscopy, STM imaging, and electron energy loss spectroscopy (EELS), have been employed to study transition-metal oxides applied as water oxidation catalysts [97-99]. Most of these measurements involving the transportation of electrons, however, are not practical when assessing bulk properties (e.g., Mn catalyst inside the Nafion matrix), but better suited to heterogeneous catalysis studies (i.e., thin film or particle catalyst adsorbed on substrate) due to the short mean free path of the electrons. Other techniques, such as K-edge X-ray absorption spectroscopy (K-edge XAS), electron paramagnetic resonance (EPR), energy dispersive X-ray spectroscopy (EDX), and TEM, can provide information about the spin state and morphology of MnO_x formed inside the Nafion matrix, [45,57, 95] but not about the detailed local valence electronic structure of catalytic sites (metal-ion sites), which is fundamentally connected to catalytic activity.

For Mn compounds doped into the Nafion matrix, element-specific photon-in photon-out measurements in the soft X-ray range would provide valuable information about the local electronic structure of Mn catalytic sites. The lowest energy-loss feature in RIXS measurements represents the lowest excitation energy from the local HOMO to the LUMO, and can thus be used to characterize the local energy gap [96]. XAS and RIXS measurements were previously applied on the Mn K-edge, but resolution was not sufficient to reveal the fine electronic structure of 3d valence levels and the restriction of the dipole-selection rule between s and d orbitals severely reduced the spectrum intensity [94, 95, 97-102]. Measurements on the Mn L edge, however, better resolve the Mn 3d electronic structure and are sensitive to the symmetry and coordination of the ligands [102-108]. In this section, a study of water oxidation catalysts is performed in an electrolysis environment under realistic stimulations (electrical bias and visible light applied simultaneously) by the RIXS technique, and significant information about the Mn electronic structure is revealed. Herein, the electronic structure of the catalyst generated with Nafion films from a series of Mn complexes is investigated. Detailed information about the Mn 3d configuration is revealed by X-ray absorption spectroscopy (XAS) and resonant inelastic X-ray scattering (RIXS) measurements at the Mn $L_{2,3}$-edge. In particular, the local energy gap that significantly influences catalytic efficiency is uncovered by the RIXS method.

3.2.1 Sample Preparation

All reagents and solvents were purchased and used as received. Purity was as follows: $Mn(ClO_4)_2.6H_2O$ (99%, referred to as Mn (II), Nafion perflourinated resin solution (5 wt. % in lower aliphatic alcohols containing 15-20% water), acetonitrile (99.9%), perchloric acid ($HClO_4$, 0.1 M), and Na_2SO_4 (ACS reagent, 99%). The manganese oxide powders of MnO, Mn_3O_4, Mn_2O_3, MnO_2 and birnessite were purchased from Sigma Aldrich with purity more than 99.9%. The $[Mn_2O(OAc)_2L_2](ClO_4)_2$ complex, referred to as Mn(III) where L = Me_3TACN (1,4,7-trimethyl-1,4,7-triazacyclononane), OAc = μ-CH_3COO^-) was prepared as described in reference [109]. Birnessite was prepared according to the already proposed procedure [110]. Depending upon the number of Mn atoms in each complex; 5 ml of equimolar solutions of the three compounds with concentrations of 8mM for $Mn(ClO_4)_2.6H_2O$, 4mM each for $[MnL(OMe)_3]^+$ and $[Mn_2O(OAc)_2L_2](ClO_4)_2$ in acetonitrile were prepared. A known volume of Nafion solution (10 µL) was cast onto 1cm^2 graphite electrodes, dried in air and then in an oven at 120 °C for 20 minutes. These Nafion coated electrodes were impregnated with the Mn compounds by dipping them in precursor solution for 20 minutes. The impregnated films were washed with deionized water and then air-dried. A potential of 1.0 V versus Ag/AgCl (3M NaCl, 0.200V vs. NHE) electrode was applied to the Mn-doped in nafion coated graphite films (anodes) using a platinum counter electrode in a conventional three-electrode electrochemical cell for 40-60 minutes.

An aqueous solution containing 0.1M Na_2SO_4 (pH 6.5) was used as the electrolyte. For the last step in the sample preparation visible light illumination by a 50W tungsten lamp was also applied with or without the simultaneous application of an electrical potential on films. All films were washed with de-ionized water and air-dried prior to the measurements.

3.2.2 Experimental Methods

XAS and RIXS experiments were performed in the LiXEdrom experimental station at U41-PGM beamline, at BESSY II synchrotron facility. Details of the BESSY II synchrotron and LiXEdrom end-station have been described in Chapter 2. Mn-doped nafion films deposited on graphite anodes were mounted on a sample holder with adhesive copper tapes in a vacuum chamber with base pressure of 10^{-8} mbar. X-ray absorption spectra were measured in total fluorescence yield (TFY) mode. TFY spectra were measured using a photodiode mounted in the same vacuum chamber close to samples. X-ray absorption spectra, in total electron yield, were measured with the conventional method of sample drain current. Quick energy scans of 1 sec per point were employed to reduce the total exposure time of sample to radiations in order to avoid any radiation damage of active catalyst caused by soft X-rays. The incoming synchrotron beam was impinging the sample at 45º angle, and the emitted (RIXS) photons were detected with an X-ray emission spectrometer (XES) mounted normal to the synchrotron beam. RIXS spectra were recorded with a 1200 mm^{-1} grating resolving emitted photon energy and a multichannel plate/phosphor screen/CCD camera assembly amplifying and detecting signal. Each measurement was repeated several times at different spots on the same sample and on several identically prepared samples to test for sample homogeneity and to assure experimental reproducibility (Appendix A.1).

No variation between the XAS spectra was observed during the repeated measurements on the same sample spot and fresh sample spots for various Mn (III) samples, indicating little beam damage from synchrotron light (Appendix A.2). Birnessite samples showed radiation damage and the synchrotron flux was strongly reduced until the damages were minimized (Figure A.2.3). One may argue that the Mn (III) samples could be already damaged by the synchrotron radiation once the sample was placed under the synchrotron light before the first measurement could even start, since it is well known that Mn complexes are sensitive to intense x-ray beam which can quickly reduce Mn from higher oxidation states to Mn^{2+}. If it is the case, the sample damage has to be stabilized very quickly since no further XAS spectrum change had ever been observed, as mentioned above. Significantly reducing photon flux from beamline would mitigate this instant damage on Mn (III) samples and produce different XAS spectra. However, almost identical XAS spectra (with less overall intensity) were observed after the photon flux was reduced less than 5% of the original one.

A gradual change of the XAS spectra was observed on a pure Birnessite sample during the repeated measurements, but not for various Mn (III) samples, which indicates that the beam damage on Mn (III) samples, even if exits, is very unlikely so instantaneous. The total fluorescence yield (TFY) mode has its limitations when used to represent the real XAS in transmission mode. Self-absorption and saturation effects are the major obstacle damaging the linear proportionality of TFY to the true XAS in transmission mode, resulting in distorted relative peak intensities within a spectrum. So, comparison of TFY spectra with those in literature measured with different modes (like total electron yield, TEY) and under different sample conditions is usually not practical. The intensity ratio change within spectra, however, still has physical significances.

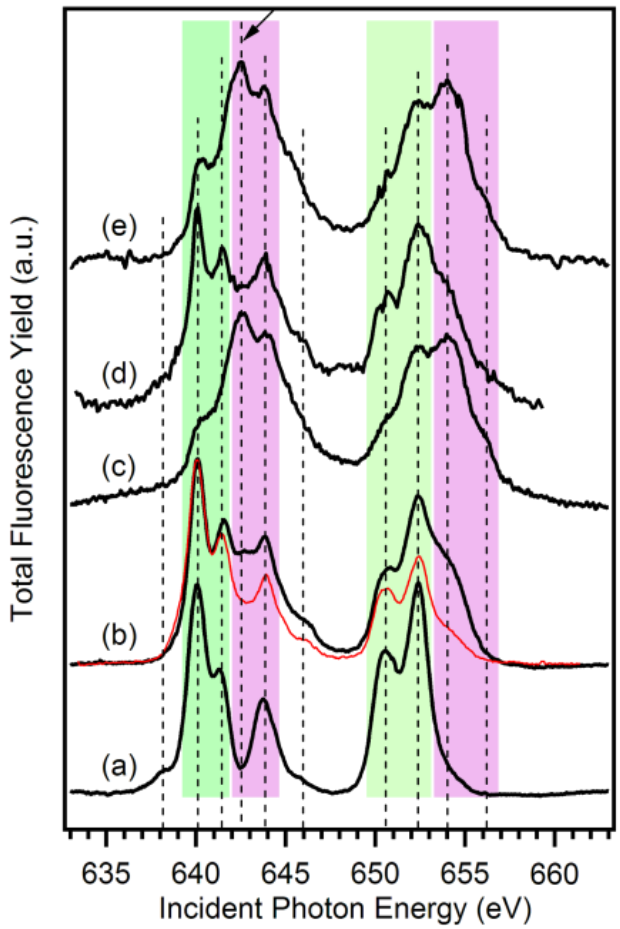

Figure 3.2. Comparison of total fluorescence yield (TFY) on Mn $L_{2,3}$-edge of Mn (III) complex (a) pristine Mn (III) powder, (b) as-doped Mn (III) (black) and $[Mn(OH_2)_6](ClO_4)_2$ (red) in Nafion, (c) Mn (III) doped in Nafion with potential applied for one hour, (d) Mn (III) doped in Nafion with potential applied followed by 16 hours of light illumination, and (e) Mn (III) doped in Nafion with simultaneous application of potential and light for 10 hours.

3.2.3 Results and Discussion

A powder sample of the Mn (III) complex was measured to establish a Mn^{3+} reference spectrum (Figure 3.2a). After doping Mn (III) into Nafion, two intense peaks, which are absent in Figure 3.2a, are observed in Figure 3,2b at 642.5 (L_3-edge) and 654.0 eV (L_2-edge). A pre-edge feature at 638.2 eV present in the powder Mn (III) spectrum (Figure 3.2a) is no longer present. The absence of this pre-edge feature in Figure 3.2b may be indicating a weaker ligand field for doped Mn (III) relative to the pristine Mn (III) complex [102, 110] due to the probable distortion of the original symmetry and changes in the ligand field. As shown previously in EPR measurements, the Mn (III) complex is reduced to Mn^{2+} species when doped into the Nafion film [43, 95]. Relative to the spectrum of $[Mn(OH_2)_6](ClO_4)_2$ doped Nafion (pure Mn^{2+} in Nafion, red trace in Figure 3.2b), there is a significant discrepancy between the reduced Mn (III) (black trace) and the original Mn^{2+} (red trace) spectrum, even though both Mn species share the same oxidation state (2+), indicating that other factors, besides the Mn oxidation state, also influence the final spectrum. So, the change from Figure 3.2a to 3.2b, especially the two additional peaks at 642.5 and 654.0 eV within the L_3 and L_2-edge, respectively (Figure 3.2b), cannot be solely due to the reduction of the Mn oxidation state. Differences in the ligand fields surrounding Mn species, arising from the presence of Me_3tacn ligands (originating from the Mn (III) complex) and distortions in the ligand field caused by the interactions between Mn species and Nafion sulfonate groups could also account for the black trace in Figure 3.2b. Therefore, it can be postulated postulate that the significant differences between Figure 3.2b (black trace) and 3.2a are due partly to different oxidation states, and also to variations in the ligand field around Mn centers before and after doping in Nafion.

After the application of an electrical potential of 1.0 V (vs. Ag/AgCl) to the Mn (III) doped Nafion film (deposited on graphite) in an aqueous electrolyte containing Na_2SO_4 (0.1M), the intensities of the two peaks at lower excitation energies within the Mn L_3-region (i.e., at 640.1 and 641.4 eV inside the green band) are reduced, whereas the two peaks at higher excitation energies (i.e., at 642.5 and 643.9 eV inside the pink band) increase in intensity as shown in Figure 3.2c relative to 3.2b. This is also the case for the Mn L_2-region: the peaks at 650.6 and 652.2 eV (green band) diminishes in intensity, whereas those at 654.0 and 656.1 eV (pink band) increase. This change is typically observed when the element in question (Mn in this case) is oxidized [95, 110]. It is consistent with previous observations that the electrical potential induces the oxidation of Mn^{2+} to a high-valent $Mn^{3+/4+}$ material (birnessite), which actually catalyzes water oxidation [43, 92, 93]. Visible light illumination of the electrolyzed Mn (III) doped Nafion film for 16 hours almost completely reverses the effect of the electrical potential when comparing Figure 3.2d with 3.2b.

In Figure 3.2d, the two peaks at lower excitation energies inside the green band increase in intensity, whereas those at higher excitation energies inside the pink band decrease relatively when compared with Figure 3.2c. These intensity changes move the Mn state towards that in Figure 3.2b (i.e., the state before the potential is applied), but the reduction to Mn^{2+} is actually not 100 % complete as observed in previous EPR measurements [95].

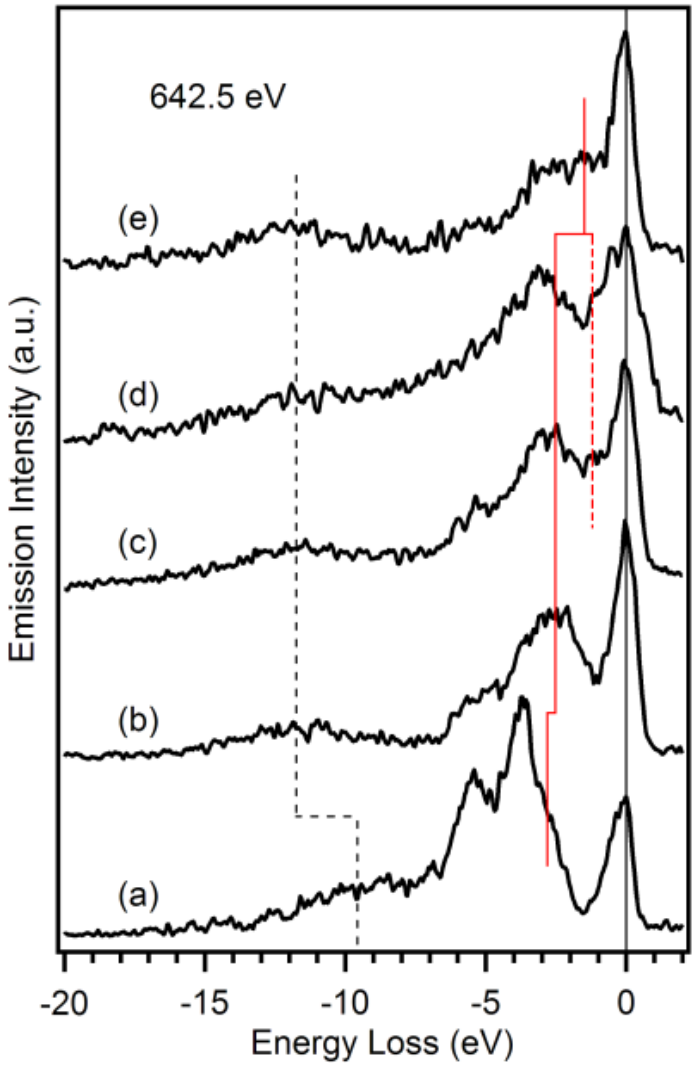

Figure 3.3. RIXS comparison at the excitation energy 642.5 eV of Mn (III) complex: (a) pristine MnIII powder, (b) as-doped Mn (III) (black) and $[Mn(OH_2)_6](ClO_4)_2$ (red) in Nafion, (c) Mn (III) doped in Nafion with potential applied for one hour, (d) Mn (III) doped in Nafion with potential applied followed by 16 hours of light illumination, and (e) Mn (III) doped in Nafion with simultaneous application of potential and light for 10 hours.

Because in a functional photo-electrochemical cell an electrical potential and visible light are applied simultaneously to have a sustainable catalytic activity, the Mn (III) doped Nafion films were then studied under both treatments for various time periods. The resultant X-ray absorption (XA) traces for the 1h treatment (not shown herein) is similar to that obtained after 10h (Figure 3.2e, indicating that the system essentially operates under steady-state conditions on the application of both treatments. The spectrum after 10h of treatment (Figure 3.2) shows that the relative peak intensities more closely resemble those in Figure 3.2c than in 3.2d, indicating the dominant effect of the electrical potential when two treatments are applied simultaneously.

The slight enhancement of the peak at 640.1 eV in Figure 3.2e relative to the corresponding feature in Figure 3.2c shows that visible light illumination partially counteracts the effect of electrical potential when the two treatments (potential and light) are applied simultaneously. The most significant change in the Mn L_3-region of the spectrum is the emergence of an absorption feature at 642.5 eV (compare Figure 3.2b, black trace, with 3.2a), which is indicative of a ligand-field change for the Mn (III) doped Nafion films besides the reduction of the Mn oxidation state. Another indication of the ligand-field change when Mn (III) is doped into Nafion is the aforementioned disappearance of the pre-edge feature at 638.2 eV.

The oxidation-state change from Mn^{3+} to Mn^{2+} cannot be solely responsible for the intense feature at 642.5eV for the black trace in Figure 3.2b because the red trace in Figure 3.2b has a different intensity at this energy. This energy was therefore chosen as the excitation energy for RIXS analyses (Figure 3.3). Significant differences in the RIXS loss-features are apparent when comparing Figure 3.3b with 3.3a, which is expected based on the spectral differences shown in Figure 3.2b (black trace) and 3.2a. The energy-loss features up to -6 eV are often categorized as d-d excitations, whereas broader peaks with larger energy losses at -8 to -12eV are considered to be charge-transfer transitions [105, 106, 108].

Two apparent changes occur in going from the pristine Mn (III) complex (Figure 3.3a) to the Mn (III) doped Nafion films (Figure 3.3b) in both the d-d transition and charge-transfer regions: (1) low energy-loss features up to -3eV within the d-d transition region are enhanced, whereas, in comparison, the higher energy-loss features at -3 to -6eV are suppressed, and consequently the lowest energy-loss feature moves closer to the elastic peak, marked by the shift of solid red lines in Figure 3.3a and 3.3b; (2) the charge-transfer feature at about -9.6 eV in RIXS analyses of the pristine Mn (III) precursor (Figure 3.3a) shifts to about -11.8 eV when Mn (III) is doped into Nafion (Figure 3.3b), as marked by black dashed lines.

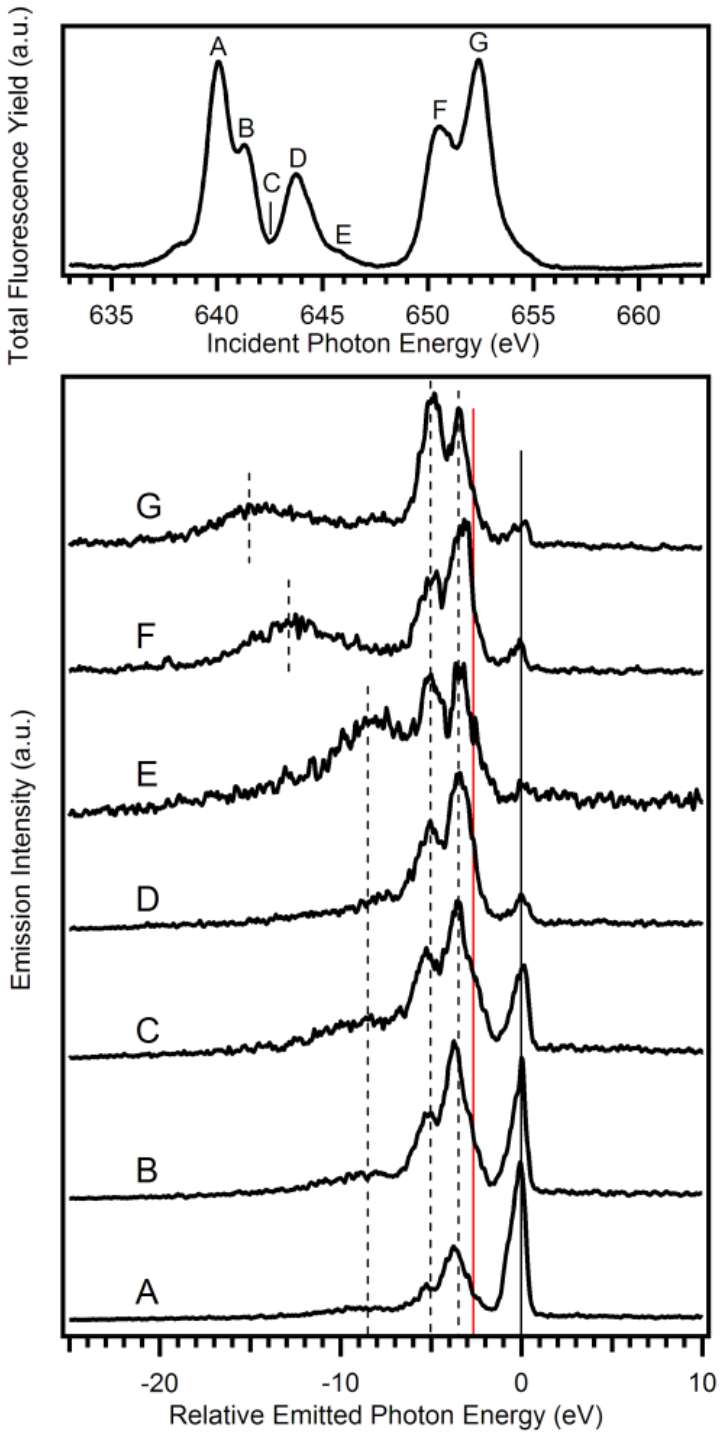

Figure 3.4. Total fluorescence yield (TFY) (top, same as Figure 3.2a) and RIXS loss spectra on Mn L-edge of pristine Mn (III) molecules.

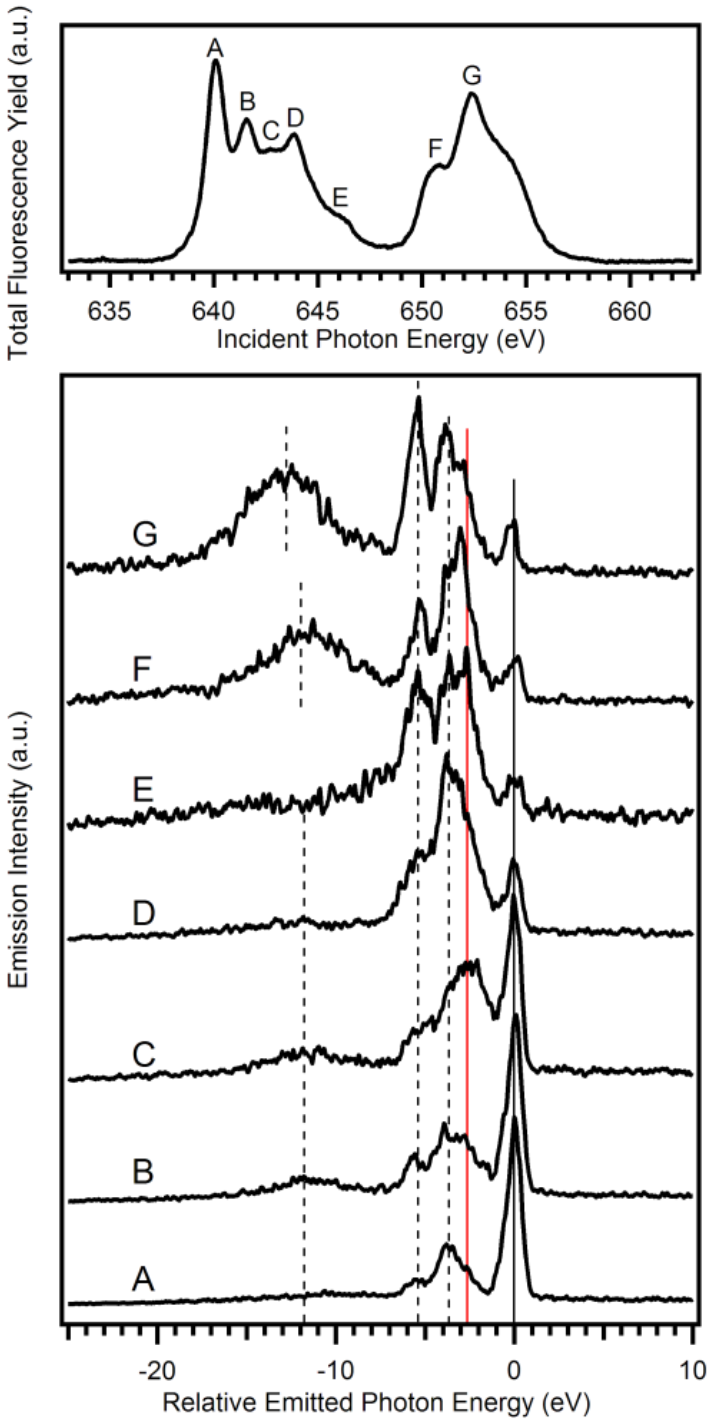

Figure 3.5. Total fluorescence yield (TFY) (top, same as Figure 3.2b) and RIXS loss spectra on Mn L-edge of as-doped Mn (III) in Nafion.

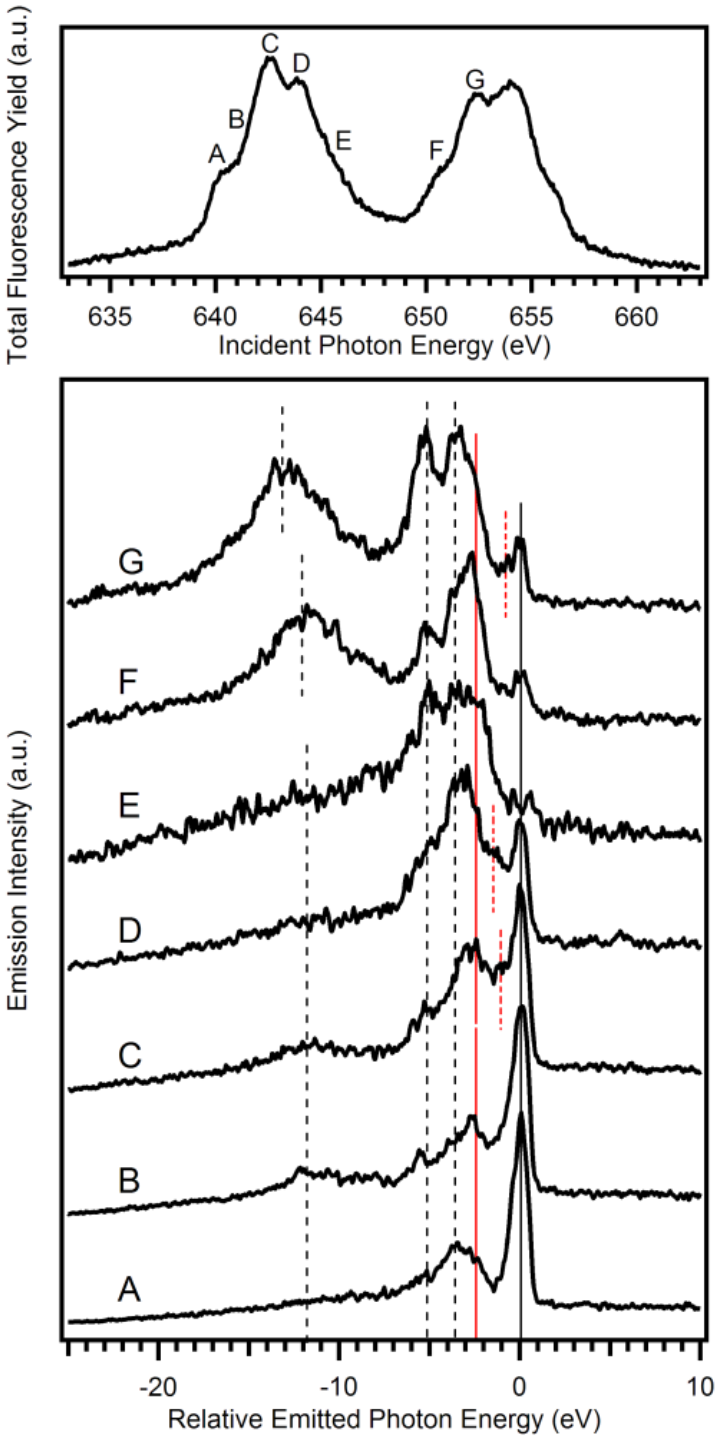

Figure 3.6. Total fluorescence yield (TFY) (top, same as Figure 3.2c) and RIXS loss spectra on Mn L-edge of doped Mn (III) in Nafion with potential applied for one hour

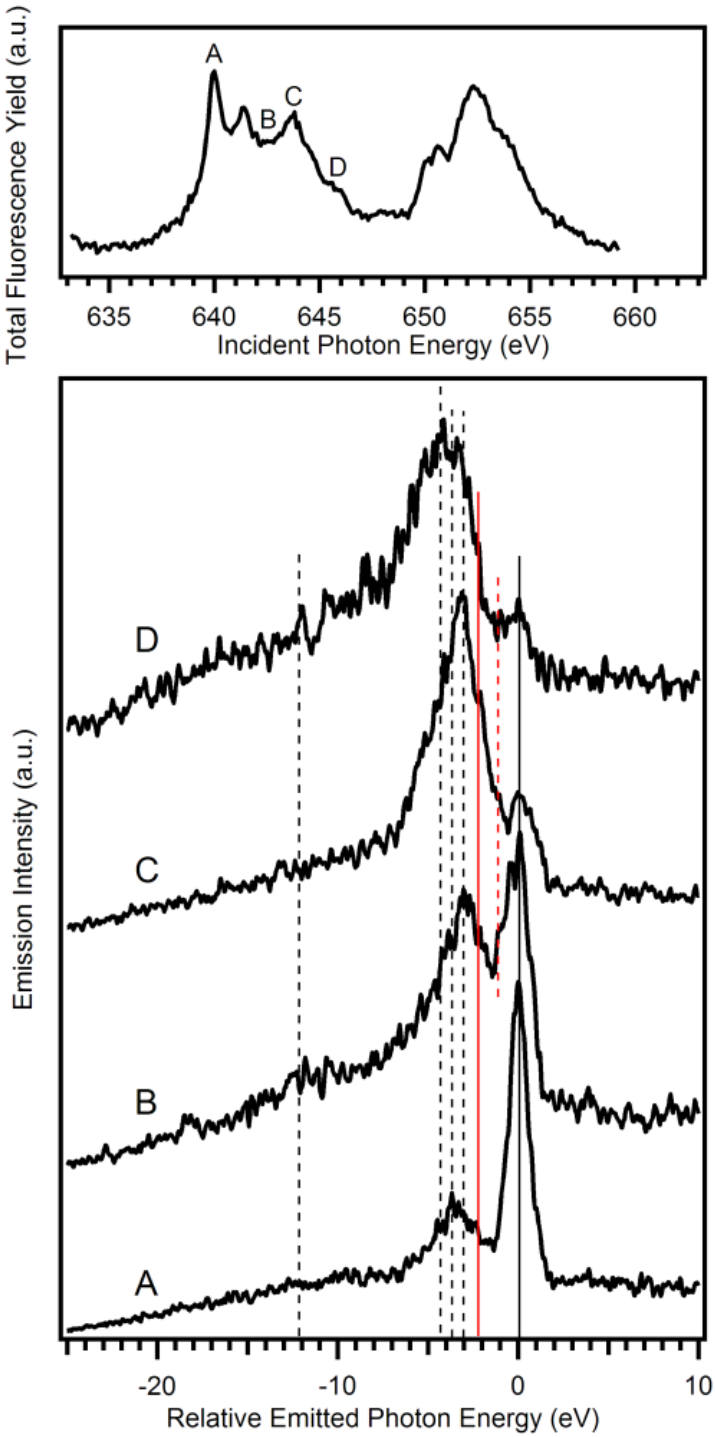

Figure 3.7. Total fluorescence yield (TFY) (top, same as Figure 3.2d) and RIXS loss spectra on Mn L-edge of doped Mn (III) in Nafion with potential applied for one hour followed by 16 hours of light illumination.

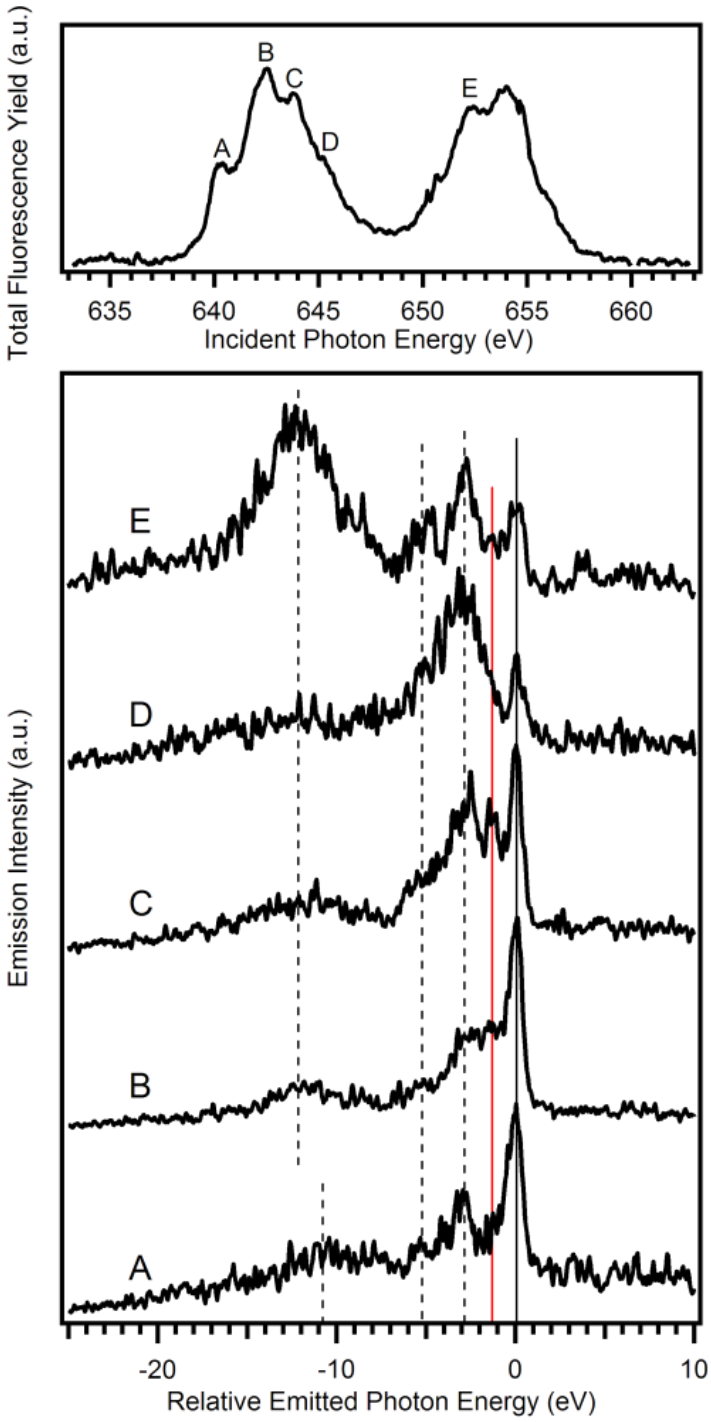

Figure 3.8. Total fluorescence yield (TFY) (top, same as Figure 3.2e) and RIXS loss spectra on Mn L-edge of doped Mn (III) in Nafion with simultaneous application of potential and light for 10 hours.

The absence of the low energy-loss features in the 0-3 eV region for the pristine Mn (III) precursor is not unique to one particular excitation energy, such as 642.5 eV chosen herein, but a general characteristic at all excitation energies within the Mn L-edge (Figure 3.4). The shift of the lowest energy-loss feature towards the elastic peak for the Mn (III) doped Nafion indicates a narrowing of the local energy gap between the HOMO and the LUMO on Mn sites. This narrower HOMO-LUMO gap remains almost constant under consecutive stimulations of electrical potential and visible light after Mn (III) doping into Nafion film, as indicated by a straight solid red line in Figure 3.3b-3.3d. The position of this solid red line is determined based on RIXS spectra at all the excitation energies for each sample (Figure 3.4-3.8). However, some weak features appear in the HOMO-LUMO gap, marked by a red dashed line in Figure 3.3, after the application of electrical potential. The emergence of these new states in the energy gap is most likely due to the formation of a new product (a manganese oxide with a birnessite structure) [43, 92, 93, 95, 111-112] under the stimulation of the electrical bias, as discussed previously. These new peaks in Figure 3.3c and 3.d, although relatively weak, actually define a much smaller HOMO-LUMO gap of around 1.1 eV from the red dashed line to the black solid line at the loss-energy zero (elastic peaks).

The local HOMO-LUMO gap on catalytic sites largely determines the ease with which electrons are transported in and out of the Mn catalytic sites, which significantly influences catalyst efficiency. However, these new peaks generally have low intensities at the excitation energy of 642.5 eV (Figure 3.3c and 3.3d), as well as at other excitation energies (Figure 3.6 and 3.7), indicating a low density of states (DOS), so that they may not significantly enhance charge flow (electrical current) near the Fermi level. Therefore, it can not be used to define a practical HOMO-LUMO gap at this stage and have marked them by a dashed red line.

When the electrical potential and visible light illumination are applied simultaneously the partial electronic density of states (PDOS) within the HOMO-LUMO gap on Mn sites is enhanced and practically defines a HOMO-LUMO gap of 1.3eV (Figure 3.3e). This loss feature at -1.3 V becomes more prominent at excitation energy of 643.9 eV (Figure 3.8c). Such a change in electronic structure near the Fermi level is expected to facilitate the electrical current flow through Mn sites; indeed, a sustainable photocurrent was observed when the Mn (III) doped Nafion films were placed under simultaneous stimulations of visible light and electrical potential [95]. Such a significant increase in PDOS was not observed when either of the stimulations (electrical potential or visible light) was applied separately. The continuous counteracting effects of electrical potential and visible light alter the Mn oxidation state and the coordinated atoms to the Mn ion, resulting in a unique electronic structure of the Mn ion revealed by RIXS analyses (Figure 3.3e).

The exact values of the local energy gap at various treatment stages extracted from Figure 3.3 are presented in Figure 3.9, indicating a clear gap reduction caused by doping in Nafion, electrical bias, and visible light illumination. The shift in the broad charge-transfer feature from -9.6 to -11.8 eV (compare Figure 3.3a with 3.3b) indicates that this type of transition requires more energy when the Mn (III) complex is doped into Nafion than in the pristine Mn (III) form. This energy shift is, again, common to all excitation energies (Figure 3.4 and 3.5). It is also not dependent on the Mn oxidation state because the energy of the charge-transfer peak does not change in going from Figure 3.3b to 3.3e, where various oxidation states exist in these spectra. The pristine Mn (III) complex has well-coordinated and relatively strong bonding ligands around the Mn ion (including bridging groups), which could lower the charge-transfer barrier between the metal center and its ligands. Once the Mn (III) complex is doped into the Nafion matrix the original molecular structure breaks down to Mn^{2+} species, and MnO_x nanoparticles in a birnessite-like structure start to form under the application of an electrical bias [11, 112]. Consequently, charge-transfer processes involving the new ligands (after doping into Nafion) and the Mn centers are expected to be different from those in the pristine Mn (III) complex (Figure 3.3). Again, the RIXS features shown in Figure 3.3 for the excitation energy of 642.5eV are also present in traces measured at other excitation energies for all investigated samples (Figure 3.5-3.8).

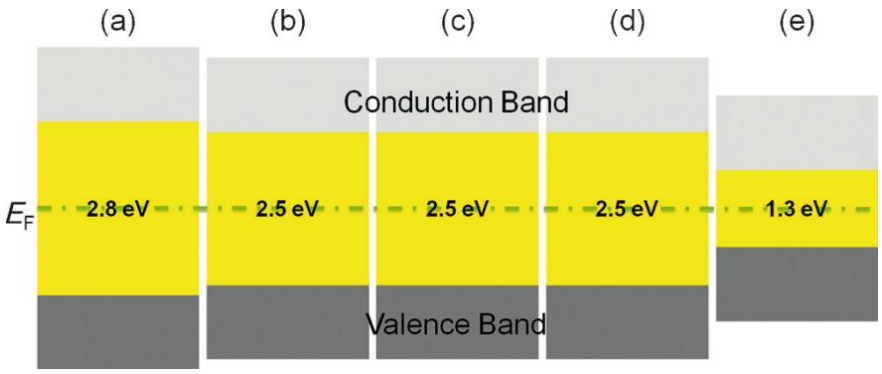

Figure 3.9. Energy diagram of local energy gaps at various treatment stages of Mn (III) complex: (a) pristine Mn (III) powder, (b) doped Mn (III) and $[Mn(OH_2)_6](ClO_4)_2$ in Nafion, (c) Mn (III) doped in Nafion with electrical potential applied for 1 h, (d) Mn (III) doped in Nafion with potential applied followed by 16 h of light illumination, and (e) Mn (III) doped in Nafion with simultaneous application of potential and light for 10 h. The light grey area indicates the conduction band, the dark grey area the valence band, and the yellow area the energy gap (label not shown). Energy levels are aligned with the Fermi level indicated by a dot-dashed green line within the energy gap.

3.3 Comparison of Mn (III) with Mn (II) and Mn (IV) Catalyst for HOMO-LUMO gap and Oxidation States

This part of thesis is taken from following publication.

Electronic Structural Insights into Efficient MnO_x Catalysts.

Munirah Khan, Edlira Suljoti, Archana Singh, Shannon A. Bonke, Tim Brandenburg, Kaan Atak, Ronny Golnak, Leone Spiccia and Emad F. Aziz .

Journal of Material Chemistry A. 2 (2014) 18199–18203. DOI: 10.1039/C4TA04185B

In earlier works encompassing K-edge X-ray absorption near edge spectroscopy (XANES), extended X-ray absorption fine structure (EXAFS), electron paramagnetic resonance (EPR), transmission electron microscopy (TEM) and electron diffraction studies it was established that disordered MnO_x nanoparticles with a layered birnessite structure were responsible for the catalytic activity [43, 95, 55]. In addition, it was found that by using different manganese precursor complexes, the size and catalytic activity of the MnO_x nanoparticles were altered [95]. Ultra-small nanoparticles (≤10 nm diameter) with the highest activity of the series were formed from a Mn (III) dimer complex that was used as a MnO_x precursor [95]. The effect of the precursors on catalytic activity has been examined, however, the effect that the Mn coordination complex has on the electronic properties of the final catalyst remains unclear. What influence do the Mn oxidation state and/or ligands in the precursor complex have on the generated MnO_x? Mn (III) complex generates MnO_x nanoparticles that were the most efficient catalysts in the series, contrasting with the MnO_x produced from the Mn (II) species which was the least active [95]. A major question that could not answer is: why are Mn (III/IV) complexes are able to generate better active catalyst than other Mn complexes?

To answer this question, a comparison of MnO_x generated from Mn (II), Mn (III) and Mn (IV) complexes is made in this section. Sample preparation was performed with the same method as described in section 3.2.1. XAS and RIXS were performed on the catalysts as described in section 3.2.2. To probe the unoccupied 3d electronic density of states (DOS), the Mn L-edge X-ray absorption (XA) spectra were recorded in total electron yield (TEY) mode, with spectra for the Mn (III) complex shown in Figure 3.10. State 1 (as doped) represents the complex doped in the Nafion film, state 2 (as biased) is after applying a 1.0 V bias (vs. Ag/AgCl) to the doped film, sufficient to form the active MnO_x catalyst, while state 3 (light shined) a result of photoreduction of the catalyst with visible light for 16 hours. During XA measurements, photon flux was minimized as a precaution against radiation damage of the catalysts from the synchrotron (Appendix A.2).

Going from state 1 to state 3 of the catalytic cycle, a pronounced intensity change of the spectral features inherent to the 3d orbital occupation and marked with letters "a–f" in Figure 3.10 is observed. The spectral features "a", "b_1– b_2" and "c", located at 640.4 eV, 642 eV, 642.8 eV and 644 eV can be associated with contributions of Mn^{2+}, Mn^{3+} and Mn^{4+} oxidation states, respectively [106,115-116]. The very high intensity of peak "a" in state 1 indicates a reduction of the Mn (III) dimer to a Mn^{2+} like state after doping into Nafion [115-116]. In order to quantify the mixed oxidation states of the catalysts, Mn L-edge XAS of several reference samples with well-known Mn oxidation states were measured: Mn_2O_3 (Mn^{3+}), synthetic birnessite (Mn^{3+} & Mn^{4+}) and MnO_2 (Mn^{4+}). The spectra obtained (Figure 3.11a) are consistent with previous reports [113]. The measured L-edge spectra of the different MnO_x catalysts were fitted by a linear combination of Mn^{2+}, Mn^{3+} and synthetic birnessite (Mn^{3+} and Mn^{4+}) spectra. The experimental and fitted spectra are shown in Figure 3.11b–d (fitting coefficients provided in Table 3.1). Thus, in the "as biased" state the MnO_x catalysts are in a mixed oxidation state that consists of 60% Mn^{3+} and 40% Mn birnessite-like for the Mn (III) catalyst; 10% Mn^{3+} and 40% Mn birnessite-like for the Mn (II) catalyst and 60% Mn^{3+} and 30% birnessite like for Mn (IV) catalyst. The presence of the 30–40% contribution from a Mn birnessite like state for all MnO_x catalysts confirm previous reports that the catalysts adopt a disordered birnessite structure under oxidative bias [43, 57].

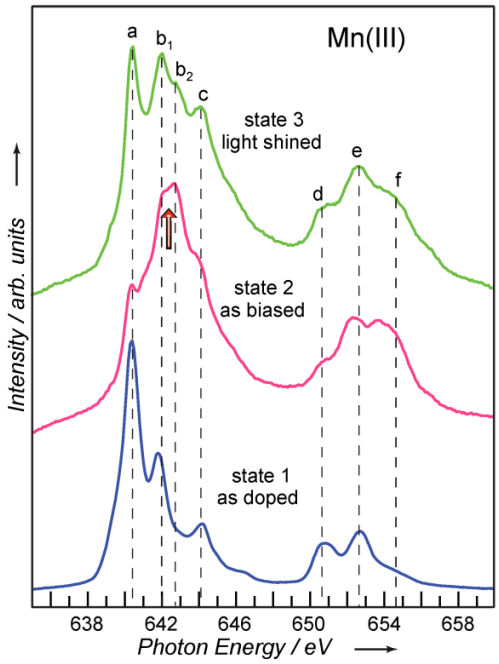

Figure 3.10. Mn $L_{2,3}$-edge XAS of the Mn (III) dimer, measured *ex situ* in TEY at different stages of the catalytic cycle. State 1 (as doped): complex doped in Nafion; state 2 (as biased): active MnO_x catalyst; state 3 (light shined): regenerated catalyst.

It is interesting to observe the higher proportion of Mn^{3+} like state in the MnO_x derived from the Mn (III) and Mn (IV) complexes (Figure 3.11b and 3.11c respectively). These are the two complexes that show the highest catalytic activity. In contrast, the least active catalyst examined, the Mn (II) precursor catalyst (Figure 3.11d) is less oxidised in the "as biased" [95]. It shows only a 10% contribution from a Mn^{3+} like state. Mn^{3+} has been recognized as an important intermediate state in Mn catalysed water splitting [13, 66, 114-118]. A greater proportion of Mn^{3+} in the structure will coincide with a larger degree of distortion in the local structure, which correlates with an improved catalytic activity [114]. Separate studies have shown increased catalytic turnover electrochemically by increasing the proportion of Mn^{3+} in MnO_x nanoparticles [116]. Regarding the MnO_x formed in Nafion TEM studies have concluded that the disordered birnessite phases generated from the Mn (III) complex have a greater number of Mn vacancies and a higher degree of layer misregistration compared to synthetic birnessite nanoparticles [57].

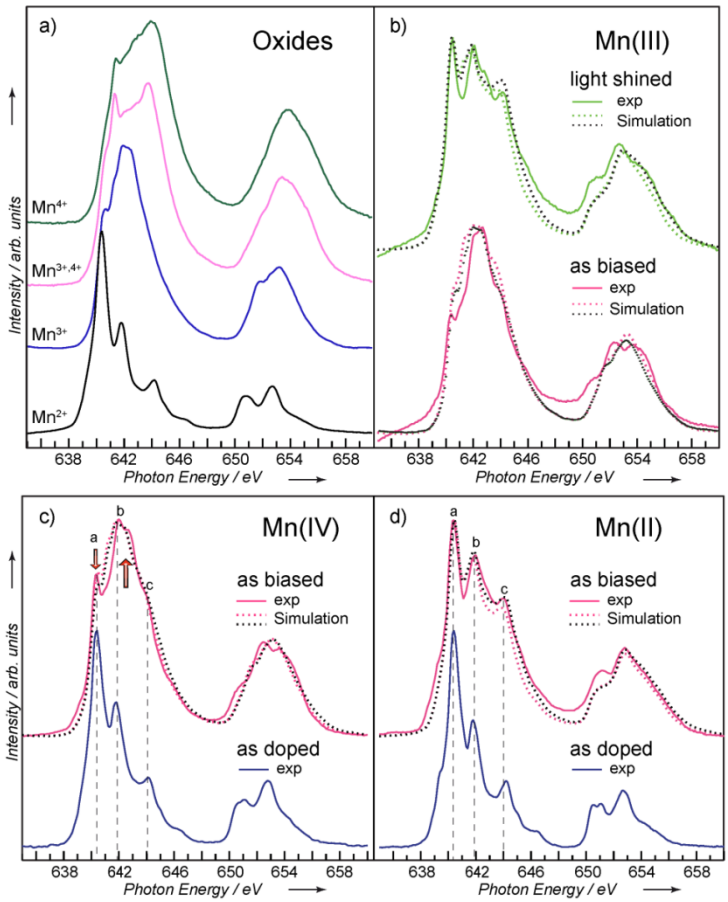

Figure 3.11. Mn $L_{2,3}$-edge XAS measured in TEY of Mn (II), Mn (III), Mn (IV) and reference Mn Oxides (a) reference Mn oxides powders; black: Mn(II) complex; blue: Mn_2O_3; pink: synthetic birnessite; green: MnO_2, and of (b–d) Mn (III), Mn (II), and Mn (IV) catalysts at different catalytic states together with simulated spectra (details are given in Table 3.1).

Herein, it is shown that Mn (III) derived MnO_x incorporates a higher content of Mn^{3+} like states. Previous catalytic studies have shown that MnO_x derived from the Mn (III) complex is more active towards water oxidation than those from the Mn (II) or Mn (IV) complexes [95]. Correlating the results from these studies indicates that the higher catalytic activity shown by these Mn (III) derived nanoparticles is likely due to the higher proportion of Mn^{3+} like states. Such a conclusion would be aligned with previous studies in the literature considering the findings linking Mn^{3+} with improved catalysis of water oxidation [114-118]. Furthermore, examination of the nitrogen K-edge XAS for the Mn (III) in Figure 3.12 revealed that some of the Me_3TACN ligands remain coordinated to Mn ions after doping into Nafion. The presence of the ligands may stabilize the Mn^{3+} like states allowing a higher proportion of Mn^{3+} like states [116].

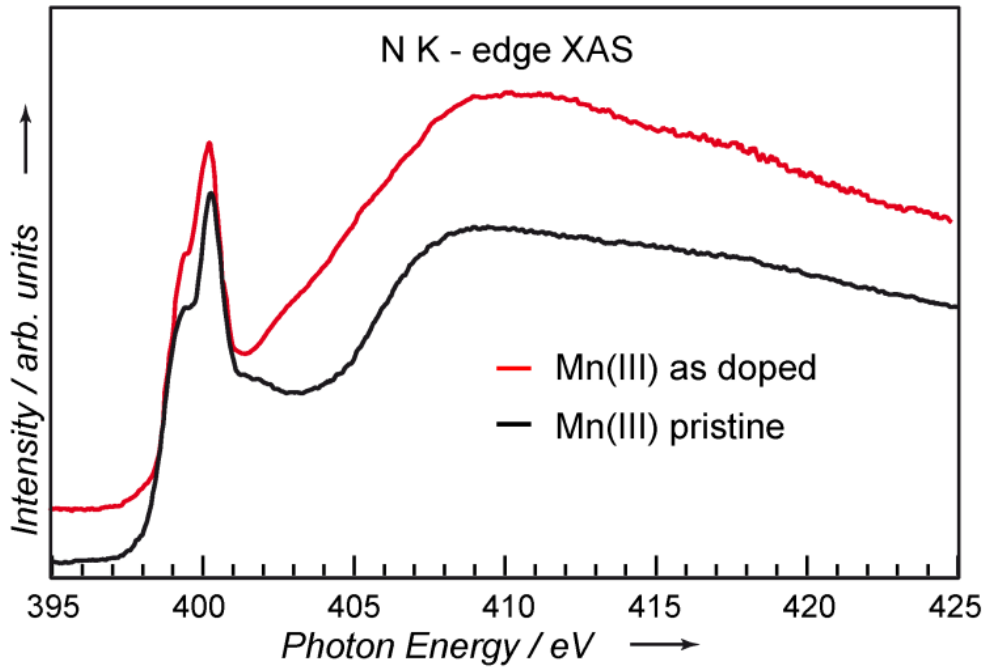

Figure 3.12. Nitrogen K-edge XAS spectra of Mn (III) complex. Black: the pristine complex dissolved in dichloromethane, State 0; red: the complex as doped into Nafion, State 1. The exact energetic location and resemblance of the near-edge double peak indicates that some of the Mn-N bonds are not broken, i.e., some TACN ligands remain coordinated to Mn inside the Nafion. The small intensity changes at Rydberg and shape resonance area (located at higher energies) manifest a change in the chemical local environment, most probably induced by the anionic sulfonate group of the Nafion matrix.

Applying the same fitting procedure to the XA spectrum of the MnO_x catalyst in state 3 (Figure 3.11b), it was found find that the catalyst is partly photo-reduced. Its mixed oxidation state consists of 45% Mn^{2+}, 15% Mn^{3+}, and 40% Mn birnessite-like state contributions. It is important to note that its birnessite-type phase contribution remains unchanged compared to the "as biased" state, even though photo-reduction converts almost 50% of the charge from the Mn^{3+} to Mn^{2+} oxidation state. This suggests that the distorted MnO_x catalyst derived from the Mn (III) complex is stable and remains as the active phase in state 2 and state 3 of the catalytic cycle. Although the greater proportion of Mn^{3+} like states correlates with catalytic activity, the reason for these activity increases remains unclear. To further reveal the role of Mn^{3+} in catalytic reaction of Mn RIXS experiments are performed as following.

Catalyst	**Fitting coefficients with: Mn^{2+} +Mn^{3+} + Birnessite**	**Fitting coefficient with: Mn^{2+} +Mn^{3+} + Mn^{4+}**
Mn (III) as biased	60% Mn^{3+} + 40% Birnessite	5% Mn^{2+} + 70% Mn^{3+} + 25% Mn^{4+}
Mn (III) light shined	45% Mn^{2+} + 15% Mn^{3+} + 40% Birnessite	55% Mn^{2+} + 10% Mn^{3+} + 40% Mn^{4+}
Mn (II) as biased	60% Mn^{2+} + 10% Mn^{3+} + 30% Birnessite	60% Mn^{2+} + 10% Mn^{3+} + 30% Mn^{4+}
Mn (IV) as biased	10% Mn^{2+} + 60% Mn^{3+} + 30% Birnessite	10% Mn^{2+} + 60% Mn^{3+} + 30% Mn^{4+}

Table 3.1. Fitting of XAS experimental spectra of MnO_x catalysts with a linear combination of oxide powders experimental spectra accounting for Mn^{2+}, Mn^{3+}, Mn^{4+}, and birnessite states like contributions.

Figure 3.13 represents RIXS comparison on the MnO_x catalysts generated from Mn (III) (most efficient catalyst) and Mn (II) (least efficient); that is, in state 2 (as biased). The spectra are presented as photon loss features in Figure 3.13. The peak located at 0 eV energy loss is due to filling of the 2p core hole by the excited electron (photon in = photon out), the peaks located at higher energy losses, up to 6 eV, are due to filling of the 2p core hole by an electron from the occupied 3d valence states (photon out < photon in) while the peaks located above 8 eV are due to charge transfer transitions [105,119]. Being fully dipole-allowed, RIXS can probe the intensity and energetic position of the occupied 3d DOS relative to the empty 3d states. In addition, the lowest energetic d–d transition can be a measure of the band-gap between the 3d valence band maximum (VBM) and the 3d conduction band minimum (CBM). Exciting the 2p electron to feature "a" as in Figure 3.10 corresponding to Mn^{2+} like state located at 640.4 eV, one can observe similar occupied 3d DOS for both Mn (III) and Mn (II) systems and a 3d band gap of 3.6 eV could be estimated. Excitation of the 2p electron at state "b1" (located at 642 eV) results in a shift of the 3d occupied DOS towards lower photon energy losses in Figure 3.13. This shift occurs in both the Mn (III) and Mn (II) derived catalysts (state 2, as biased), but is more pronounced in the case of Mn (III) derived MnO_x. Exciting the 2p electron at spectral feature "b2" (Figure 3.13), results in the greatest shift in the 3d DOS, giving rise to a 3d CBM–VBM band gap of 2.5 eV for Mn (III) and 3 eV for Mn (II). In addition, the RIXS spectra excited at XA features "b1" and "b2" show the presence of a higher intensity charge transfer peak located between 8 and 12 eV energy losses for Mn (III) derived MnO_x in comparison to the Mn (II) system.

These results indicate that the "b1" and "b2" absorption features are the result of mixed unoccupied states of Mn 3d and ligand 2p states. They are also indicative of the presence of itinerant electrons. Charge-transfer band is missing in both Mn (III) and Mn (II) derived oxides, while they both show the same band gap of 3 eV. It is interesting to note that excitation at peak "e" at the L_2-edge, which is the broadened replica of "b1–b2" feature at the L_3-edge, manifests the same behavior. This provides an explanation for the much higher photocurrents measured for Mn (III) derived MnO_x catalysts. When exciting at 644 eV, which would correspond to a Mn^{4+} like state, the energetic shift of the 3d Mn valence states is toward lower energies and a very strong emission extended up to 20 eV energy losses. This is due to a charge transfer transition mixed with a fluorescence contribution. The intensity of this peak for the Mn (III) derived oxide is much greater than that from Mn (II) in state 2 of the catalytic cycle (Figure 3.10). This can again be taken to indicate the itinerant electron and the presence of 2p ligands DOS in the vicinity of manganese metal centres. Bearing in mind that being lower in average oxidation is due to higher contribution from "b1– b2" features which correspond to a Mn^{3+} like state, the correlation between the higher Mn^{3+} quantity and previously quantified catalytic activity is supported.

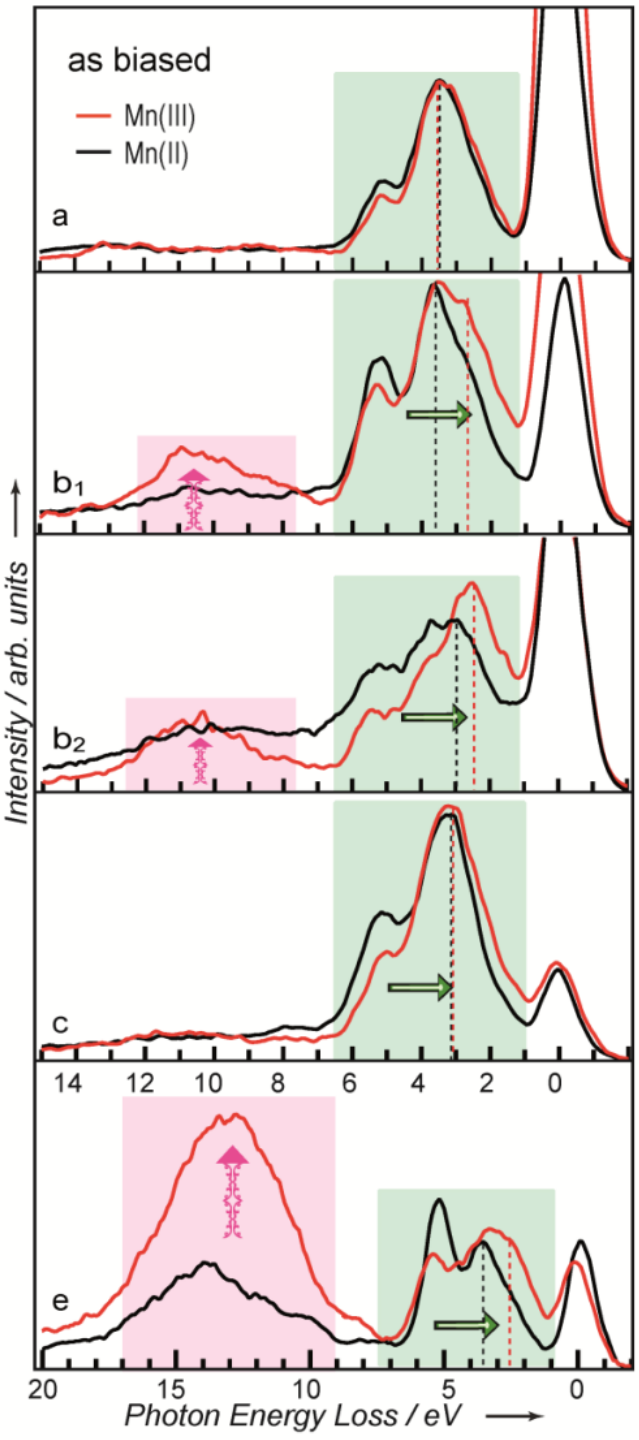

Figure 3.13. Experimental RIXS spectra at the Mn $L_{2,3}$-edge of Mn (III) and Mn (II) catalysts in state 2 (as biased) of the catalytic cycle. Red: Mn (III) and black: Mn (II) RIXS spectra are measured upon excitation at the spectral features marked a–e in the XAS spectra shown in Figure 3.3. Charge transfer transitions are highlighted pink and d–d transitions are highlighted green.

Figure 3.14 explains RIXS spectra measured at the Mn L_3-edge of Mn (III) catalysts and synthetic birnessite. Four excitation energies for each RIXS spectrum are shown in Figure 3.14. It explains that energy loss features of birnessite are expanded at higher energies than in Mn (III) State 2. The d-d features of synthetic birnessite are more closely spaced to elastic line than Mn (III). According to the previous study reported by Ghiringhelli et al this result shows that the average oxidation state of the electro-oxidized Mn (III) cluster is lower than the synthetic birnessite [108].

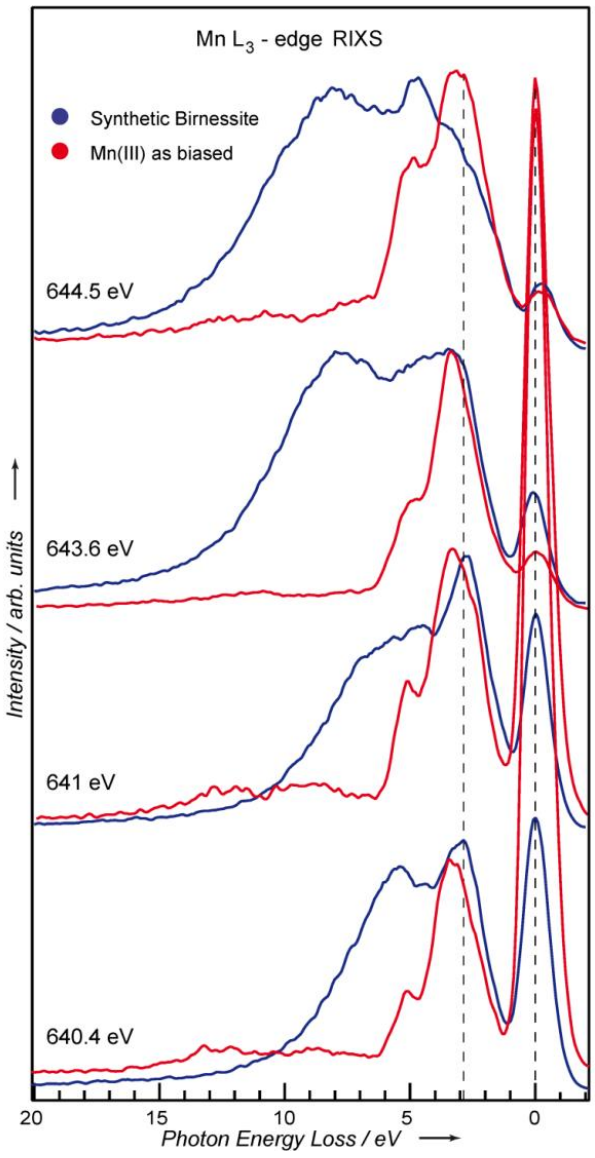

Figure 3.14. Experimental RIXS spectra measured at the Mn $L_{2,3}$-edge of Mn (III) catalysts and synthetic birnessite. Excitation energies for each RIXS spectrum are given in the Figure 3.10. Energy loss features of birnessite are expanded at higher energies than in Mn (III) State 2.

3.4 Theoretical Calculations

This part of thesis is taken from following publication.

Unraveling Electronic Structure of Photocatalytic Manganese Complexes via Theoretical Multi-Reference X-Ray Spectroscopy

Sergey I. Bokarev, **Munirah Khan**, Mahmoud Abdel-Latif, Jie Xiao, Leone Spiccia, Rifaat Hilale, Saadullah G. Azize, Emad F. Aziz, and Oliver Kühn.

The Journal of Physical Chemistry C. DOI: 10.1021/acs.jpcc.5b05169

Interpretation of complex experimental spectra or spectra with unresolved bands is a non-trivial task and insights from theoretical simulations are mandatory. Recently, Professor Oliver Kühn and his group has shown the multi-reference approach to calculate X-ray spectra utilizing the restricted active space self-consistent field (RASSCF) technique together with the state interaction method (RASSI) for spin-orbit coupling [120]. These techniques were proven to be quite effective in unraveling the nature of different transitions in both XAS and RIXS [121-127]. They are particularly suited for the investigation of transition metal complexes as these are multi-reference character even in the ground electronic state and the dipole selection rules allow keeping the active spaces quite compact, since only MOs with substantial d-character need to be considered. According to theoretical analysis of Professor Kühn, the oxidation state of the central ion has a strong impact on the XAS and especially RIXS spectra what allows using them as a sensitive probe of the electronic structure [122-127].This makes the combination of experimental and theoretical X-ray spectroscopies a powerful tool for studying chemical transformations of transition metal coordination compounds in course of catalytic processes [123].

This section includes theoretical calculations performed by Professor Oliver Kühn and his group to provide theoretical explanation of experimental sepctra discussed in previous section. The interpretation of theoretical calculations was performed by combined efforts of author and his group. From the viewpoint of computational methodology, the simplest 3p5d active space already well reproduces the shape of both XAS and RIXS similar to other aqueous transition metal complexes [122-127]. However, the deeper σ3d orbitals need to be taken into account to reveal the charge transfer transitions. The application of RASPT2 leads to over-stabilization of the ground state what slightly deteriorates the agreement with experiment. In addition, RASPT2 encounters severe intruder states problems when σ3d orbitals are included into the active space and cannot be recommended in this case.

Special focus was put on the quantification of spin-orbit coupling in the core-excited states, being stronger than for the valence ones. The strength of mixing between states of different multiplicities increases in series Mn^{2+}, Mn^{3+}, and Mn^{4+} as well as from lower to higher energies across the spectrum. Because of stronger mixing core-excited states mediate formally spin-forbidden transitions between different valence spin manifolds. Thus the description of RIXS spectra in terms of HOMO-LUMO gaps based on purely experimental results seems to be simplistic since spin-mixing effects are not included in this picture. Figure 3.15 shows the experimental absorption spectra recorded in total electron yield (TEY) mode for Mn (II) and Mn (III) precursors after doping into Nafion matrix (denoted as doped) and application of a voltage (denoted as biased).

The spectrum of the doped Mn (III) compound is not shown because it very closely resembles that of the Mn (II) doped sample [96]. The spectra are aligned according to the energies of corresponding transitions. In the lower part of Figure 3.15, the calculated XAS spectra for different complexes using the RASSCF and RASPT2 methods for different active spaces are presented. The fact that in experiment one has mixture of different forms complicates the comparison with theoretical results. However, it could be clearly seen from Figure 3.15, that XAS of doped Mn (II) and Mn (III) samples is dominated by the reduced Mn^{2+} species, whereas Mn (II) and Mn (III) after applying bias could be attributed to predominant Mn^{3+} and Mn^{4+} species, respectively, determined by the linear fitting in the previous study [96]. All spectra consist of two band systems L_3 and L_2 (3/2 and 1/2 total angular momentum of the core hole), with the L_3/L_2 energy splitting corresponding to the core hole spin-orbit coupling. As illustrated in Figure 3.16 and discussed below, core-excited states with different spin, S-1, S, S+1, strongly mix; here S denotes the spin of the ground state. The unambiguous analysis of the character of both valence and core-excited states is further hindered by strong multi-configurational nature of the states. Therefore, below a simplified picture based on the occupation numbers of natural orbitals is presented. Due to the multi-configurational character, these occupation numbers are in general non integer and the core electron can be distributed over several MOs.

The complexes with different oxidation states of the central Mn ion show distinct differences in their absorption spectra. In $[Mn^{2+}(H_2O)_6]^{2+}$ (group IIa in Figure 3.15), the low energy shoulder (*a*) of the L_3 band consist of weak almost purely spin-allowed S→S transitions predominantly of $2p\rightarrow3d(t_{2g})$ character. The main band (*b*) besides S→S has a notable admixture of S→S-1 character as seen in Figure 3.16. The nature of the electronic transitions is of mixed $2p\rightarrow3d(t_{2g})$ and $2p\rightarrow3d(e_g)$ type, with the latter having larger intensity. The next two peaks denoted as *c* in Figure 3.15 are mostly spin-forbidden S→S-1 transitions of mixed t_{2g}/e_g character borrowing some intensity through mixing with the S states of the main spin series. The corresponding groups of states (*a*-*e*) are also shown in Figure 3.16.

The L_2 band has similar assignment although spin mixing is even stronger. Coordination of two Nafion-like ligands (group IIb in Figure 3.15) leads only to very minor changes if compared to $[Mn^{2+}(H_2O)_6]^{2+}$. The low-energy shoulder (*d*) of the L_3 edge in the $[Mn^{3+}(H_2O)_6]^{3+}$ spectrum (group IIIa in Figure 3.15) is due to S→S/S+1 excitations, mostly to e_g orbitals. The corresponding transitions at the L_2 edge gain more intensity due to stronger spin-orbit coupling giving rise to more pronounced features in the 647-650 eV range. Starting from the main peak (*b*) the S/S-1 state mixing plays a role and for the post-peaks (*c*) it has already predominant spin forbidden character. The electronic character of the most intense transitions across the whole Mn (II) spectrum corresponds to $2p \rightarrow 3d(e_g)$ excitations. Remarkably, already at the main band the shake-up effects are prominent, i.e. the $2p \rightarrow 3d(e_g)$ excitations are accompanied by $3d(t_{2g}) \rightarrow 3d(e_g)$ transitions.

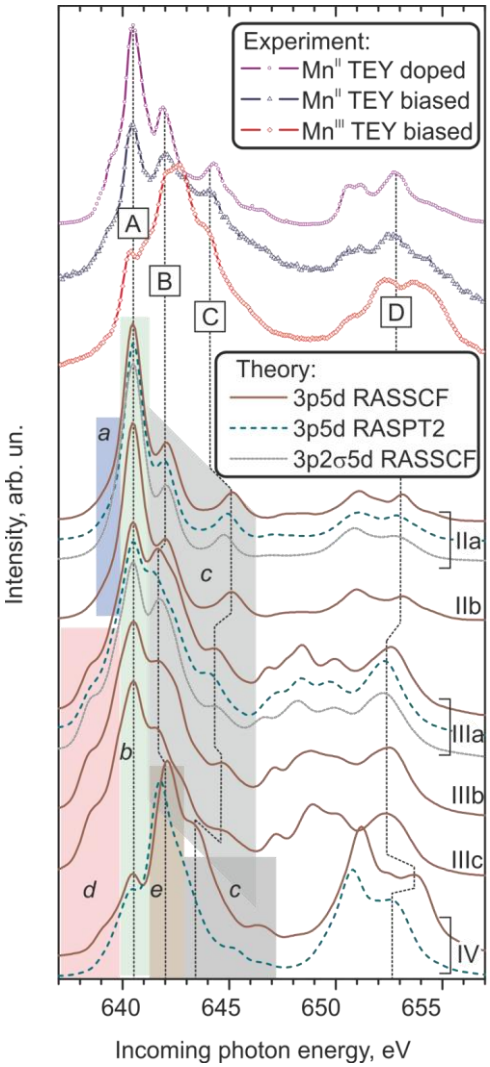

Figure 3.15. Experimental and calculated XAS spectra with RASSCF and RASPT2 methods and different active spaces of Mn complexes: group IIa is $[Mn^{3+}(H_2O)_6]^{2+}$; group IIb is $[Mn^{2+}(H_2O)_4N_2]^{0}$; group IIIa is $[Mn^{3+}(H_2O)_6]^{3+}$; IIIb is $[Mn^{3+}(H_2O)_4N_2]^{+}$; IIIc is $[Mn^{3+}L(AcO)N_2]^{0}$ and group IV is $[Mn^{3+}L(OMe)_3]^{+}$.

This effect becomes more pronounced for the *c* bands (especially for the second one at 645 eV) and the last peak of L_2 band (653 eV). These shake-up bands have lower intensities than one-electron transitions, but their density is large giving rise to notable features. Coordination of $CF_3SO_3^-$ ligands (spectrum IIIb in Figure 3.15) has a bit more pronounced influence on the XAS spectra of Mn (III) complex than for Mn (II) one. However, the assignment for both $[Mn^{3+}(H_2O)_4N_2]^+$ and $[Mn^{3+}L(AcO)N_2]^0$ (spectrum IIIc) stays the same as for $[Mn^{3+}(H_2O)_6]^{3+}$. The Mn (IV) spectrum has an assignment similar to Mn (III). As peculiarities one can consider the prevailing $2p\rightarrow3d(t_{2g})$ character of *d* shoulder and notable contributions from the sextet states (S+1) for *b*, *d*, and *e* features (Figure 3.15). Shake up effects are even more pronounced in this case.

The experimental RIXS spectra for doped and biased Mn (II) and Mn (III) precursors are plotted in Figure 3.17 together with the results of theoretical simulations. The experimental excitation energies correspond to the bands denoted as A (640.4 eV), B (642.0 eV), C (644.0 eV), and D (652.6 eV) in Figure 3.15. These energies vary slightly for different complexes and methods in theoretical simulations. In general, the shapes of the theoretical RIXS spectra are in good agreement with the experiments.

In Mn (II) systems, both t_{2g} and e_g orbitals are equally populated in the ground sextet state. Additionally, all final valence excited states except for the ground one belong to the quartet spin manifold within the 3p5d active space. This means that apart from the elastic peak all other features for this model correspond to the change of the multiplicity. The lowest excited valence state of Mn (II) lies about 2.8 eV above the ground state. In total for the 3p5d active space, valence states cover range up to 6.5 eV (or -6.5 eV loss energies). The inelastic transitions in Mn (II) RIXS can be divided into three groups. They start from the pairing of electrons from e_g to t_{2g} orbitals, which corresponds to the shoulder at -2.7 − -3.2 eV loss energies. The main peak at -4.1 – -4.3 eV and less intense feature at about -6.3 eV are assigned to reverse electron redistribution $t_{2g}\rightarrow e_g$.

Due to complex multi-configurational nature of the wave function the loss/excess of electrons is usually almost equally redistributed within t_{2g} or e_g orbitals. The third group, present only for the 3p2σ5d active space, corresponds to relaxation of electrons from σ3d (e_g) orbitals filling the core hole. These transitions have substantial charge transfer character, because the core-hole is strongly localized on the Mn atom and σ3d orbitals have predominant ligand localized character. The coordination of Nafion (spectrum IIb) has very minor effect on the RIXS spectrum similar to XAS.

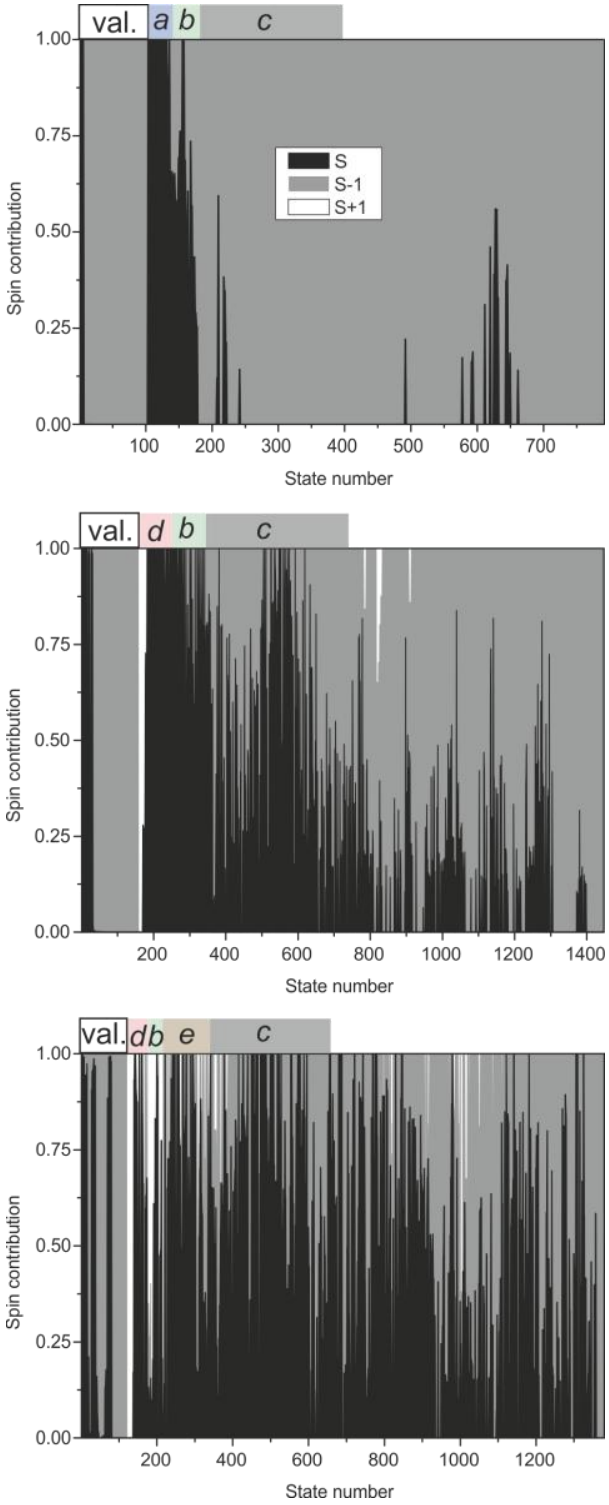

Figure 3.16. Contributions of states with ΔS=0,±1 to the spin-orbit coupled wave functions for $[Mn^{2+}(H_2O)_6]^{2+}$ (top), $[Mn^{3+}(H_2O)_6]^{3+}$ (middle), and $[Mn^{4+}L(OMe)_3]^{+}$ (bottom) ions obtained with the RASSCF method and the 3p5d active space. The labels on top of each panel correspond to bands in Figure 3.15.

Mn (III) RIXS demonstrates a more specific behavior due to the appearance of the valence hole in the e_g orbitals. Here, the first excited valence state occurs at 0.7 eV having $e_g \rightarrow e_g$ nature. The gap between ground and first excited states is smaller than the combined lifetime and inhomogeneous broadening, that is why, the elastic peak is not resolved from the inelastic bands. In contrast to Mn (II), in Mn (III) the quintet states are present in the valence manifold, however, the triplet states still dominate and most inelastic features correspond to formally spin-forbidden S→S-1 transitions. The next feature at about -1.6 eV is attributed to a number of intertwined $t_{2g} \rightarrow e_g$ and $e_g \rightarrow t_{2g}$ transitions having nearly the same energy and intensity. The feature at -2.9 eV corresponds to redistributing electrons within t_{2g} or e_g orbitals that is $t_{2g} \rightarrow t_{2g}$ and $e_g \rightarrow e_g$ excitations. The range -3.9 – -8.6 eV can be assigned to $t_{2g} \rightarrow e_g$ transitions possessing notable amount of double electron shake up character. In contrast to Mn (III), $[Mn^{3+}(H_2O)_4N_2]^+$ (and similarly $[Mn^{3+}L(AcO)N_2]^0$) demonstrates notable increase of intensity at about -2 eV, this can be caused by stronger covalent interactions for the higher charged Mn (III).

The nature of the electronic transitions in the case of Mn (IV) complex is quite homogeneous. All transitions with notable intensity representing inelastic features are of $t_{2g} \rightarrow e_g$ character; some of them possess considerable double excitation character. Mainly these are transitions in the ranges -3.0 – -3.9 eV and below -5.0 eV. Noteworthy, inelastic features are of both S→S and S→S-1 character, with the amount of S→S intense transitions decreasing from A to D excitation lines, which is in accord with increase of spin-mixing (Figure 3.16).

The CT bands (-15 - 25 eV) consisting of $\sigma 3d(e_g) \rightarrow 3d(t_{2g})$ and $\sigma 3d(e_g) \rightarrow \sigma^* 3d(e_g)$ transitions tend to have 7-10 eV lower loss energies than in experiment, showing notably more bound σ3d orbitals. Probably the inclusion of dynamic correlation could improve the agreement with experiments here. Note, for both $[Mn^{2+}(H_2O)_6]^{2+}$ and $[Mn^{3+}(H_2O)_6]^{3+}$ with 3p2σ(1hole)5d active space the intensities of CT bands are quite low for all excitation energies. Only if two holes are allowed for σ-orbitals, the intensity of CT becomes large for D excitation similar to experiments. This effect cannot be attributed solely to the contribution of two-electron transitions; obviously the correlation introduced by allowing two holes is also important.

Comparing RIXS spectra for systems with different oxidation states of manganese ions shows that Mn (III) differs most prominently from Mn (II) and Mn (IV). It shows very small gap between ground and first excited state of 0.7 eV, while both even oxidation states have 2.8 and 1.8 eV, respectively. Since at experimental conditions one has a mixture of different Mn ions, the contribution from Mn^{3+} leads to the appearance of inelastic features at lower energies as was observed in experiments [96] and shown in Figure 3.17. However, the signal is dominated by the Mn^{2+} contribution.

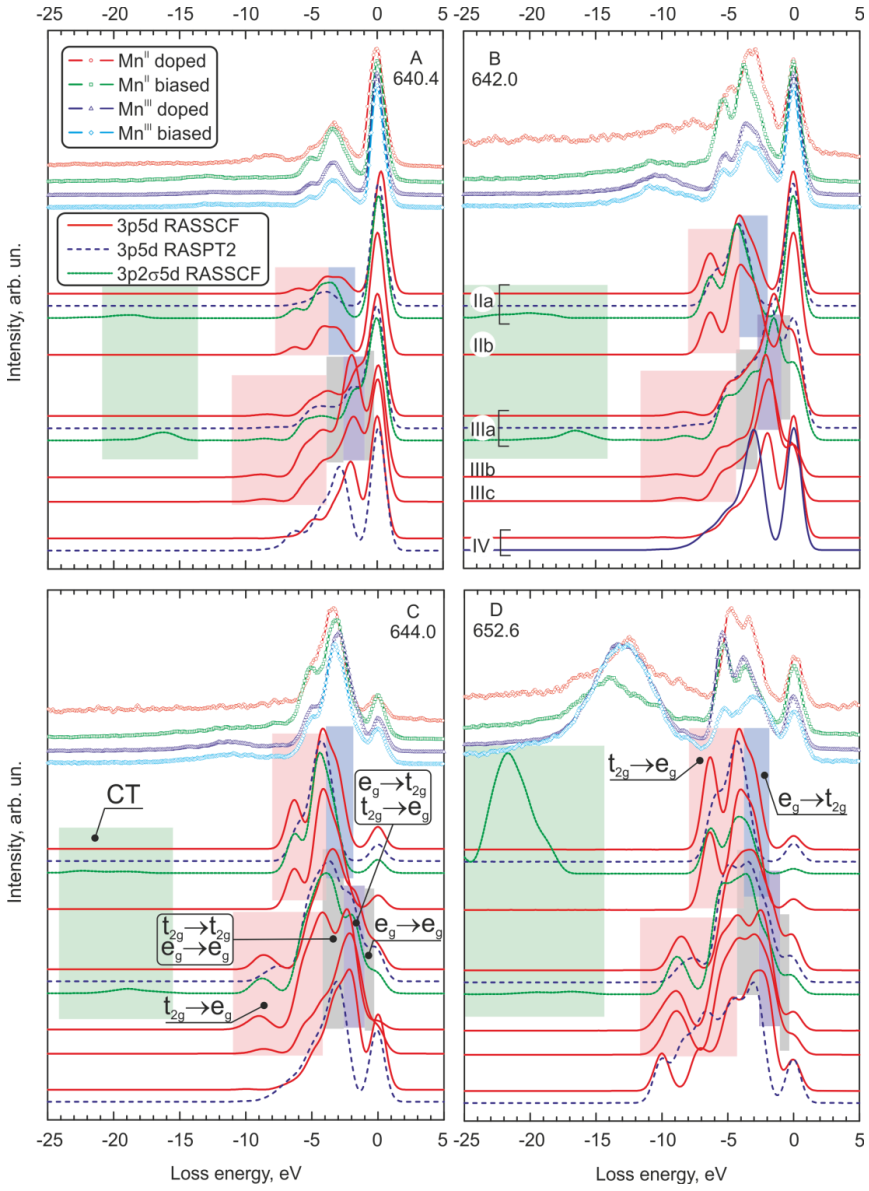

Figure 3.17. RIXS spectra of different Mn complexes at excitation energies of 640.4 (A), 642.0 (B), 644.0 (C), and 652.6 (D) eV as obtained from experiment and different computational approaches. Spectra IIa-IV are the same as in Figure 3.15.

The spin-orbit mixing is illustrated in Figure 3.16 providing the collective contributions of states of different multiplicities to the wave function of the spin-orbit coupled states in the LS coupling scheme. The labels on top of each panel correspond to bands in Figure 3.15. The strength of mixing systematically increases with the state energy and along with the increase of the charge of central ion, being the largest for Mn (IV). For the valence manifold, states from main spin progression S usually have the lowest energies; S-1 states have intermediate and S+1 state have the highest energies. Interestingly, in the case of Mn (III) and Mn (IV) for the core manifold, the S+1 state (septets and sextets, respectively) occur right after the core-excitation threshold. Thus the order of spin-states changes to S+1<S<S-1 (Figure 3.16). The same reverse order for Mn (III) and Mn (IV) is obtained accounting for dynamic correlation via the PT2 correction on the top of RASSCF. This evidences that the stability of the spin-states is affected by the presence of the core-hole. In addition, although most of low-energy S+1 states do not contribute notably to the spectrum, a quite notable fraction of them is mixed with the S states and show up as low energy shoulders of the L_3 and L_2 bands (denoted as *d* in Figure 3.15).

In Mn (II) complexes, all final valence excited states are quartets (within the 3p5d active space) evidencing that inelastic RIXS process corresponds to the change of the multiplicity: starting from the pure sextet ground state through spin-mixed intermediate core-excited states to the final pure quartet states. Because of the stronger spin-orbit coupling of the core-hole than for the valence one, core-excited states are much stronger spin-mixed (Figure 3.16). That is why inelastic RIXS process can be described as sextet→mixed→quartet transitions, which are spin-forbidden for first order valence excitation process. Hence, core-excited states mediate the coupling of sextets and quartets. In general, for excitation at the A band in Figure 3.15, the elastic peak is much more prominent than the inelastic features. Moving further to B, both have comparable intensity and for C and D elastic peak is notably weaker than the inelastic ones. This fact could be explained by the tendency of an increase of quartet character in the core states when moving in the direction of the increase of energy across the spectrum. Thus, the more quartet character is present the more intense are inelastic transitions to the final quartet manifold and the less intense are those back to the sextet ground state. This situation does not change if more sextet valence states are included in the calculation with the 3p2σ5d active space (dotted green line, group IIa, Figure 3.17) since the number of quartet states is much larger. With Mn (II) systems being an extreme case, Mn (III) and Mn (IV) RIXS spectra show basically similar behavior and are dominated by spin-forbidden transitions.

Concerning the effect of the computational method, the PT2 correction overstabilizes the ground state if compared to other valence and core-excited states. This is reflected both in the XAS and RIXS. For XAS this corresponds to a shift of the spectrum as a whole to higher energies. The offset for the comparison with experiments substantially increases upon inclusion of the PT2 correction.

The same effect corresponds to the shift of inelastic RIXS features to more negative loss energies (Figure 3.17), e.g. for Mn (II) this shift is 0.6 eV. The structure of the inelastic bands stays almost intact upon such shift, again evidencing that it is mostly due to the effect on the ground state. In a series Mn (II) - Mn (III) - Mn (IV) the effect of PT2 increases, which can be explained by stronger covalent interaction of highly charged ions with ligands and thus increasing importance of inclusion of dynamic correlation.

3.5 Conclusions

In summary, previous work on Mn water splitting catalysts is complemented by performing X-ray absorption and resonant inelastic X-ray scattering experiments at the manganese L-edge. These techniques were applied under *ex situ* conditions at different stages of the catalytic cycle to gain additional electronic structural insights into the MnO_x catalysts. It has been demonstrated that the XAS and RIXS techniques can be used in combination to probe the changes in electronic structure of a manganese catalyst for water oxidation involving the application of electrical potential and visible light illumination. The electronic structure of Mn 3d orbitals near Fermi level is well-resolved by these two types of measurements, especially RIXS that reveals the detailed Mn 3d structure in a bulk material (Nafion). The Mn 3d orbitals and its oxidation state are altered by Nafion sulfonic group, electrical potential and light illumination. The local HOMO-LUMO gap on Mn sites, an important factor influencing the catalytic efficiency, becomes reduced when Mn (III) complex is doped into Nafion and further reduced when the electronic potential and light illumination are simultaneously applied to the Mn (III) doped Nafion films.

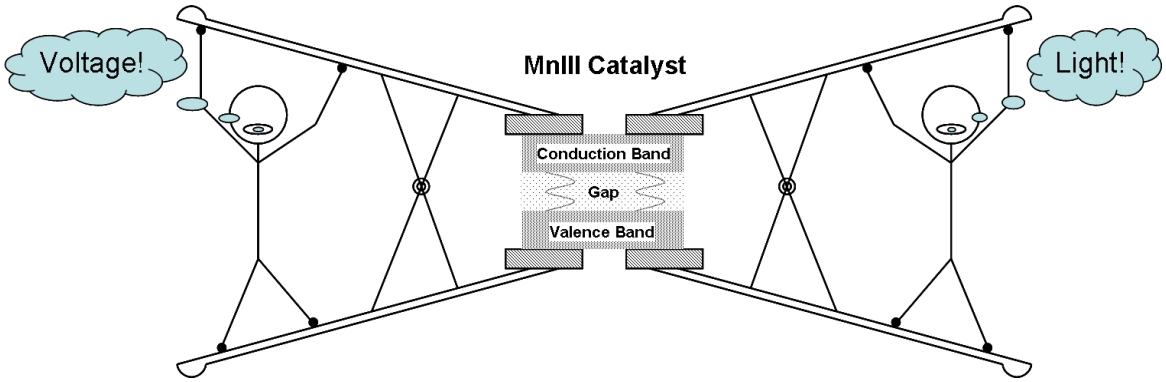

Figure 3.18. Schematic Figure showing the simultaneous effect of light and potential on local d-d gap of MnOx catalyst

The narrowing of the local HOMO-LUMO gap on the catalytic sites enhancing **t**he catalytic activity is exactly revealed by RIXS technique. This elucidation of the local electronic structure on Mn sites cannot be made possible without the advanced RIXS measurement. There is no steady catalytic activity occurring when two stimulations (electrical potential and light illumination) are applied separately and the local HOMO-LUMO gap remains relatively large. Only when both electrical potential and visible light applied simultaneously, the local HOMO-LUMO gap significantly reduces to 1.3 eV and the continuous catalytic reaction and large photocurrent are observed.

In the second part, it is shown that whilst each of the examined precursor complexes forms nanoparticles with a disordered birnessite phase, they show distinct differences in their electronic structure. Mn centres in the MnO_x nanoparticles are highly oxidised and that the ratio of Mn oxidation states varies (Mn^{2+}, Mn^{3+}, and Mn^{4+}), with the most active catalyst showing a higher proportion of Mn^{3+} over the $Mn^{2+/4+}$ like states. Furthermore, the RIXS experiments indicated that Mn^{3+} like states have the lowest local HOMO–LUMO gap (d–d transition energy of 2.5 eV) of the Mn sites present. The Mn^{3+} like states also display the strongest intensity of charge transfer emission band compared to the $Mn^{2+/4+}$ like states. These facts point to the presence of itinerant electrons.

The results of RASSCF/RASSI calculations of different manganese compounds demonstrate fairly good agreement with experiment for both XAS and RIXS what allows to unequivocally assigning spectral features. According to theoretical analysis, the oxidation state of the central Mn ion has strong impact on the XAS and especially RIXS spectra that allows using them as a sensitive probe. It is shown that the gap between the ground and first valence excited state varies strongly for different oxidation states, being 2.8, 0.7, and 1.8 eV for Mn (II), Mn (III), and Mn (IV), respectively. That is why inelastic RIXS features of Mn (III) are close to the elastic band and was not resolved from it. This supports the interpretation made in experimental works. Interestingly, the S+1 core-excited states show up in Mn^{3+} and Mn^{4+} right after the core excitation threshold, which is not the case for valence states. Mn^{2+} shows mainly two groups of transitions separated in energy, while Mn^{3+} has several groups corresponding to different redistributions of electrons both between t_{2g} and e_g MOs and within t_{2g} or e_g groups. All transitions in Mn^{4+} are of $t_{2g} \rightarrow e_g$ character.

Chapter 4

On the Origin of the Improvement of Electrodeposited MnO_x Films in Water Oxidation Catalysis Induced by Heat Treatment and Various Electrolyte pH

4.1 Introduction

Manganese oxides (MnO_x) have been widely recognized as promising catalysts for water oxidation [43, 61]. Various approaches have been used to synthesize highly active MnO_x and various treatments were applied to the MnO_x to improve the catalytic performance [128-129]. Despite their relatively simple chemical compositions, many factors have been shown to affect the catalytic activity, [130-132] and the mechanisms by which MnO_x catalyzes water oxidation are rather complicated, [115, 130-131] and poorly understood at a molecular level. This lack of knowledge has triggered extensive studies. Two factors that are highly related to the electronic structure of catalysts, and intrinsic to their catalytic properties, are considered to have a major influence on catalytic activity: the Mn oxidation state [59, 66, 114] and Mn/O atomic arrangement [132]. The former is believed to play a dominant role in catalytic reactions, whereas the latter is believed to have only a marginal effect [114]. The morphology of catalysts is also a determining factor in catalyst performance as it affects the active site concentration, [133] but it plays an extrinsic role without affecting the electronic structure of each active site itself. A high concentration of the Mn^{3+} (d^4) oxidation state is often detected in the manganese oxide catalysts with high catalytic activity [59, 1115, 116]. Previous studies suggest that the birnessite-like MnO_x and Mn_2O_3 exhibit higher catalytic performance than Mn_3O_4 and MnO_2. The series of a declining performance follows an order, (birnessite, Mn_2O_3) > Mn_3O_4 > (MnO, MnO_2), that basically mirrors the decrease of the Mn^{3+} concentration in these manganese oxides [59, 134]. The Mn^{3+} state is, however, not stable in certain environments and, for example, can disproportionate into Mn^{2+} and Mn^{4+} in neutral solution, causing a decline in catalytic activity [115]. Indeed, suppression of the disproportionation reaction, and consequent stabilization of Mn^{3+}, has been linked to a significant increase in catalytic activity [53, 115, 132, 135].

This is supported by investigations showing that MnO_x films electrodeposited from aqueous electrolytes, which are poorly active at pH 7, show much improved activity in basic solution (pH > 9), a regime under which Mn^{3+} is stabilized [115, 117]. It would be advantageous if highly active MnO_x water oxidation catalysts could be developed that operate under neutral chemical environments to minimize loss/degradation processes. The main purpose of this chapter is to understand the mechanism of catalytic improvements under heat treatment or various values of electrolyte pH by identifying the effective Mn oxides species in MnO_x films.

4.2 On the Origin of Improvement of MnO_x Films in Water Oxidation Catalysis Induced by Heat Treatment

This part of thesis is taken from following Publication.

On the Origin of the Improvement of Electrodeposited MnO_x Films in Water Oxidation Catalysis Induced by Heat Treatment.

Munirah Khan, Jie Xiao, Fengling Zhou, Mikhail Yablonskikh, Douglas R. MacFarlane, Leone Spiccia, and Emad F. Aziz.

ChemSusChem. 8 (2015) 1980–1985. DOI: 10.1002/cssc.201500330

It is already demonstrated that a simple heat treatment at a low temperature (<120 °C) for 30 min converts low-activity MnO_x films electrodeposited from ionic liquid-containing aqueous electrolytes into highly active catalysts. The improvement in water oxidation catalysis was remarkable, reaching as high as a 60-fold increase in catalytic activity [128]. Analyses of the films by XRD, SEM, EDX, FTIR and Raman spectroscopy revealed that the transformation to the highly active form on heat treatment is not accompanied by significant changes in the film morphology or chemical composition. However, an irreversible dehydration process occurs that removes structural water and hydroxyl species, and there is also the growth of small amounts (3-10 %) of reduced Mn species (Mn^{2+} or Mn^{3+}). Unfortunately, these characterization methods do not reveal changes in the electronic structure of the MnO_x films under the heat treatment, an intrinsic property of catalysts that can define their catalytic performance. The valence electronic structure of catalysts is usually heavily involved in catalytic action. Probing the valence states at specific catalytic sites is particularly desirable since they are very sensitive to the oxidation state of the element of interest and its surrounding chemical environment (ligand field); it is, therefore, possible to uncover details about the mechanism of catalysis. In this work, X-ray absorption spectroscopy (XAS) is employed at the manganese L-edge and oxygen K-edge to investigate the valence electronic structure of the MnO_x films following heat treatment at various temperatures.

XAS is capable of revealing the unoccupied valence orbitals for specific elements (catalytic sites) by resonantly exciting the characteristic core electronic levels. Due to the amorphous nature of the electrodeposited MnO_x films, surface sensitive techniques, such as photoelectron spectroscopy, which is often used to characterize the valence electronic structure, are not suitable in this study due to the very short mean-free-path of the photoelectron. On the other hand, XAS, an element-specific photon-in photon-out measurement, would be an ideal tool for gaining valuable information about the local electronic structure of catalytic sites within a bulk material. It has been very successfully realized in previous studies on similar Mn complexes [67, 96].

4.2.1 Sample Preparation

The manganese oxide powders of MnO, Mn_3O_4, Mn_2O_3, MnO_2 and birnessite were purchased from Sigma Aldrich and spread on conducting Cu tapes for further XAS measurements. The XA spectra of MnO was, however, later replaced by the spectra measured on $Mn(ClO_4)_2.6H_2O$ instead due to the instantaneous oxidation of MnO in air. The $Mn(ClO_4)_2.6H_2O$ powder, also purchased from Sigma Aldrich, was dissolved into acetonitrile and subsequently doped into Nafion film before the XAS measurement. This has been proven to be a viable technique for acquiring a genuine Mn^{2+} spectrum [96]. The acquired Mn L-edge XA spectrum from $Mn(ClO_4)_2.6H_2O$ was almost identical to the spectrum taken from the crystalline MnO in the literature, [113] and is thus used in this work to represent the XA spectrum of MnO. The oxygen K-edge XA spectrum of MnO is also impossible to be obtained properly because of sample oxidation. The MnO_x films were prepared using an electrodeposition method [128]. Ethylammonium nitrate (EAN) was synthesized by neutralizing ethylammonium hydroxide with diluted HNO_3 solution followed by the removal of water using a rotary evaporator at 50 °C and reduced pressure for 2h. The aqueous electrolytes for the deposition consisted of $Mn(CH_3COO)_2$ (10mM) and EAN (1M), and the pH was adjusted to 1.8 using diluted HNO_3 (this electrolyte will be described as aqEA1). Electrodeposition and subsequent heat treatment followed the exact procedures described in our previous study [128]. Fluorine-doped tin oxide (FTO, sheet resistance 15Ω/□) glass slides with a $0.5x0.5cm^2$ active electrode area were used as the substrates. The electrodeposition of the MnO_x films was carried out by using a three-electrode electrochemical system with the FTO glass, saturated calomel electrode (SCE) and Ti foil as the working, reference and counter electrode, respectively. All films were electro-deposited by applying a constant current density of 200 μAcm^{-2} for 10 minutes at room temperature. After deposition, the films were thoroughly rinsed with distilled water and dried under a N_2 flow. The as-grown MnO_x films were then heat treated at 50, 90 and 120 °C for 30min in air on a hotplate fitted with a temperature controller.

4.2.2 Experimental Methods

The XAS experiments were carried out at the U41-PGM beamline and LiXEdrom endstation at the synchrotron facility BESSY II (Berlin, Germany) [136, 137]. The as-grown MnO_x film and heat treated samples were mounted in a vacuum chamber with base pressure of 10^{-8} mbar. The XA spectra were measured in total electron yield (TEY) mode by detecting the sample drain current. In this way, the beamline flux could be significantly reduced without sacrificing the quality of the spectra and possible beam damage could be avoided (in vacuum manganese oxides are typically very sensitive to intense X-ray beams, which can quickly reduce Mn from higher oxidation states to Mn^{2+}). All measurements were repeated multiple times at various sample spots to assure the reproducibility of the data as well as to enhance the signal-to-noise ratio. The acquired XA spectra of the well-defined manganese oxides MnO ($Mn(ClO_4)_2.6H_2O$), Mn_3O_4, Mn_2O_3, MnO_2 and birnessite were almost identical to those in the literature, [104, 113, 138] proving no beam damage on the manganese oxide films (Appendix A.2).

4.2.3 Results and Discussion

The effect of the heat treatment on the electronic structure, especially on the valence levels, of the electrodeposited MnO_x films has been probed by the X-ray absorption spectroscopy (XAS) at the Mn L-edge and oxygen K-edge. The Mn L-edge XA spectra of the four MnO_x films, each subjected to their respective heat treatment before the X-ray measurements, were examined first as they could provide valuable information about the Mn catalytic sites. The XA spectra were normalized and then aligned to their background for a clear intensity comparison, as shown in Figure 4.1. The four manganese L-edge XA spectra are quite similar except for the slight intensity enhancement with the increasing temperature in the absorption energy range of 639-643 eV within the Mn L_3-edge, as highlighted in the enlarged inset in Figure 4.1 (the Figure separates the four XA spectra into two categories, as-grown/50 °C and 90 °C/120 °C). The spectra in each category are almost identical, indicating that no change of the electronic structure occurs at the manganese sites and their surrounding ligand fields when the samples are heated to 50 °C or from 90 to 120 °C for 30min. The intensity enhancement of the XA spectral features at around 640.2 and 641.6 eV, on the other hand, indicates that the MnO_x film undergoes some change in the electronic structure of the Mn sites when heated up to 90 °C, as shown in Figure 4.1. To identify the origin of these enhanced spectral features, a series of the well-defined manganese oxides varying in their Mn oxidation states, that is, MnO (2+), $Mn(ClO_4)_2 \cdot 6H_2O$ (2+), Mn_3O_4 (2+, 3+), Mn_2O_3 (3+), MnO_2 (4+) and birnessite (3+, 4+), were also measured by XAS at the Mn L-edge to establish the reference spectra, as shown in Figure 4.3.

A comparison of the reference spectra in Figure 4.3 with the XA spectra of the MnO_x in Figure 4.1 indicates that the spectra of the as-grown and the heat treated MnO_x samples are in general very similar to that of birnessite. The enhanced spectral features of the MnO_x, highlighted in the inset of Figure 4.1 matches perfectly the two major absorption features of Mn_3O_4 at the Mn L_3-edge. These observations suggest that the majority of the MnO_x in the films is in the birnessite phase and that heat treatment at 90 °C or higher mainly leads to a small increase of the Mn_3O_4 contribution. The linear fitting of the measured XA spectra of MnO_x using the reference manganese oxide spectra discussed below will further clarify that this enhancement of the Mn_3O_4 contribution represents a phase transition from birnessite to Mn_3O_4 species induced by the heating. The average Mn oxidation state is thus reduced upon the heat treatment at 90 °C because a certain amount of the birnessite phase with a mixed (3+, 4+) oxidation state is converted into Mn_3O_4 phase with a mixed oxidation state of (2+, 3+). This observation is in line with previous XAS study at the manganese K-edge that indicated an overall reduction of the oxidation state of the MnO_x films when the sample was heated up to 90 °C [128].

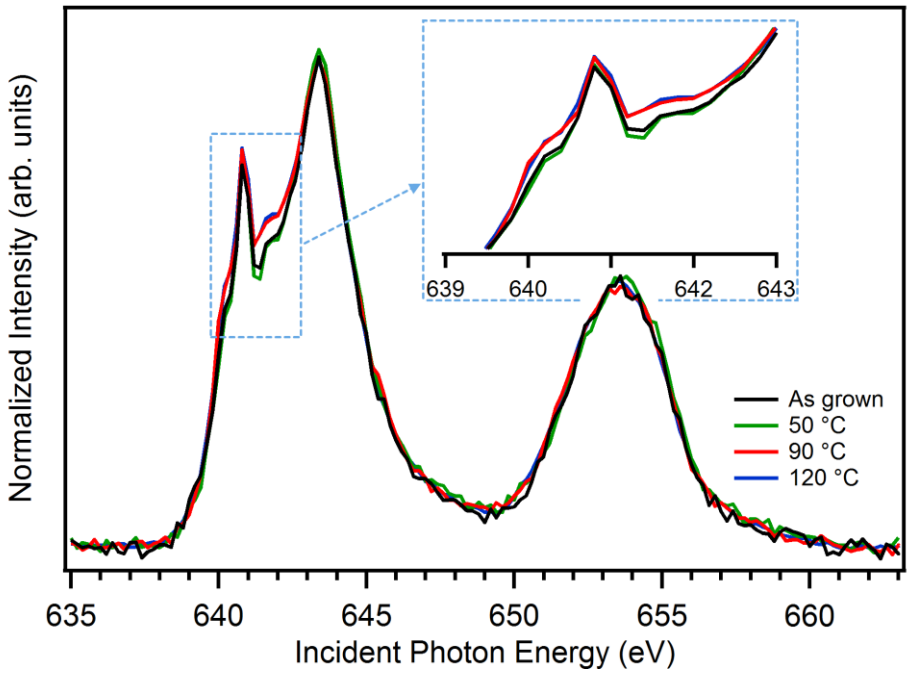

Figure 4.1. Mn L-edge XA spectra of the electrodeposited MnO_x films heattreated at various temperatures: as-grown, 50, 90, and 120 °C. All spectra are normalized and then aligned to their individual background for a clear intensity comparison. The spectral differences are highlighted by a dashed rectangular and further enlarged as an inset in the Figure for a better identification of the dissimilar features. The black trace represents the as-grown MnO_x film, whereas the green, red and blue traces indicate the MnO_x films receiving 50, 90 and 120°C heat treatments for 30 min, respectively.

A previous study also showed that the MnO_x film, when heated to 90 °C, exhibited the best catalytic performance among all the heat-treated samples, [128] indicating that the electronic structure after the 90 °C heating should possess certain distinctive features when compared to the other heat-treated MnO_x films. The manganese L-edge XA spectrum of the 90 °C sample is, however, identical to that of the 120 °C sample, as shown in Figure 4.1 which makes the electronic structure at the Mn sites indistinguishable between the 90 and 120 °C samples. Thus, there is no apparent change of the Mn oxidation state and the Mn/O geometrical arrangement (that affects the Mn surrounding ligand fields) at these temperatures. The expected distinctive spectral features for the 90 °C sample are not observed in the Mn spectra and then must appear in the oxygen spectra. Indeed, the oxygen K-edge XA spectra, shown in Figure 4.2 are able to distinguish the 90 °C spectrum from the rest. The spectral change observed between the 90 and 120 °C samples in Figure 4.2 is unlikely to be caused by the oxygen atoms that directly bond to the Mn atoms in the MnO_x structure as any variation of these oxygen atoms should alter the ligand fields around the Mn sites and consequently change the Mn L-edge XA spectra in Figure 4.1. The general reduction in the oxygen K-edge spectral intensity at 120 °C, compared to the other oxygen spectra in Figure 4.2 is most likely caused by the irreversible removal of the water molecules accommodated within the layered birnessite structure, as suggested by previous study [128]. The absorption edge of the oxygen K-edge XA spectrum of pure water usually starts at 534 eV, and low energy absorption features located below 534 eV are often attributed to the interaction of oxygen with metal atoms, as demonstrated in the cases of water interactions with alkali or transition metals in previous works [139, 140].

Based on this argument, a deepening of the spectral dip at about 531 eV in Figure 4.2 for the 90 °C spectrum when compared with the as-grown and 50 °C spectra appears to be connected to changes in the Mn-O interactions. This is consistent with proposed phase transition from birnessite to Mn_3O_4 producing a unique electronic structure that leads to the superior catalytic performance for the MnO_x films treated at 90 °C. The O K-edge XA spectra of the as-grown and 50°C treated samples in Figure 4.2 are still indistinguishable, similar to the situation of the Mn L-edge XA spectra in Figure 4.1. Previous study suggests that only the weakly adsorbed water molecules that have little or no significant interactions with the MnO_x framework are removed from the film surface at 50 °C [128]. As all MnO_x films were measured inside a vacuum chamber in this work, the vacuum condition could produce a similar effect as the 50 °C heating that is, removing the superficial water molecules from the as-grown sample. This could be the reason why no intensity reduction was observed in the 50 °C oxygen K-edge spectrum when compared to the as-grown spectrum. The spectral evolution for the higher temperature treatments is attributable to the removal of structural water or hydroxyl species embedded, presumably within the layers MnO_x of the birnessite phase.

This process results in the observed catalytic improvement (accompanied by the phase transition from birnessite to Mn_3O_4) at 90 °C and deterioration at 120 °C. The poorer MnO_x catalytic performance after the 120 °C heat treatment, accompanied by the excessive loss of water/hydroxyl species from the MnO_x film, indicates the importance of having a certain amount of structural water in these catalysts.

4.2.4 Linear Fitting

The conclusions drawn above are solely based on the qualitative discussion of the measured XA spectra at the manganese and oxygen edges. Further quantitative analysis of the manganese L-edge XA spectra uncovers additional detailed information about the specific manganese oxide species existing in the MnO_x structure. Fitted manganese L-edge XA spectra are shown in Figure 4.4 using linear combinations of the spectra of well-defined reference manganese oxides, shown in Figure 4.3, as the basis functions, as has been successfully adopted in previous analyses of the manganese oxides shown in Chapter 3 [96, 118].

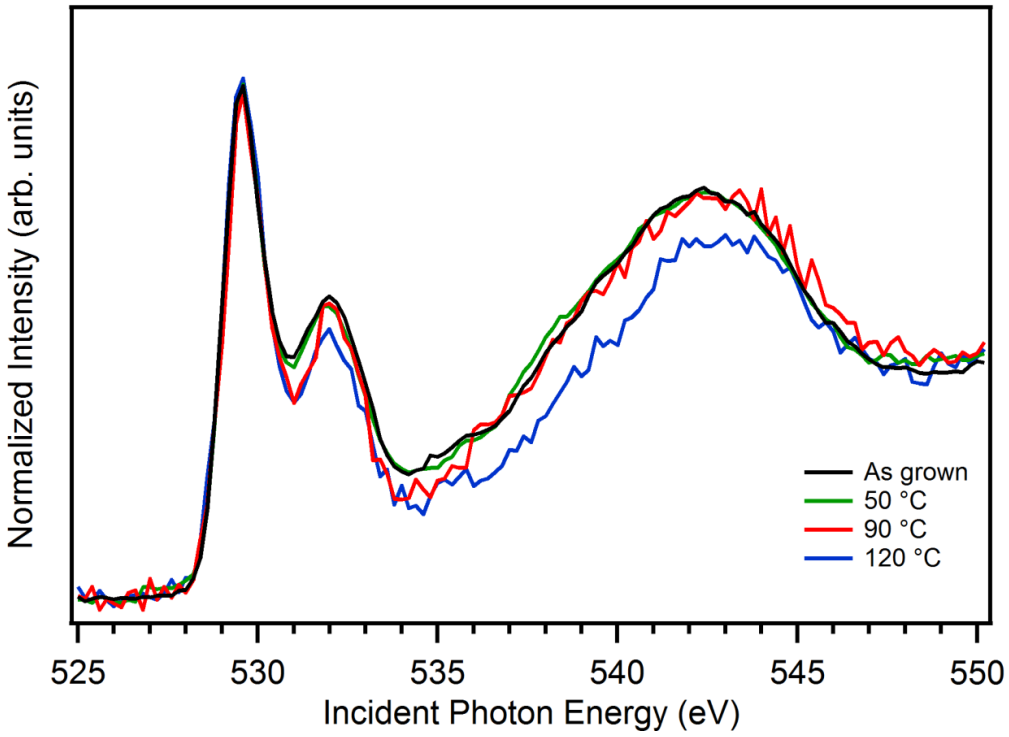

Figure 4.2. O K-edge XA spectra of the electrodeposited MnO_x films heat treated at various temperatures: as-grown, 50, 90, and 120 °C. All spectra are normalized and then aligned to their individual background for a clear intensity comparison. The black trace represents the as-grown MnO_x film, whereas the green, red and blue traces indicate the MnO_x films receiving 50, 90 and 120 °C heat treatments for 30 min, respectively.

The fitted spectra agree extremely well with the measured spectra, as shown in the upper panel of Figure 4.4 indicating that the reference manganese oxides contain all the possible manganese oxide phases comprising the Mn oxidation states and Mn/O atomic arrangements present in the mixed MnO_x materials. In other words, the Mn L-edge XA spectra of the reference manganese oxides represent a sufficient basis set that can be used for the linear expansion of the spectra of the mixed MnO_x phases. Further inspection of the expansion coefficients, as shown in Table 4.1, reveals that not all the bases (reference spectra) are necessary. Birnessite and Mn_3O_4 are the two leading phases in the MnO_x structure with 76-84 % and 13-21 % contributions, respectively, which is in good agreement with the previous study showing 80 % birnessite and 20 % Mn_3O_4 in the MnO_x films by the linear fitting of the Mn K-edge XA spectra [118]. MnO only plays a marginal role with about 3 % contribution, and Mn_2O_3 and MnO_2 make no measurable contribution.

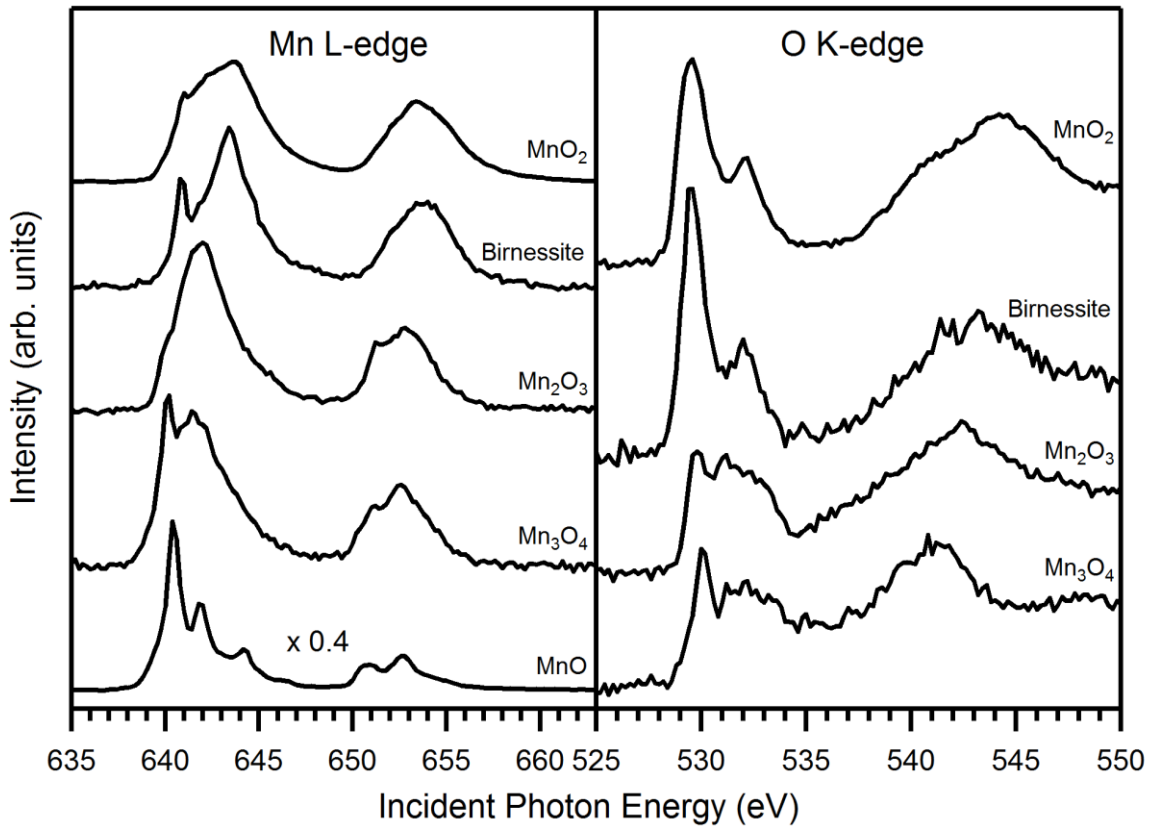

Figure 4.3 Mn L-edge and O K-edge XA spectra of the reference manganese oxides. All spectra are normalized to their respective background for intensity comparison. The overall intensity of the XA spectrum of the MnO ($Mn(ClO_4)_2 \cdot 6H_2O$) is reduced to 40% for a better view. The O K-edge XA spectrum of the MnO is absent because of the infeasibility of acquiring the undistorted O data due to the instantaneous oxidation of MnO when exposed to air.

The contribution of each manganese oxide, birnessite, Mn_3O_4 and MnO, are plotted in the lower panel of Figure 4.4 to provide a clear illustration of the percentage shift at various heating stages. The shift only occurs when the MnO_x films are heated up to 90 °C, consistent with the two categories discussed previously for Figure 4.1. Contrary to the common conception in the literature that birnessite is generally more catalytically active than Mn_3O_4, [118] the 8 % increase of the Mn_3O_4 phase, along with the same amount of decrease of the birnessite phase after the 90 °C heat treatment, actually suggests that Mn_3O_4 may be playing a significant role in the catalytic activity. The small amount (8 %) of transformation of birnessite into Mn_3O_4 is in line with previous analysis , which showed an 3-10 % increase in reduced Mn species after the 90 °C treatment, [128] appears to be connected with the improved MnO_x catalytic performance. Surprisingly, no Mn_2O_3 phase was discovered in the MnO_x material, even though it contains only Mn^{3+} centres which are often believed to be the most effective ingredient in water oxidation catalysis [53, 115, 132, 135].

The absence of the Mn_2O_3 and MnO_2 phases also indicates that the Mn oxidation state is not the only factor determining the MnO_x XA spectra, otherwise the XA spectra of the reference manganese oxides with pure oxidation states, that is, MnO (2+), Mn_2O_3 (3+) and MnO_2 (4+), would be the only sufficient and necessary basis functions for the linear expansion of the MnO_x XA spectra. On the contrary, the mixed oxidation states and characteristic geometric structures, as in birnessite (3+, 4+) and Mn_3O_4 (2+, 3+) phases, constitute the actual catalytic phases present in these MnO_x catalysts. The equal percentage of the birnessite and Mn_3O_4 phases for the 90 and 120 °C spectra in Figure 4.4 indicates that the difference of the catalytic performances after these two temperature treatments does not originate from the Mn-related species in the MnO_x structure. The argument of the loss of the water content discussed above for the oxygen K-edge XA spectra in Figure 4.2 therefore provides a reasonable explanation for the poorer catalytic activity observed after the 120 °C heat treatment. A previous study suggested that the removal of the structural water at 90 °C helps enhance the catalytic performance [128]. In this work, the XAS analysis discovers that the excessive loss of this water at 120 °C may actually degrade the catalytic performance.

Linear fitting for the oxygen K-edge XA spectra in Figure 4.2 is not practical because there exist multiple undefined oxygen sources in the manganese oxides, for example, absorbed water molecules and various carbon oxide species when samples are exposed to air. The reference oxygen K-edge spectra of the well-defined manganese oxides are nevertheless provided in Figure 4.3. From the comparison of the MnO_x spectra with the references, the similarity between the spectra in Figure 4.2 and the birnessite spectrum at the oxygen K-edge in Figure 4.3 is again recognized.

The clear connection between the spectral change in Figure 4.2 and the X-ray absorption features of the Mn_3O_4 in Figure 4.3 however, cannot be established as in the case of analyzing the Mn spectra due to the diverse oxygen sources discussed above. The close resemblance of the oxygen XA spectra between the reference birnessite and MnO_2 further hinders the accurate linear fitting to the oxygen spectra of the MnO_x catalysts.

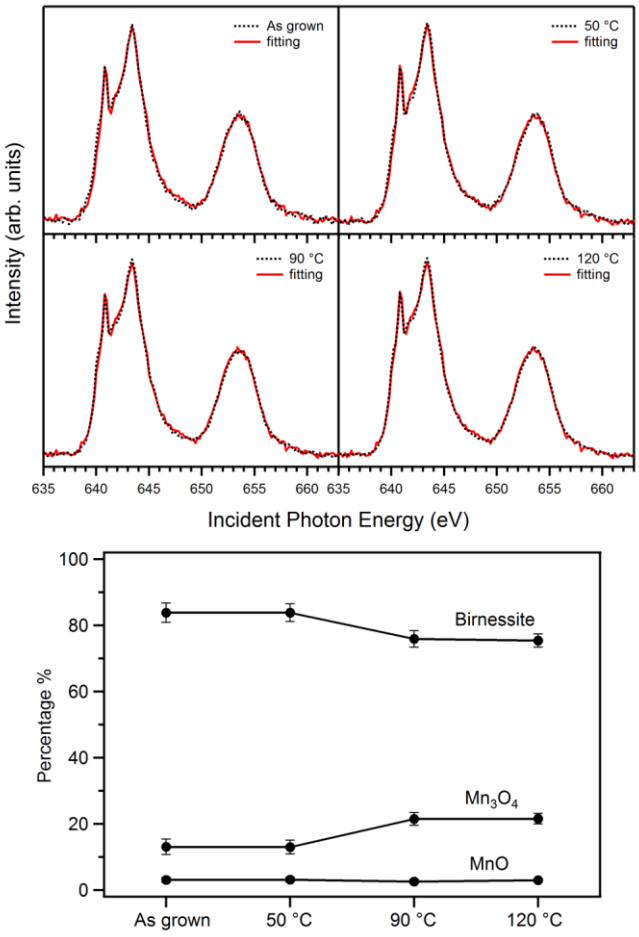

Figure 4.4. Upper panel: Linear fitting of the Mn L-edge XA spectra of the MnO_x films heated at indicated temperatures by linear combinations of the reference XA spectra of the well-defined manganese oxides: MnO ($Mn(ClO_4)_2.6\ H_2O$), Mn_3O_4, Mn_2O_3, MnO_2 and birnessite. The black dashed line traces, identical to the spectra in Figure 4.1 and the red solid line traces represent the measured spectra and fitted spectra, respectively. The reference XA spectra and the fitting procedure are given in the Figure 4.3. Lower panel: Percentages of the well-defined manganese oxide species constituting the MnO_x films at various heating stages, extracted from the fitting coefficients listed in Table 4.1 and plotted with the error bars created by the fitting algorithm.

	Birnessite	Mn_3O_4	MnO	Mn_2O_3	MnO_2
As grown	84	13	3	0	0
50 ℃	84	13	3	0	0
90 ℃	76	21	3	0	0
120 ℃	75	22	3.0	0	0

Table 4.1. Percentage contributions from individual reference manganese oxide species to the heat-treated MnO_x catalysts, derived from the fitting process for the Mn L-edge XA spectra presented in Figure 4.4, with the reference XA spectra in the left panel of Figure 4.3 as the basis set.

The percentage values are calculated according to the following linear fitting algorithm.

Linear fitting algorithm:

Fitted spectrum (red traces in Figure 4.3) = a*Birnessite+b*Mn_3O_4+c*MnO+d*Mn_2O_3+e*MnO_2

Percentage of Birnessite = a/(a+b+c+d+e)

Percentage of Mn_3O_4 = b/(a+b+c+d+e)

Percentage of MnO = c/(a+b+c+d+e)

Percentage of Mn_2O_3 = d/(a+b+c+d+e)

Percentage of MnO_2 = e/(a+b+c+d+e)

4.3 On the Origin of Improvement of MnO_x Films in Water Oxidation Catalysis Induced by Various Electrolyte pH

Recently, a novel method to deposit thin films of MnO_x is reported [129]. A variety of manganese oxide nanostructures with phases varying in composition from birnessite to Mn_3O_4, can be electro-deposited in a controllable fashion on FTO substrate from a hydrated ionic liquid (Ethyl ammonium nitrate) at 120 °C. An investigation of the influence of pH on the deposition electrolytes revealed systematic variations in the chemical composition, oxide phase and morphology of the films. It was shown that film exhibiting low catalytic activities was composed of Mn_3O_4, while those of high activity showed birnessite-like and Mn_2O_3 manganese oxide phases [129]. However, precise determination of contribution of each phase and 3d occupation was still lacking. In this section, Mn L and oxygen K-edges are studied for these catalysts in order to understand their electronic structure. XAS spectroscopy at Mn L-edge is sensitive to the valence structure of the 3d level, the spin state of Mn and the local symmetry of the coordination environment at Mn sites. This is a rich amount of information relative to what is available from K-edge XANES spectra. XAS is an element specific probe, i.e. only electron density around the element of interest is probed. However, the main challenge of using soft X-rays is that the samples may be subjected to X-ray damage [96].

4.3.1 Sample Preparation

Electrochemical deposition of thin films of MnO_x on FTO glass substrate (sheet resistance 115 ohms/m^2) was carried out using a three-electrode electrochemical cell. FTO cleaned ultrasonically was used as working electrode whereas a Ti foil was used as counter electrode along with Ti wire as pseudo-reference electrode. An area of 0.5x0.5cm^2 was used for deposition of the catalyst by protecting the active area of FTO with laser etching and Kapton tape masking. Ethylammonium Nitrate (EAN) was prepared using the procedure explained in section 4.2.1. An electrolyte with composition of 90% Ethylammonium Nitrate (EAN), 10% water and 10mM of Mn $(CH_3COO)_2$ was used to deposit films at 120 °C. This catalyst was named E0 as it was prepared from neutral electrolyte. Other catalysts were deposited by changing pH of electrolyte either by addition of HNO_3 (for acidic electrolytes) or by Ethylamin (for basic electrolyte). Electrochemical deposition was conducted in chronopotentiometry mode at a constant current density of 200 μAcm^{-2} for 10 min for all the catalysts. After depositions, films were thoroughly rinsed with deionized water and dried with nitrogen (N_2) purge. All the reference oxides were bought from Sigma Aldrich (MnO_2, Mn_2O_3, and Mn_3O_4). XAS and RIXS spectra were measured using the same procedure as described in section 4.2.2

4.3.2 Results and Discussion

Manganse L-edge XAS spectra were measured in total electron yield (TEY) mode as shown in Figure 4.5. All spectra were normalized for a clear intensity comparison. The absorption features in the region of 640–648 eV are assigned to the Mn $2p_{3/2}$–3d (L_3-edge) transitions, and those in the region of 650–659 eV to the Mn $2p_{1/2}$–3d (L_2-edge) transitions. Oxygen K-edge spectra for all the catalysts are presented in Figure 4.6. Three set of catalysts with notations A1-A2, E0, B1-B2, are shown in Figure 4.5. E0 is deposited from neutral precursor solution while other two series are deposited from acidic and basic electrolytes respectively. It was reported that A2 and B2 electrodeposited from highly acidic and highly basic electrolytes were least active catalysts while A1 and B1 from less acidic and less basic electrolytes were marked as efficient catalysts. However, the catalyst prepared from neutral electrolyte E0 was ranked as best catalyst [129].

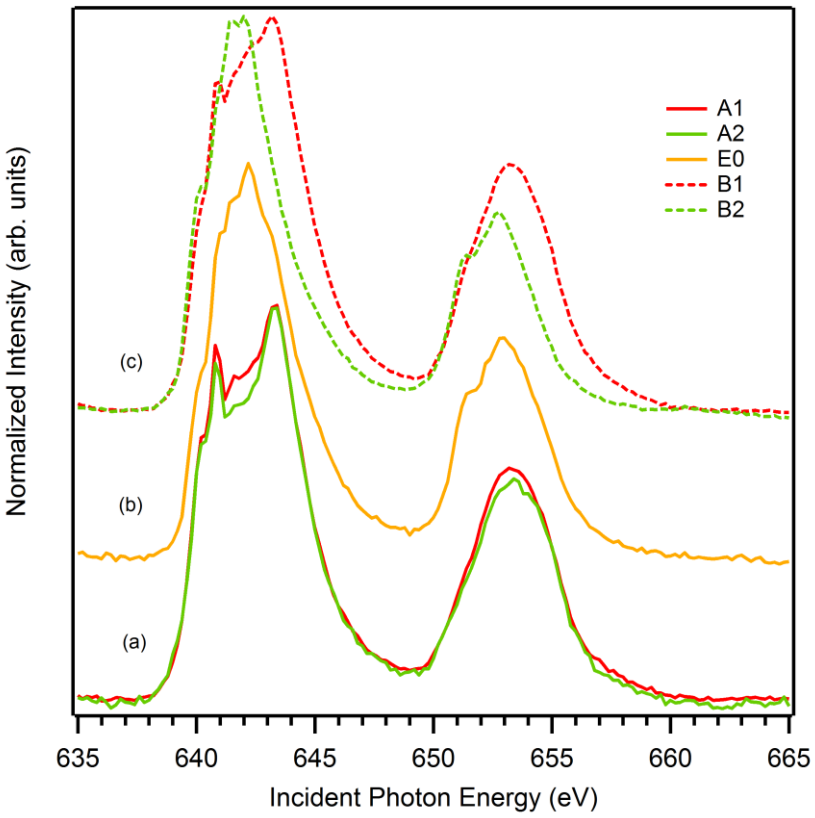

Figure 4.5. Mn $L_{2,3}$ XAS measured in TEY mode of MnO_x catalysts deposited from a range of pH values for the electrolyte of solution. The red traces are for catalysts deposited from acidic (A1) and basic electrolytes (B1). The orange trace represents catalyst E0 prepared from neutral electrolyte. The green traces are for catalysts deposited from more acidic (A2) and more basic electrolytes (B2).

X-ray absorption spectra in Figure 4.5 show significant spectral shape changes for A1, E0 and B1 for the main L_3-edge absorption features although all of them are good catalysts. The spectrum of E0 significantly resembles Mn_2O_3 (Mn^{2+}, Mn^{3+}) when compared to Mn_2O_3 spectra in Figure 4.3 and is very different from A1 and B1 which are more close to birnessite, and MnO_2 (Mn^{3+} and Mn^{4+}) shown in Figure 4.3. Catlysts A1 and A2 deposited from acidic precursors in Figure 4.5a are similar to birnessite structure shown in Figure 4.3. Comparing the oxygen K-edge of these catalysts shown in Figure 4.6a to the oxygen K-edge spectra of birnessite in right panel of Figure 4.3, it becomes evident that A1 and A2 have birnessite as the most important contribution. XAS spectra of A1 catalyst in Figure 4.5a are significantly different than A2 around 642.0 eV.

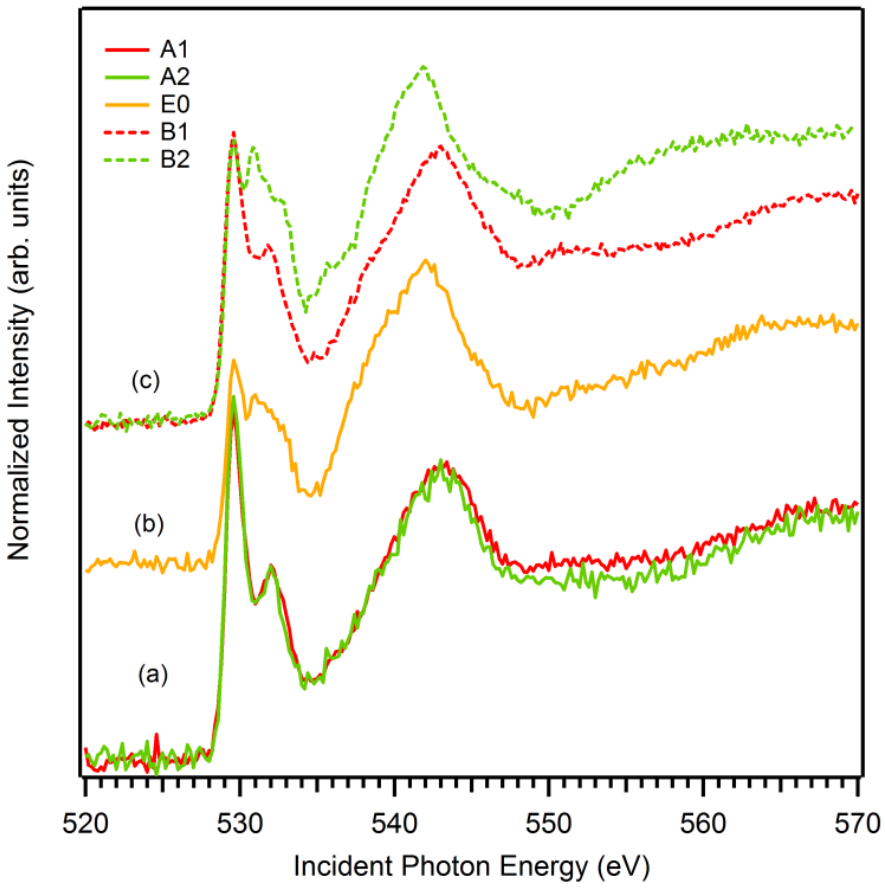

Figure 4.6. Oxygen K-edge XA spectra measured in TEY mode for MnO_x catalysts deposited from various electrolyte pH. The red traces are for catalysts deposited from the less acidic (A1) and the less basic electrolytes (B1). The orange trace represents catalyst E0 prepared from neutral electrolyte. The green traces are for catalysts deposited from highly acidic (A2) and basic electrolytes (B2).

This rise of intensity at this energy may be due to contribution of Mn^{3+} from Mn_2O_3. The spectraum of second best catalyst B1 is different from the other catalyst B2 prepared from the more basic electrolyte and contains contribution from all reference oxides. The spectrum of B2 is almost similar to Mn_2O_3 and Mn_3O_4. More amount of hydroxyl ions present in basic precursor of B2 will lead to the formation of Mn_2O_3 and Mn_3O_4 according to the Pourbaix diagram dicussed in Figure 1.5. The spectrum of B1 also resembles the birnessite but not completely, so it can be assumed that other oxides are also present in good amount. The B2 catalyst is very similar to reference spectra of Mn_2O_3 and Mn_3O_4. In order to quantify the amount of possible oxides present in all catalysts, measured spectra of Mn L-edge are fitted by a linear combination of reference oxides as shown in Figure 4.7.

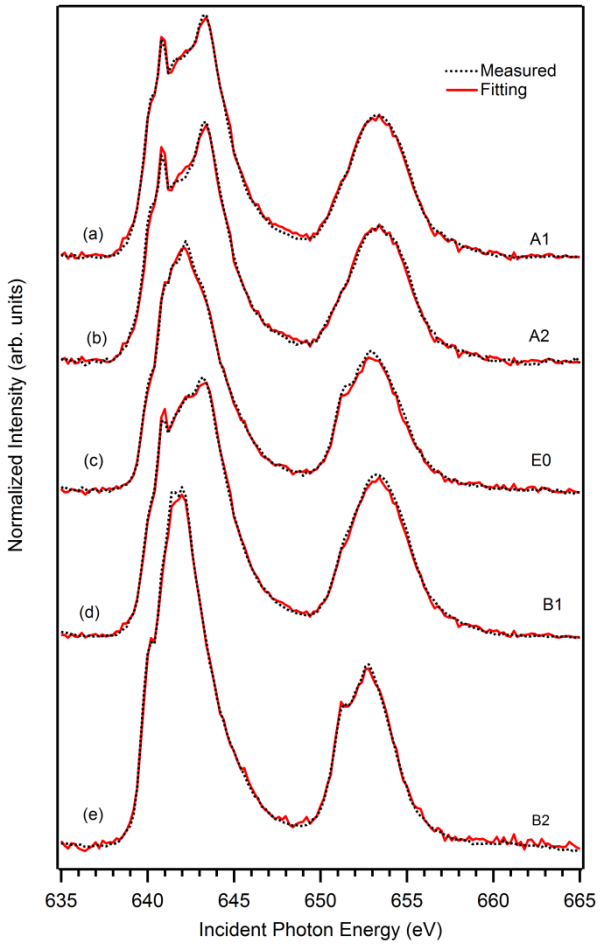

Figure 4.7. Linear fitting of the Mn L-edge XA spectra of the MnO_x catalysts deposited from electrolytes of different pH by linear combinations of the reference XA spectra of the well-defined manganese oxides: MnO ($Mn(ClO_4)_2.6H_2O$), Mn_3O_4, Mn_2O_3, MnO_2 and birnessite. (a, b): catalysts prepared from acidic electrolyte (A1, A2). (c): catalyst prepared from neutral electrolyte (E0). (d, e): catalysts prepared from basic electrolyte (B1, B2). The black dotted lines are identical to the spectra in Figure 4.5 and the red solid line traces represent the fitted spectra. The reference XA spectra and the fitting procedure are given in Figure 4.3.

The fitted spectra presented in Figure 4.7 agree very well with the measured spectra. The comparison of percentage contribution of each oxide present in MnO_x catalysts is shown in Figure 4.8. This shows that each catalyst contains contributions from reference oxide species (MnO, Mn_2O_3, Mn_3O_4, MnO_2 and birnessite) which are shown in Table 4.2. The contribution of birnessite within A1 and A2 is 58 % and 65 % respectively (Table 4.2) which confirms them to be birnessite structure as discussed above for Figure 4.5. However A1 also has a small amount of 2 % Mn_2O_3 and 33 % of Mn_3O_4 in comparison to A2 which has 31 % Mn_3O_4 with no Mn_2O_3 contribution. The high efficiency of A1 over A2 may be related to this small amount of Mn_2O_3. The most efficient catalyst E0 has a major amount of 48 % Mn_2O_3 along with 31 % Mn_3O_4 and 17 % of birnessite (Table 4.2). This result is different from K-edge XAS and EDX experiments which characterized E0 catalyst to be composed of birnessite and Mn_2O_3 [129]. The spectrum of B1 catalysts is fitted with 41% birnessite, 16% Mn_3O_4, 20 % Mn_2O_3 and 23 % MnO_2, while B2 has shown a very high amount of 78 % Mn_2O_3 and 22 % Mn_3O_4 with no contribution of MnO_2 or brinessite. The contribution of Mn_2O_3 and Mn_3O_4 oxides for E0 and B1 can be seen in Figure 4.8.

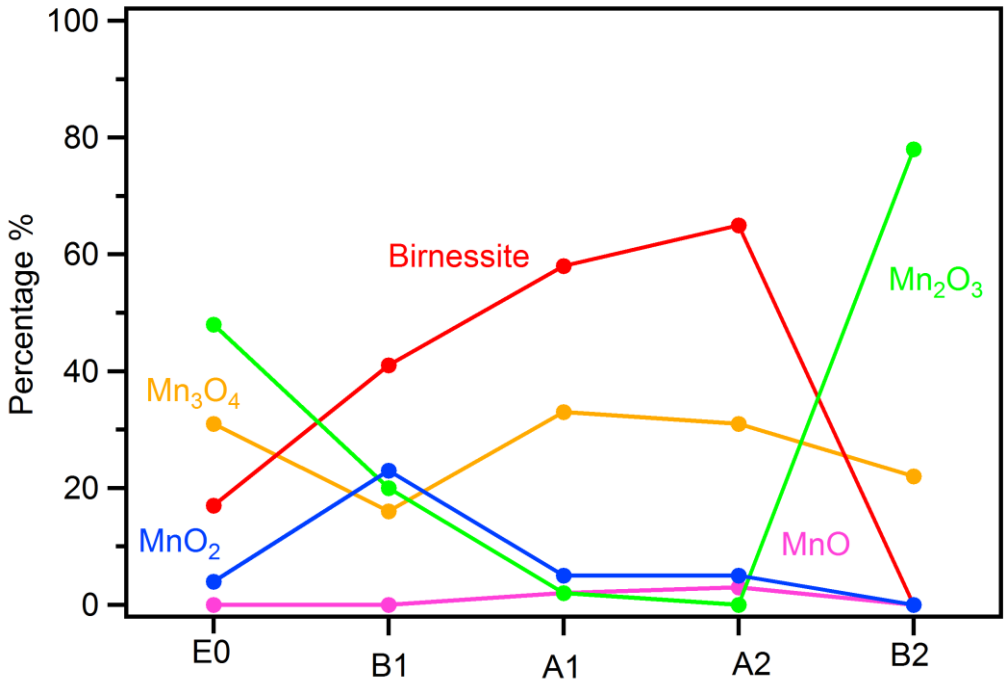

Figure 4.8: Percentages of the well-defined manganese oxide species constituting the MnO_x films, extracted from the fitting coefficients listed in Table 4.2.

	Birnessite	Mn_3O_4	MnO	Mn_2O_3	MnO_2
E0	17	31	0	48	4
A1	58	33	2	2	5
A2	65	31	3	0	1
B1	41	16	0	20	23
B2	0	22	0	78	0

Table 4.2. Percentage contributions from individual reference manganese oxide species to the MnO_x catalysts prepared from different pH values, derived from the fitting process for the Mn L-edge XA spectra presented in Figure 4.5. The percentages from the fitting co-efficients are calculated with the similar procedure shown in section 4.2.4.

4.4 Conclusions

Heat treatment has previously been proven to be an effective method to significantly improve the catalytic performance of MnO_x films electrodeposited from ionic liquid-containing aqueous electrolytes. This study further discovers that this improvement may actually be arising from the conversion of a small amount (8 %) of the total MnO_x material from the birnessite phase to the Mn_3O_4 phase when the films are heated up to 90 °C. The water molecules accommodated within the transformed birnessite layered structure before the phase transformation are lost on heating. This irreversible dehydration process was discovered in previous study [128] and is now understood more precisely at a microscopic level. It was observed that heat-treatment of catalyst at higher temperature (120 °C) that removes more structural water does not lead to further phase transformation but to poorer catalytic performance as shown in Figure 4.9. This finding clearly indicates that certain amount of the structural water molecules embedded within the layered birnessite phase is important for water catalysis. The minimum amount of the structural water required for the superior catalytic performance and its role in the water oxidation catalysis will be probed in future investigations.

The electrolyte pH is shown to have a signifcant effect on the catalytic activity as well. It has been reported that catalysts deposited from a neutral precursor were higher in activity than other catalysts deposited from acidic or basic electrolytes [129]. XAS spectra were measured at manganese L-edge and oxygen K-edge to investigate the electronic structure of these catalysts. The linear combination of various reference oxides was used to fit the measured spectra. All the catalysts were found to be mixture of combinations of two or more oxides. The best catalyst from a neutral precursor was composed of MnO, M_2O_3 , Mn_3O_4, Birnessite and MnO_2. This is in contrast to low activity catalysts prepared from acidic or basic electrolyte which are either a combination of birnessite, Mn_2O_3 and Mn_3O_4 or a combination of Mn_2O_3 and Mn_3O_4. A right combination of Mn oxide species might be the key to achieve high water splitting efficiency. The detailed mechanism is still under investigation.

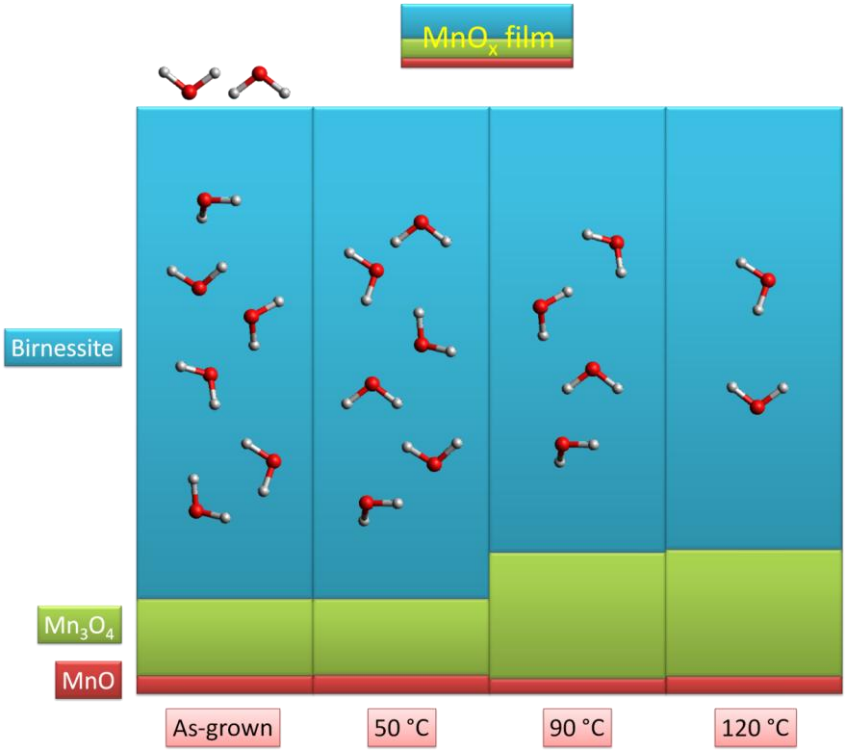

Figure 4.9. Heat treatment of the MnO_x films lead to successive water losses at the surface for adsorbed water at 50 °C and in the bulk for structural water at 90 and 120 °C. The loss of the structural water embedded in birnessite phase at 90 °C triggers a small amount of birnessite transformation into Mn_3O_4 phase, and results in a significant improvement in catalytic performance.

Chapter 5

Summary and Outlook

5.1 Summary

Water splitting into hydrogen and oxygen molecules is recognized as a clean and sustainable way to store energy. For the energetically demanding water oxidation reaction, a minimum electrical potential of 1.23 V is required (vs. standard hydrogen electrode (SHE), pH 0). Practically, however, overpotential is needed to realize this mechanistically complex process, and there is great interest in highly active catalysts that reduce this overpotential. Transition metal based oxides have been widely recognized as promising catalysts for water oxidation that reduce overpotential of water oxidation reaction mimicking the OEC complex. Since a manganese cluster is the only known system to catalyze water oxidation in nature, manganese catalysts have been attracting much attention. Manganese oxides (MnO_x) have been demonstrated to be effective water oxidation catalysts whilst also providing structural and mechanistic clues about the nature of the reaction occurring in the OEC.

The improvement in water oxidation catalysis over the years is remarkable. Various approaches have been used to synthesize highly active MnO_x and various treatments applied to the MnO_x in order to improve the catalytic performance. Highly active MnO_x water oxidation catalysts are developed which operate under neutral chemical environments. Despite their relatively simple chemical compositions, many factors have been shown to affect the catalytic activity. Mechanism by which MnO_x catalyzes water oxidation is rather complicated, and poorly understood at a molecular level. In this dissertation, X-ray absorption and resonant inelastic X-ray scattering spectroscopy have been applied to trace the electronic structure of different water splitting manganese catalyst. The aim was to complement earlier works on water splitting catalysts which paved a way to address the mechanism of water oxidation based catalytic reactions happening inside transition metal oxides.

A part of the thesis covers manganese complexes doped into Nafion films deposited on conductive electrodes as water oxidation catalysts. These catalysts are impregnated with anionic sulfonate groups of the Nafion matrix. The anionic sulfonate groups of the Nafion matrix are important such that they allow the ion-exchange of cationic manganese species into the films which are then converted into active catalysts. The complexes decompose into Mn^{2+} species in Nafion, and the prolonged water oxidation catalysis involves a birnessite-like manganese oxide formed on electro-oxidation of the Mn^{2+} species. X-ray absorption spectroscopy (XAS) and resonant inelastic X-ray scattering (RIXS) analyses are used in combination to probe the changes in the electronic structure of a manganese catalyst for water oxidation on application of an electrical potential and visible light illumination.

The electronic structure of Mn 3d orbitals near the Fermi level is well-resolved by these two types of measurements, (especially RIXS) that reveal the local energy gap at the Mn sites in a bulk material (Nafion); the Mn 3d orbitals and Mn oxidation state are altered by the Nafion matrix, electrical potential, and visible light illumination. The local HOMO-LUMO gap at the manganese sites, a critical factor influencing catalytic efficiency, becomes reduced slightly when $[Mn_2O(OAc)_2L_2](ClO_4)_2$ (Mn (III)) is doped into Nafion and further reduced significantly when the electrical potential and visible light illumination are simultaneously applied to Mn (III) doped Nafion films. Such a steady-state condition is not observed when the two stimulations (electrical potential and visible light illumination) are applied separately and the local HOMO-LUMO gap remains relatively large. Only when both an electrical potential and visible light are applied simultaneously under continuous catalytic cycling is the local HOMO-LUMO gap significantly reduced to 1.3 eV. The narrowing of the local HOMO-LUMO gap on catalytic sites, revealed by RIXS analyses along with strongest charge transfer and a higher proportion of Mn^{3+} over $Mn^{2+/4+}$ produce itinerant electrons that contribute to the higher catalytic activity.

From a theoretical point of view, X-ray absorption and resonant inelastic scattering of a number of $Mn^{2+,3+,4+}$ complexes relevant for photo-electrooxidation of water is studied on the RASSCF/RASSI level. The gap between the ground and first excited valence states for Mn^{3+} is notably lower than its values for even oxidation states ($Mn^{2+,4+}$), which is reflected in the unique shape of inelastic scattering spectra. Spin-orbit coupling induced mixing of states with different multiplicities in the valence and core-excited electronic states is analyzed, evidencing the mostly spin-forbidden character of transitions in RIXS spectra. The notably different patterns of spectroscopic features in series of substances not only provide insight into their electronic structure but open the possibility for tracing redox evolution by means of X-ray spectroscopy.

Besides nafion doped MnO_x films, catalysts prepared from ionic liquids have been investigated as non heat treated and heat treated catalysts. A simple heat treatment at a low temperature (< 120 °C) for 30 min converts these low-activity MnO_x films electro-deposited from ionic liquid containing aqueous electrolytes into highly active catalysts. X-ray absorption spectroscopy (XAS) at the Mn L-edge and oxygen K-edge was employed to investigate the valence electronic structure of the MnO_x films following a heat treatment at various temperatures. Linear fitting of experimental spectra were performed through linear combination of reference spectra. All the catalysts were found to be a mixture of Mn_3O_4 and birnessite. It was shown that the higher activity of the best catalyst heat treated at 90 °C for 30 minutes is due to conversion of about 8% of birnessite into Mn_3O_4.

In another experiment, the influence of the pH value of the deposition electrolytes on electronic structure of MnO_x films was revealed systematically by XAS. A variety of manganese oxide nanostructures with phases varying in composition from birnessite to Mn_3O_4 were electro-deposited in a controllable fashion on an FTO substrate from a hydrated ionic liquid (Ethyl ammonium nitrate) at 120 °C. XAS spectra of these catalysts revealed that film prepared from acidic and basic electrolytes are exhibiting low catalytic activities. They were composed of Mn_3O_4, Mn_2O_3 and birnessite with major contribution from birnessite. The catalysts prepared from a neutral precursor showed high amount of M_3O_4, and birnessite phases along with Mn_2O_3 as major contributor.

5.2 Outlook

Elucidations of the local electronic structure on Mn sites described above would not be possible without advanced XAS and RIXS measurements. Having established the feasibility of these measurements it has become possible now to apply these techniques in the study of extensive water-oxidizing complexes in photosystems II (PS II), including those used in homogeneous catalysis. *In situ* RIXS measurements of the local energy gap during the water oxidation process are already planned for further studies with a newly designed electrochemical cell.

To study the roles of Nafion in water catalysis, far and mid infrared spectroscopies was performed *ex-situ* at different stages of the catalyst generation and water oxidation cycle in transmittance mode. The systematic change of sulphonate (SO_3^{-1}) band of Nafion around 1160 cm^{-1} by far infrared spectroscopy and back bone of Nafion polymer (CF_2CF-) was found to be varying from doped to illuminated states. Detailed analysis of these results may provide benchmarks for revealing the modified structure of Nafion hydrophilic and hydrophobic chains during water catalysis. Such signatures can probe the detailed structure of Nafion "water channels" located in the Nafion–water interface upon catalysis. Theoratical calculations are underway to calculate the vibrational bands of Nafion modified by the doped Mn catalysts.

Qualitative trends in the vibrational energies of Nafion will be explained by calculating electronic and/or structural (ionic domain-size) effects. The possible ionic clusters of perfluorinated sulfonic acid formed with Na^+ of the electrolyte will be correlated systematically. Two new manuscripts (one for XAS/RIXS studies of unsupported MnO_x deposited from ionic liquids as a function of pH and other for mid /far infrared studies of nafion in supported MnO_x catalysts) are in the process of writing and will be submitted soon in peer review journals.

In order to better understand dynamic character of a photoactive catalyst (nafion doped), new experiments will be demonstrated at laser lab of Freie universität that will help study the visible light induced time resolved ultra-fast dynamics of doped and biased Mn catalysts. Considering the experimental requirements, a pump source like laser will be needed and high harmonics will be used to probe the catalysis happening on femtosecond scale. The suggested experiments will be carried out in a pump-probe mode, where the Mn-catalysts will be advanced with visible light laser pulses and probed with 3rd harmonics. It will be a crucial step to accomplish investigation of photo dynamics of valence orbitals of under study catalysts. These proposed experiments are very important as they may shed light on the mechanism of catalysis cycle of water splitting through visible light.

To shed further light on water splitting catalysis, photoemission spectroscopy is also planned to investigate Mn-catalysts for supported (nafion doped) and unsupported (directly deposited from ionic liquids and other methods like screen printing) catalysts at BESSY II in near future. Information of the oxidation states and ligation throughout the catalytic cycle will be obtained by performing soft X-ray photo emission spectroscopy. To support the experimental results and interpretations of the experiment, theoretical calculations will be important and are already in progress in collaboration with Professor Oliver Kühn at University of Rostock using ab initio methods and atomic multiplet methods for transition metals.

Appendix

A.1 Stability and Reproducibility of Experiment

To address the possibility that the samples may be changing over time when either exposed to air or under high vacuum during measurement, the following steps were followed. After electrochemical generation of the samples or treatment in solution, the samples were carefully air-dried. This step was not expected to have any effect on the Mn^{2+} samples as Mn^{2+} is stable in Nafion and does not react with oxygen. If it did, the resultant species of the oxidation process would have been seen in previous XAS studies [43, 95]. For the oxidised species, the stability was predicted to be an issue only if the samples were kept as wet films or films which have electrolyte and water in the Nafion channels. In that case, light would cause partial reduction of the oxide and the release of oxygen, changing the sample. The films containing the oxides are stable and show no evidence of converting/reducing to Mn^{2+} when left as dry films. For the possibility of the samples being changed over time in the high vacuum environment of the soft X-ray chamber, spectra were collected at multiple spots on the same sample, one after another. The spectra obtained were reproducible. As the second spot has been subjected to the vacuum for a longer duration without changing, it can be concluded that the samples are stable under the analysis conditions. This is not surprising, as once the samples are dry there will not be any species present that are able to evaporate under the conditions in use.

A.2 Radiation Damage Study

It is well known that the manganese oxide samples undergo photo-reduction under the intense flux of the soft X-rays [102, 106, 113]. Therefore, a systematic study was carried out to check for any possible radiation damage for all Mn catalysts in all states (doped, as biased and light shined). In order to reduce radiation damages, the XAS spectra were recorded in electron yield mode which allowed to drastically reduce the photon flux on the sample (in the soft X-ray range electron yield method has a cross section of ~95%, compared to 1-5% of fluorescence yield). The photon flux was reduced by closing the primary beamline baffles (the one located directly after the undulator) from the 1.2 x1.2, 1.0x1.0 conventional values up to 0.1x 0.2, 0.1x 0.0. The beam flux reduces linearly with the closing of the baffles. The XAS spectra of catalysts and some of the reference oxides samples are shown in Figure A.2.1- A.2.3. To test for radiation damages, the spectra were measured at least twice at the same spot and then to a fresh illuminated spot for each sample. For all the catalysts no intensity change or energy shift was observed for the XAS spectral features measured at different spots and at the same spot (see Figure A.2.1). The fact is that the MnO_x catalysts are doped inside the nafion layer which itself absorbs and therefore attenuate further X-rays. In contrast, for the oxide reference powders, a change in intensity of spectral features was observed upon reducing the synchrotron beam flux. Radiation damages were severe in case of MnO_2 and synthetic birnessite, where manganese is in high oxidation state Mn^{2+}, Mn^{3+} and Mn^{4+}, respectively. Therefore, for these samples the beam line apertures were almost fully closed up to 0.1×0.2, 0.1×0.0. XAS experimental spectra look similar with those reported in the literature [102, 108].

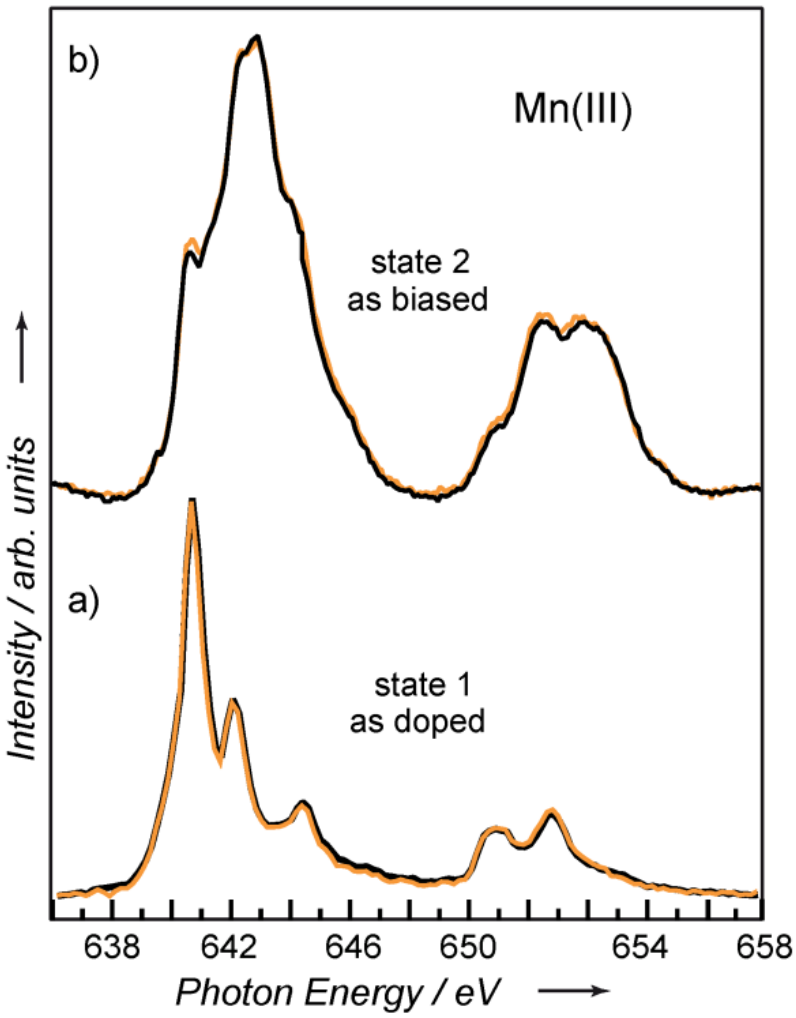

Figure A.2.1. Radiation damage study of Mn (III) in the a) as doped (state1); and b) as biased (state 2). Yellow: fresh spot, Black: subsequent measurement on the same spot. The spectra show no changes in intensity when measured on a fresh spot or two times consecutively on the same spot with fixed beam line settings. In both cases the opening of beam line apertures was 0.8×0.8, 0.8×0.8 and the beamline slit was 20μm.

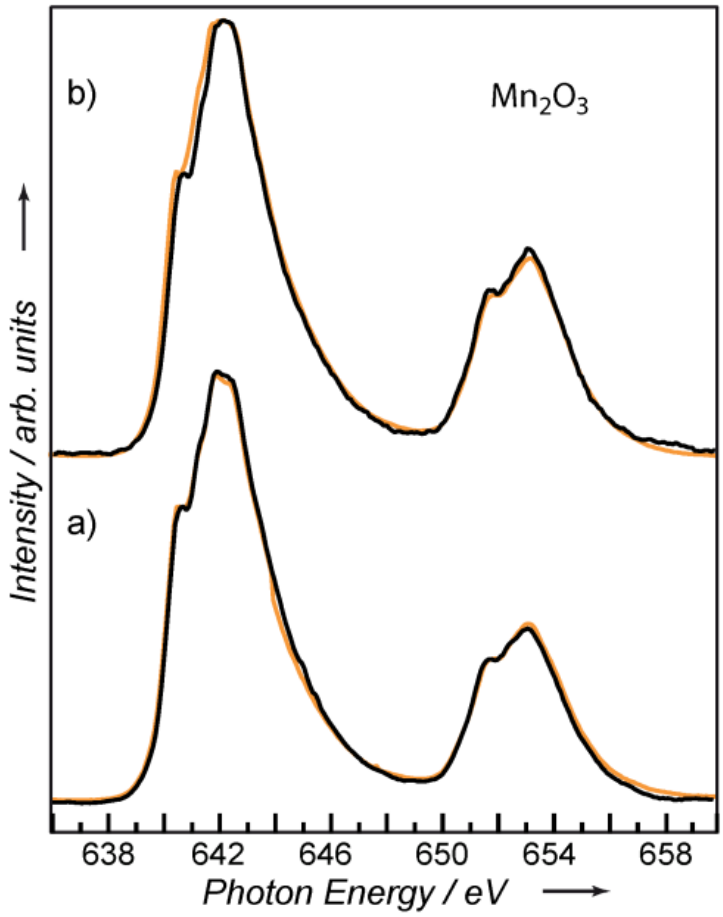

Figure A.2.2. Radiation damage study of Mn_2O_3 oxide powder; yellow: fresh sample spot, black: subsequent measurement on the same spot. The spectra were recorded with beam line slit width of 20µm. a) Apertures of 0.8×0.8, 1.0×1.0. b) Apertures of 0.2×0.2, 02×0.2. The spectra apparently look similar for the two different aperture openings (different synchrotron beam flux). This indicates the Mn_2O_3 is quite stable with no specific radiation damage when exposed to soft X-rays.

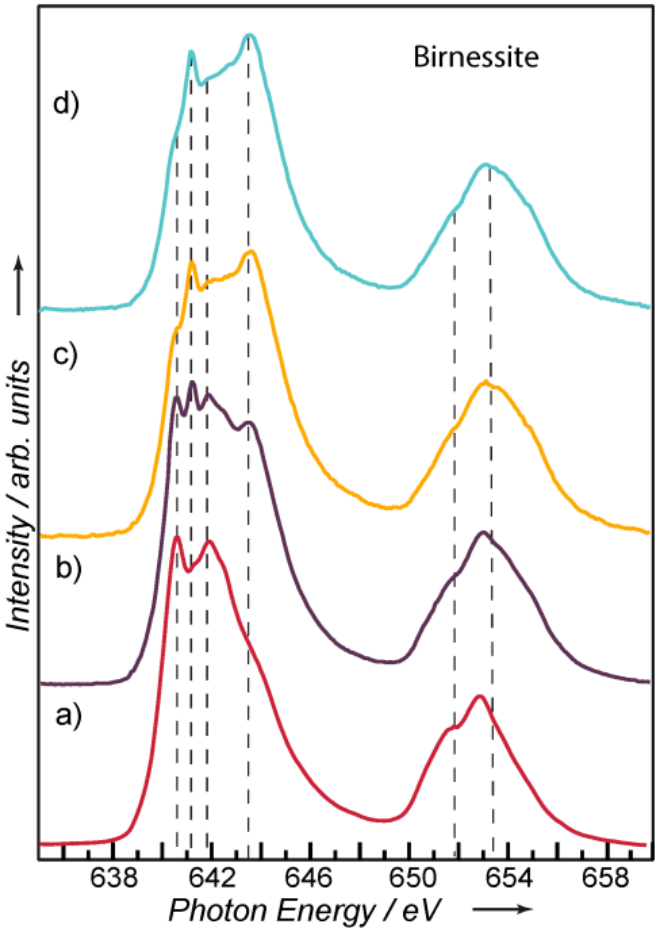

Figure A.2.3. Radiation damage study of synthetic birnessite. It showed clear changes of the spectral feature intensities, upon reduction of the photon flux. The damages were minimized by reducing the beam line apertures stepwise to the lowest possible values that allowed to record the XAS spectrum. a) Apertures of 0.8×0.8, 0.8×0.8. b) Apertures of 0.2×0.2, 02×0.2. c) Apertures of 0.1×0.1, 0.1×0.1. d) Apertures of 0.1×0.1, 0.1×0.0.

List of Figures

List of Tables

List of Abbreviations

1. PS II……..Photosystem II
2. OEC……..Oxygen Evolving Complex
3. WOC…….Water Oxidizing Center
4. CCD……...Charged Couple Device
5. XAS……...X-ray Absorption Spectroscopy
6. RIXS……...Resonant Inelastic Spectroscopy
7. HOMO……Highest Occupied Molecular Orbital
8. LUMO……Lowest Unoccupied Molecular Orbital
9. SEM……Scanning Electron Microscopy
10. TEM……Transmission Electron Microscopy
11. EDX……Energy Dispersive X-ray
12. XRD……X-ray Diffraction
13. FTIR……Fourier Transform Infrared Microscopy

Acknowledgement

I am very thankful to my supervisor Prof. Dr. Emad Flear Aziz for providing me a splendid chance to earn my doctorate in his research group at BESSY as a DAAD and HEC scholarship holder. I have always been fascinated by his devoted passion to achieve excellence in science. With this opportunity, I want to thank him for all the support and efforts he had for me. This is also a nice time to thank my second referee for thesis Prof. Dr. Ludger Wöste from the Freie University for reviewing all my research reports and helping me out whenever needed. I specially want to thank Prof. Dr. Leone Spiccia from University of Monash, Australia for helping me out to lay down the building blocks of my project in first year of my research and to complete it in due time frame. He was always there for fruitful discussions and critical comments while reviewing the manuscripts.

I would also like to thank two of my post doctorates Dr. Edlira Suljoti and Dr. Jie Xiao. You were always there to get an expert opinion on experiments, for hot scientific discussions and positive criticism. Dr. Xiao put a lot of effort for helping me to shape this thesis in its present form. Thanks a lot to Dr. Ulrich Schade for supervising the FT-IR measurements and for all his basic questions to refresh my knowledge of science. I am thankful to Dr. Sergey Bokarev and Prof. Dr. Oliver Kühn from University of Rostock to provide theoretical explanation of my experimental work. I am grateful to Dr. George Rappich who spared his chemistry lab for me to prepare samples. Special thanks go to Dr. Kaan Atak and Dr. Marc Tesch for correcting this thesis for mistakes and lively discussions. I am thankful to Dr. Ljiljana Puskar, Ronny Golnak, Kenji Yamamoto, Dr. Archana Singh, Dr. Fengling Zhou, Tim Brandenburg, and Mikhail Yablonskikh, who accompanied me during experiments at BESSY II and to all the other people who were or still are members of the group.

I am indebted to my aunt and uncle Mr. and Mrs. Asif for all their love and affection that no one was able to offer during my PhD. Since my arrival in Berlin, I have met and found many people without them, it would not have been possible to stay and complete my project in such a cheerful and comfortable environment. I want to thank all of these nice and lovely friends, who will be a part of my rest of life. I was blessed to have Mr. and Mrs. Qureshi as my neighbours. They always showed up at the time of need. I want to thank Mr. and Mrs. Farooq, Kiran Hameed, Anam Khan, Mr. and Mrs. Rahim. Many thanks go to Amna Salman, Tehmina Bibi, Fatima Saleh, Shinkay Bibi, Ruba-Al-Obaidi to spent sleepless nights with my baby while I was at long experiments during weekends. Thanks a lot from my heart to my mother, brother and lovely sister who always believed in me. At the end, I want to express my love to my sweethearts, my daughter Rameen and husband Qasim. You both mean a lot in my life and I dedicate this thesis to both of you.

References

1. N. Armaroli, V. Balzani, Energy for a Sustainable World: From the Oil Age to a Sun-Powered Futur. Wiley VCH Verlag GmbH & Co. KgaA. (2010).
2. D.G. Nocera, Acc. Chem. Res. 45 (2012) 767.
3. A.J. Bard, L.R. Faulkner, Electrochemical Methods.John Wiley & Sons, Inc. (1990).
4. G.C. Dismukes, Science. 292 (2001) 447.
5. J. Murray, J. Barber, J. Struct. Biol. 159 (2007) 228.
6. W. Hillier, T. Wydrzynski, Coord. Chem. Rev. 252 (2008) 306.
7. F. Rappaport, B.A. Diner, Coord. Chem. Rev. 252 (2008) 259.
8. D. K. Bediako, B. L. Kaiser, Y. Surendranath, J. Yano, V. K. Yachandra, D. G. Nocera, J. Am. Chem. Soc. 134 (2012) 6801.
9. J. Limburg, G. W. Brudvig, R. H. Crabtree, J. Am. Chem. Soc. 119 (1997) 2761.
10. M. M. Najafpour, Govindjeeb, Dalton Trans. 40 (2011) 9076.
11. N. Kamiya, J. Shen, Proc. Natl. Acad. Sci. USA. 100 (2003) 98.
12. M. Wiechen, M. M. Najafpour, S. I. Allakhverdiev, L. Spiccia, Energy Environ. Sci. 14 (2014) 2203.
13. G.M. Ananyev, G.C. Dismukes, Photosynth. Res. 84 (2005) 355.
14. L. Duan, F. Bozoglian, S. Mandal, B. Stewart, T. Privalov, A. Llobet, L, Sun, Nat. Chem. 4 (2012) 418.
15. K. N. Ferreira, T. M. Iverson, K. Maghlaoui, J. Barber, S. Iwata, Science. 303 (2004) 1831.
16. J. Yano, J. Kern, K. Sauer, M. J. Latimer, Y. Pushkar, J. Biesiadka, B. Loll, W. Saenger, J. Messinger, A. Zouni, V. K. Yachandra, Science. 314 (2006) 821.
17. Y. Umena, K. Kawakami, J. R. Shen, N. Kamiya, Nature. 473 (2011) 55.
18. H. Dau, I. Zaharieva, Acc Chem Res. 42 (2009) 1861.
19. M. Wiechen, L. Spiccia, ChemCatChem. 6 (2014) 439.
20. J. Yano, V. K. Yachandra, Photosynth Res. 102 (2009) 241.
21. G. C. Dismukes, R. Brimblecombe, G. A. N. Felton, R. S. Pryadun, J. E.Sheats, L. Spiccia, G. F. Swiegers, Acc. Chem. Res. 42 (2009) 1935.
22. M. Calvin, Science. 184 (1974) 375.
23. K. S. Joya, J. L. Vall, S, P, Y. F. Joya, T. Eisenmayer, B. Thomas, F. Buda, H J. M. de Groot, ChemPlusChem. 78 (2013) 35.
24. S. W. Gersten, G.J. Samuels, T. J. Meyer, J. Am. Chem. Soc. 104 (1982) 4029.
25. F. Liu, J. J. Concepcion, J. W. Jurss, T. Cardolaccia, J. L. Templeton, T. J. Meyer, Inorg. Chem. 47 (2008) 1727.

26. F. M. Toma, A. Sartorel, M. Lurlo, M. Carraro, P. Parisse, C. Maccato, S. Rapino, B. R. Gonzalez, H. Amenitisch, T. Da Ros, L. Casalis, A. Goldoni, M. Marcaccio, G. Scorrano, G. Scoles, F. Paolucci, M. Prato, M. Bonchio, Nat. Chem. 2 (2010) 826.
27. U. Hintermair, S. M. Hashmi, M. Elimelech, R.H. Crabtree, J. Am. Chem. Soc. 134 (2012) 9785.
28. J. Kiwi, M. Gratzel, Angew. Chem. Int. Ed. Engl. 18 (1979) 624.
29. G. Beni, L. M. Schiavone, J .L. Shay, W. C. Dautremont-Smith, B. S. Schneider, Nature. 282 (1979) 281.
30. J. S. Kanady, E. Y. Tsui, M. W. Day, T. Agapie, Science. 333 (2011) 733.
31. F. M. Ashmawy, C.A. McAuliffe, R.V. Parish, Dalton Trans. 7 (1985) 1391.
32. J. L. Fillol, Z. Codola, I. Garcia-Bosch, L. Gomez, J. J. Pla, M. Costas, Nat. Chem. 3 (2011) 807.
33. D. J. Wasylenko, R. D. Palmer, E. Schott, C.P. Berlinguette, Chem. Commun. 48 (2012) 2107.
34. J. N. Broughton, M. J. Brett, Electrochim. Acta. 50 (2005) 4814.
35. N. Miyamoto, S. Kitahara, Y. Matsufuj, R. Morita, Electrochemistry. 68 (2000) 95.
36. K. Q. Ding, Int. J. Electrochem. Sci. 5 (2010) 668.
37. K. Q. Ding, J. Chin, Chem. Soc. 56 (2009) 175.
38. D. Portehault , S. Cassaignon , E. Baudrin , J. P. Jolivet , J. Mater. Chem. 19 (2009) 2407.
39. G. H. Qiu , H. Wen , Q. Guo , Y. H. Hu , D. Yang , F. Liu, Ionics. 17 (2011) 209.
40. L. Zhou, J. Zhang, J. H. He, Y. C. Hu, H. Tian, Mater. Res. Bull. 46 (2011) 1714.
41. S. C. Pang, M. A. Anderson, T. W. Chapman, J. Electrochem. Soc. 147 (2000) 444.
42. A.M. Mohammad, M.I. Awad, M.S. El-Deab, T. Okajima, T. Ohsaka, Electrochim. Acta. 53 (2008) 4351.
43. R. Brimblecombe, A. M. Bond, G.C. Dismukes, G. F. Swiegers, L. Spiccia, Phys. Chem. Chem. Phys. 11 (2009) 6441.
44. R. Brimblecombe, A. Koo, G. C. Dismukes, G. F. Swiegers, L. Spiccia, J. Am. Chem. Soc. 132 (2010) 2892.
45. R. K. Hocking, R. Brimblecombe, L. Y. Chang, A. Singh, M. H. Cheah, C. Glover, W. H. Casey, L. Spiccia, Nat. chemistry. 3 (2011) 222.
46. M. Wiechen, H. M. Berends, P. Kurz, Dalton Trans. 41 (2012) 21.
47. M. Mohammad, T. Ohsaka, Electrochem. Commun. 9 (2007) 2082.
48. M. Morita, C. Iwakura, H. Tamura. Electrochim. Acta. 22 (1977) 325.
49. M. M. Najafpour, A. N. Moghaddam, S. I. Allakhverdiev, Govindjeeb, Biochim. Biophys. Acta, Bioenerg. 1817 (2012) 1110.
50. M. M. Najafpour, F. Rahimi, E.M. Aro, C.H. Lee, S. I. Allakhverdiev, J. R. Soc. Interface. 9 (2012) 2383.

51. M. M. Najafpour, T. Ehrenberg, M. Wiechen, P. Kurz, Angew. Chem. Int. Ed. 122 (2010) 2281.
52. I. Zaharieva, M. M. Najafpour, M. Wiechen, M. Haumann, P. Kurz, H. Dau, Energy Environ. Sci. 4 (2011) 2400.
53. M. M. Najafpour, Dalton Trans. 40 (2011) 3793.
54. D. Shevela, S. Koroidov, M. M. Najafpour, J. Messinger, P. Kurz, Chem. Eur. J. 17 (2011) 5415.
55. M. Wiechen, I. Zaharieva, H. Dau, P. Kurz, Chem. Sci. 3 (2012) 2330.
56. J. W. Murray, J. Barber, J. Struct. Biol. 159(2007) 228.
57. S. L. Y. Chang, A. Singh, R. K. Hocking, C. Dwyer, L. Spiccia, J.Mater. Chem. A. 2 (2014) 3730.
58. I. Djerdj, D. Arčon, Z. Jagličić, M. Niederberger, J. Phys. Chem. C. 111 (2007) 3614.
59. A. C. Gaillot, D. Flot, V. A. Drits, A. Manceau, M. Burghammer, B. Lanson, Chem. Mater. 15 (2003) 4666.
60. K. D. Kwon, K. Refson, G. Sposito, Phys. Rev. Lett.10 (2008) 146601.
61. D. M. Robinson, Y. B. Go, M. Mui, G. Gardner, Z. Zhang, D. Mastrogiovanni, E. Garfunkel, J. Li, M. Greenblatt, G. C. Dismukes, J. Am. Chem. Soc. 135 (2013) 3494.
62. A. Indra, P. W. Menezes, I. Zaharieva, E. Baktash, J. Pfrommer, M. Schwarze, H. Dau, M. Driess, Angew. Chem. Int. Ed. 52 (2013) 13206.
63. M. M. Najafpour, B. Haghighi, D. J. Sedigh, M. Z. Ghobadi, Dalton Trans. 42(2013) 16683.
64. M. M. Najafpour, D. J. Sedigh, Dalton Trans. 42 (2013) 12173.
65. F. Jiao, H. Frei, Chem. Commun. 46 (2010) 2920.
66. M. Fekete, R. K. Hocking, S. L. Y. Chang, C. Italiano, A. F. Patti, F. Arena, L. Spiccia, Energy Environ. Sci. 6 (2013) 2222.
67. W. Lubitz, E. J. Reijerse, J. Messinger, Energy Environ. Sci. 1 (2008) 15.
68. Y. Gorlin, B. Lassalle-Kaiser, J. D. Benck, S. Gul, S. M. Webb, V. K. Yachandra, J. Yano, T. F. Jaramillo, J. Am. Chem. Soc. 135 (2013) 8525.
69. J. Xiao, M. Khan, A. Singh, E. Suljoti, L. Spiccia, E. F. Aziz, ChemSusChem. 8 (2015) 872.
70. B.T. Thole, G. van der Laan, Physical Review B. 38 (1988) 3158.
71. F. M. F. de Groot, J. Electron Spectrosc. Relat. Phenom. 67 (1994) 529.
72. C. N. R. Rao, D. D. Sarma, S. Vasudevan, M. S. Hegde, Proc. R. Soc. London, A, 367 (1979) 239.
73. F. M. F. de Groot, J. C. Fuggle, B. T. Thole, G. A. Sawatzky, Phys. Rev. B, 42 (1990) 5459.

74. F. M. F. de Groot, A. Kotani, Core Level Spectroscopy of Solids. CRC Press Taylor & Francis. (2008).
75. F.M.F. de Groot, M. Grioni, H. Douglas, Physical Review B. 44 (191) 6708.
76. D. T. Attwood, Soft x-rays and extreme ultraviolet radiation: principles and applications. Cambridge University Press. (1999).
77. J. Stöhr, NEXAFS Spectroscopy, Springer-Verlag. (1996).
78. J. J. Sakurai, Advanced Quantum Mechanics. Addison Wesley.(1967)
79. K. Boon. Teo, EXAFS: Basic Principles and Data Analysis. Springer. (1986).
80. D. C. Koningsberger, X-Ray Absorption: Principles, Applications, Techniques of EXAFS, SEXAFS and XANES. John Wily & Sons. (1988).
81. S. Eisebitt, T. Böske, J. E. Rubensson, W. Eberhardt, Physical Review B. 47 (1993) 14103.
82. T. X. Carroll, J. Hahne, T. D. Thomas, L. J. Sæthre, N. Berrah, J. Bozek, and E. Kukk, Physical Review A. 61(2000) 042503.
83. F. Meyer, J. J. Vrakking, Surface Science. 33(1972) 271.
84. H. A. Kramers, W. Heisenberg, Nuclear Instruments and Methods in Physics Research Section A: Accelerators, Spectrometers, Detectors and Associated Equipment 31 (1925) 350.
85. Kwang. Je Kim. X-ray data booklet: Section 2.1-characteristics of synchrotron radiation. http://xdb.lbl.gov/Section2/Sec_2-1.html.
86. R. Garcia-Diez, Master thesis. (2013).
87. M. Gotz, Master thesis. (2012).
88. Ch. Jung, F. Eggenstein, S. Hartlaub, K. Holldack, R. Follath, M. Mast, J. S. Schmidt, F. Senf, M. R. Weiss, Th. Zeschke, U41-pgm: commissioning results.
89. A. H. Rowland, Philosophical Magazine Series. 535 (1893) 397.
90. E. Suljoti, PhD thesis. (2008).
91. M. Dantz, Master thesis. (2013).
92. R. Brimblecombe, G. C. Dismukes, G. F. Swiegers, L. Spiccia. Dalton Trans. 48 (2009) 9374.
93. R. Brimblecombe, G. F. Swiegers, G. C. Dismukes, L. Spiccia, Angew. Chem. Int. Ed. 47 (2008) 7335.
94. R. J. Pace, L. Jin, R. Stranger, Dalton Trans. 41 (2012) 11145.
95. A. Singh, R. K. Hocking, S. L. Y. Chang, B. M. George, M. Fehr, K. Lips, A. Schnegg, L. Spiccia, Chem. Mater. 25 (2013) 1098.
96. M. Khan, E. Suljoti, A. Singh, S. A. Bonke, T. Brandenburg, K. Atak, R. Golnak, L. Spiccia, E. F. Aziz, J. Mater. Chem. A. 2 (2014) 18199.
97. A. Kotani, S. Shin, Rev. Mod. Phys. 73 (2001) 203.

98. L. Z. P. Ament, M. van Veenendaal, T. P. Devereaux, J. P. Hill, J. van den Brink, Rev. Mod. Phys. 83 (2011) 705.
99. S. Grenier, J. P. Hill, V. Kiryukhin, W. Ku, Y. J. Kim, K. J. Thomas, S. W. Cheong, Y. Tokura, Y. Tomioka, D. Casa, Phys. Rev. Lett. 94 (2005) 047203.
100. P. Glatzel, J. Yano, U. Bergmann, H. Visser, J. H. Robblee, W. Gu, F. M. F. de Groot, S. P. Cramer, V. K. Yachandra, J. Phys. Chem. Solids. 66 (2005) 2163.
101. P. Glatzel, U. Bergmann, J. Yano, H. Visser, J. H. Robblee, W. Gu, F. M. F. de Groot, G. Christou, V. L. Pecoraro, S. P. Cramer, V. K. Yachandra, J. Am. Chem. Soc. 126 (2004) 9946.
102. S. P. Cramer, F. M. F. de Groot, Y. Ma, C. T. Chen, F. Sette, C. A. Kipke, D. M. Eichhorn, M. K. Chan, W. H. Armstrong, J. Am. Chem. Soc. 113 (1991) 7937.
103. M. M. Van Schooneveld, R. W. Gosselink, T. M. Eggenhuisen, M. Al Samarai, C. Monney, K. J. Zhou, T. Schmitt, F. M. F. de Groot, Angew. Chem. Int. Ed. 52 (2013) 1170; Angew. Chem. 125(2013) 1208.
104. M. M. Grush, J. Chen, T. L. Stemmler, S. J. George, C. Y. Ralston, R. T. Stibrany, A. Gelasco, G. Christou, S.M. Gorun, J. E. Penner-Hahn, S. P. Cramer, J. Am. Chem. Soc. 118 (1996) 65.
105. G. Ghiringhelli, M. Matsubara, C. Dallera, F. Fracassi, A. Tagliaferri, N. B. Brookes, A. Kotani, L. Braicovich, Phys. Rev. B. 73 (2006) 035111.
106. S. M. Butorin, J. H. Guo, M. Magnuson, P. Kuiper, J. Nordgren, Phys. Rev. B. 54 (1996) 4405.
107. S. Kučas, A. Kynienė, R. Karazija, L. D. Finkelstein, E. Z. Kurmaev, J. Phys. Condens. Matter. 17 (2005) 7307.
108. G. Ghiringhelli, A. Piazzalunga, X. Wang, A. Bendounan, H. Berger, F. Bottegoni, N. Christensen, C. Dallera, M. Grioni, J. C. Grivel, M. Moretti, L. Patthey, J. Schlappa, T. Schmitt, V. Strocov, L. Braicovich, Eur. Phys. J. Spec. Top. 169 (2009) 199.
109. I. Saratovsky, P. G. Wightman, P. A. Pastén, J. F. Gaillard, K. R. Poeppelmeier, J. Am. Chem. Soc. 128 (2006) 11188.
110. R. Parent, R. Crabtree, G. W. Brudvig, Chem. Soc. Rev. 42 (2013) 2247.
111. G. C. Dismukes, R. Brimblecombe, G. A. N. Felton, R. S. Pryadun, J. E. Sheats, L. Spiccia, G. F. Swiegers, Acc. Chem. Res. 42 (2009) 1935.
112. R. Brimblecombe, D. R. J. Kolling, A. M. Bond, G. C. Dismukes, G. F. Swiegers, L. Spiccia, Inorg. Chem. 48 (2009) 7269.
113. B. Gilbert, B. H. Frazer, A. Belz, P. G. Conrad, K. H. Nealson, D. Haskel, J. C. Lang, G. Srajer, G. De Stasio, J. Phys. Chem. A. 107 (2003) 2839.

114. J. Park, H. Kim, K. Jin, B. J. Lee, Y. S. Park, H. Kim, I. Park, K. D. Yang, H. Y. Jeong, J. Kim, K. T. Hong, H. W. Jang, K. Kang, K. T. Nam, J. Am. Chem. Soc. 136 (2014) 4201.
115. T. Takashima, K. Hashimoto, R. Nakamura, J. Am. Chem. Soc. 134 (2012) 1519.
116. T. Takashima, K. Hashimoto, R. Nakamura, J. Am. Chem. Soc. 134 (2012) 18153.
117. I. Zaharieva, P. Chernev, M. Risch, K. Klingan, M. Kohlhoff, A. Fischer, H. Dau, Energy Environ. Sci. 5 (2012) 7081.
118. Y. Gorlin, T. F. Jaramillo, J. Am. Chem. Soc. 132 (2010) 13612.
119. M. Magnuson, L. C. Duda, S. M. Butorin, P. Kuiper, J. Nordgren, Phys. Rev. B: Condens. Matter Mater. Phys. 74 (2006) 172409.
120. P. Malmqvist, Å. Roos, O. Schimmelpfennig, Chem. Phys. Lett. 357 (2002) 230.
121. I. Josefsson, K. Kunnus, S. Schreck, A. Föhlisch, F. M. F. de Groot, P. Wernet, M. Odelius, J. Phys. Chem. Lett. 3 (2012) 356.
122. P. Wernet, K. Kunnus, S. Schreck, W. Quevedo, K. Kunnus, R. S. Techert, F.M. F. de Groot, M. Odelius, A. Föhlisch, J. Phys. Chem. Lett. 3(2012) 3448.
123. E. Suljoti, R. Garcia-Diez, S. I. Bokarev, K.M. Lange, R. Schoch, B. Dierker, M. Dantz, K. Yamamoto, N. Engel, K. Atak, O. Kühn, M. Bauer, M, J. E. Rubensson, E. F. Aziz, Angew. Chem. Int. Ed. 52 (2013) 9841.
124. S. I. Bokarev, M. Dantz, E. Suljoti, O. Kühn, E. F. Aziz, Phys. Rev. Lett. 111 (2013) 083002.
125. K. Atak, S. I. Bokarev, M. Gotz, R. Golnak, K. M. Lange, N. Engel, M. Dantz, E. Suljoti, O. Kühn, E. F. Aziz, J. Phys. Chem. B. 117 (2013) 12613.
126. N. Engel, S. I. Bokarev, E. Suljoti, R. Garcia-Diez, K. M. Lange, K. Atak, R. Golnak, A. Kothe, M. Dantz, O. Kühn, E. F. Aziz, J. Phys. Chem. B. 118 (2014) 1555.
127. R. Pinjari, V. Delcey, M. G. Guo, M. Odelius, M. Lundberg, J. Chem. Phys. 141 (2014) 124116.
128. F. Zhou, A. Izgorodin, R. K. Hocking, V. Armel, L. Spiccia, D. R. MacFarlane, ChemSusChem. 6 (2013) 643.
129. F. Zhou, A. Izgorodin, R. K. Hocking, L. Spiccia, D. R. MacFarlane, Adv. Energy Mater. 2 (2012) 1013.
130. M. Najafpour, M. A. Isaloo, RSC Adv. 4 (2014) 6375.
131. A. Yamaguchi, R. Inuzuka, T. Takashima, T. Hayashi, K. Hashimoto, R. Nakamura, Nat. Commun. 5 (2014) 5256.
132. A. Ramírez, P. Hillebrand, D. Stellmach, M. M. May, P. Bogdanoff, S. Fiechter, J. Phys. Chem. C. 118 (2014) 14073.
133. A.J. Esswein, Y. Surendranath, S. Y. Reece, D. G. Nocera, Energy Environ. Sci. 4 (2011) 499.

134. Y. Gorlin, C. J. Chung, D. Nordlund, B. M. Clemens, T. F. Jaramillo, ACS Catal. 2 (2012) 2687.
135. S. M. A. Shibli, P. S. Arun, A. V. Raj, RSC Adv. 5 (2015) 19393.
136. K. M. Lange, K. F. Hodeck, U. Schade, E. F. Aziz, J. Phys. Chem. B 114 (2010) 16997.
137. K. M. Lange, R. Könnecke, M. Soldatov, R. Golnak, J. E. Rubensson, A. Soldatov, E. F. Aziz, Angew. Chem. Int. Ed. 50 (2011) 10621; Angew. Chem. 123 (2011) 10809.
138. L. J. Garvie, A. J. Craven, Phys. Chem. Miner. 21 (1994) 191
139. S. Thürmer, R. Seidel, W. Eberhardt, S. E. Bradforth, B. Winter, J. Am. Chem. Soc. 133 (2011) 12528.
140. T. Petit, K. M. Lange, G. Conrad, K. Yamamoto, C. Schwanke, K. F. Hodeck, M. Dantz, T. Brandenburg, E. Suljoti, E. F. Aziz, Struct. Dyn.1 (2014) 034901.